DOCTOR OF PHILOSOPHY

Precipitation Behaviour of Wrought and Additively Manufactured Ti-5553 β-Ti Alloy

Sharma, Deepak

Award date:
2022

Awarding institution:
Coventry University
Deakin University

Precipitation Behaviour of Wrought and Additively Manufactured Ti-5553 β-Ti Alloy

By

Deepak Sharma

PhD

February 2021

Precipitation Behaviour of Wrought and Additively Manufactured Ti-5553 β-Ti Alloy

By

Deepak Sharma

PhD

A thesis submitted in partial fulfilment of the University's requirements for the Degree of Doctor of Philosophy. This thesis is a jointly supervised Cotutelle Programme with Coventry University and Deakin University.

February 2021

Certificate of Ethical Approval

Applicant:

Deepak Sharma

Project Title:

Effects of Alloying Elements on Microstructures and Mechanical Properties of ß-Ti alloys

This is to certify that the above named applicant has completed the Coventry University Ethical Approval process and their project has been confirmed and approved as Low Risk

Date of approval:

23 June 2020

Project Reference Number:

P97026

[redacted]

ABSTRACT

This dissertation provides important insights into the phase transformations occurring in the wrought (conventionally produced) and the additively manufactured (AM) β-Ti alloy as a function of different heat treatment parameters. High-end characterisation techniques such as small-angle neutron scattering (SANS) and electrical resistivity measurement were performed to study the *in situ* nucleation and growth kinetics of phase transformations as a function of heat treatment parameters. Scanning electron microscopy, energy dispersive spectroscopy, electron backscatter diffraction, and X-ray diffraction were used to understand the variability in the microstructural features. These techniques were also used to complement the nucleation and growth kinetics study. A Vickers' microhardness tester was used to measure the microhardness of the samples to establish the relationship between microstructure and the associated mechanical properties. The availability of microstructure-property relationship data at different heat treatment conditions will benefit β-Ti users. The critical evaluation and understanding of additively manufactured β-Ti alloy will support the potential application of additive manufacturing in the aerospace sector. Further, a better understanding of the precipitation kinetics in the material will enable precise control and optimisation of the alloy properties. Ti–5Al–5V–5Mo–3Cr wt% (Ti-5553), a metastable β-Ti alloy system, was selected for this work due to its desirable properties for high strength applications and increasing use in the aerospace industry.

The influence of different ageing approaches (single ageing with different heating rates, and duplex ageing) on the microstructure evolution and the associated property of the wrought alloy was studied extensively. The observations indicated that single aged

samples with slow heating rate and duplex aged samples produced approximately similar microstructures and microhardness at all ageing conditions. This was attributed to the same precipitation mechanism in both cases as observed via *in situ* electrical resistivity measurements. Both these samples showed extremely fine and uniform microstructures in comparison to single aged samples with a fast heating rate. The single aged samples with slow heating rate and duplex aged samples generally produced higher microhardness in comparison to single aged samples with fast heating rate. However, the difference in the microhardness tended to decrease with ageing time at higher temperatures (600 °C and 700 °C). A correlation ($H_v = 348 + 247/\sqrt{d}$) between the microhardness values and the width of α-phase (d) was established for all the aged wrought samples. This study also supported that the precursor isothermal ω-phase (ω_{iso}) precipitates have a direct influence on the nucleation of the α-phase leading to better alloy properties.

Since the nanoscale ω_{iso} precipitates assisted α-phase nucleation led to the higher microhardness, therefore, an investigation was done to study the precipitation kinetics of the ω_{iso} precipitates during low-temperature ageing (300 °C and 325 °C) up to 8 h to better control the mechanical properties. The precipitation kinetics were studied as a function of cooling rate (air cooling and water quenching) after β-solutionising because, for structural applications in the aerospace industry, the section thickness may determine the achievable cooling rate and therefore limit the mechanical properties. A combined *in situ* SANS and electrical resistivity measurement approach was used for this purpose. The SANS modelling was consistent with ellipsoid shaped particles for the ω_{iso} precipitates, for both air-cooled and water-quenched samples. The precipitates attained a maximum size (equatorial diameter) of ~21 nm and ~17 nm after 2 h and 4 h of ageing the water-quenched and the air-cooled samples, respectively. Although the air-cooled samples showed delayed nucleation in comparison to the water-quenched samples, the volume fraction became approximately the same (~11 %) after ageing for 8 h. The average value of the activation energy for ω_{iso} nucleation from the β-phase matrix was determined as ~122 kJ mol^{-1} from electrical resistivity data using a modified Johnson-Mehl-Avrami-Kolmogorov (JMAK) model. The aged sample after water quenching showed higher hardness than the aged samples after air cooling, with the hardness values trend with ageing time for both the cooling rates.

Additive manufacturing of titanium alloys for aerospace applications is attractive due to design and near net shape benefits. However, the formation of solely β-phase after direct laser deposition of β-Ti alloy does not provide the desired properties. Hence, the ageing response (after single ageing with different heating rates, and duplex ageing) of the AM Ti-5553 β-Ti alloy was studied to obtain the bimodal (β+α) microstructure providing improved properties. The as-built samples showed the presence of elemental segregation due to the formation of sub-structures within the β-phase matrix. The duplex aged samples and single aged samples with slow heating rate showed higher hardness when compared to single aged samples with fast heating rate, similar to the wrought alloy. This is attributed to the extreme refinement of microstructure due to ω_{iso} precipitates assisted α-phase nucleation. The single aged samples with a fast heating rate showed refined intragranular and discontinuous grain boundary α-phase when aged at 500 °C and 600 °C. This is important to get higher strength and higher ductility at the same time. The as-built and aged samples showed similar final microstructures with respect to the wrought samples. This boosts confidence in exploring the possibility of the use of the direct laser deposition method in applications. Similar to wrought alloy, a correlation ($H_v = 348 + 168/\sqrt{d}$) between the microhardness values and the width of α-phase (d) was established for all the aged AM samples. The solution-treated AM sample showed coarser intragranular α-phase precipitates (width = 139 ± 22 nm) with continuous grain boundary α-phase precipitates (thickness = 126 ± 12 nm) after ageing (600 °C/0.5 h). However, the AM sample directly aged (600 °C/0.5 h) after deposition exhibited refined intragranular α-phase precipitates with an average width of 105 ± 20 nm and discontinuous grain boundary α-phase precipitates with an average thickness of 46 ± 11 nm. Refined intragranular α-phase precipitates in the AM sample led to increased hardness from 400 ± 5 Hv to 424 ± 4 Hv (~6% increase) in comparison to the solution-treated sample. The average activation energy for ω_{iso} precipitation from the β-phase matrix of as-built and solution-treated samples was calculated as ~130 kJ/mol using the modified JMAK model for electrical resistivity data.

ACKNOWLEDGEMENTS

First and foremost, I owe my sincere gratitude to my mentors and guides from my supervisory team in two different parts of the world – the UK and Australia, where my work was led by Prof. Michael E. Fitzpatrick and Dr. Sitarama Raju Kada as my Director of Studies at Coventry University (UK) and Principal Supervisor at Deakin University (Australia), respectively. The other members of the supervisory team include Prof. Bo Chen and A/Prof. David Parfitt at Coventry University, and Prof. Matthew Robert Barnett and A/Prof. Daniel Fabijanic at Deakin University. Without their untiring mentorship, constant inspiration, valuable discussions and suggestions, this work would not have been possible. They patiently provided the vision, encouragement, and advice necessary for me to proceed through the entire research program. Their constructive guidance and encouragement helped me to think positively and intelligently.

I take the opportunity to especially thank Dr. Bryan Roebuck from National Physical Laboratory, London and Dr. Diego Alba Venero from ISIS Neutron and Muon Source, Rutherford Appleton Laboratory, Oxfordshire for helping me with the electrical resistivity and small-angle neutron scattering experiments, respectively. I would also want to extend my special thanks to Dr. Yiqiang Wang from the Culham Centre for Fusion Energy, Oxfordshire for his willingness to give his time to discuss the results from small-angle neutron scattering experiments. I am also thankful to the technical staff at Coventry University: Steven Allitt, Colin Thorneycroft, Geoff Booth, Rizwan Tai, and Steve Damms; who helped me with the machines required for my experimental work. I wish to thank my friends and research colleagues at Coventry and Deakin

University especially Dr. Abul Syed Khadar, Dr. Niall Smyth, Dr. Yao Li, Dr. Yiding Liu, Dr. Arpit Goyal, Dr. Sattam Saha, Sithila Theminimulla, Sunil Anandatheertha, Muhammad Shamir, Gokulnath Kadavath, and Hitesh Sharma for their constant support.

I am grateful to Coventry and Deakin University for starting a very interesting cotutelle program. This provided me with unparalleled international exposure, and I got to work with world-class researchers from both Universities. This program also provided me with an opportunity to utilise the best laboratories across two continents. I am thankful to Coventry University for providing the necessary funding for my research.

I am also grateful to National Physical Laboratory, London and ISIS Neutron and Muon Source, Rutherford Appleton Laboratory, Oxfordshire for giving me access to electrical resistivity measurement kit and LARMOR neutron beamline (via RB1820495) to perform electrical resistivity and small-angle neutron scattering experiments, respectively.

Finally, I am nothing without my family, I express my heartiest gratitude to my parents (Mr. Somvir Sharma and Mrs. Sudha Devi), my brothers (Dinesh Sharma and Anuj Sharma) and my wife (Ruby Sharma) for their love and blessings. Their untiring support and co-operation in every step of my life made it possible for me to reach this stage. This thesis is dedicated to my family. Above all, I want to thank the supreme power of nature who provided me with the strength and the patience to achieve the goal.

Deepak Sharma
February 2021

PUBLICATIONS

Some part of this work has been published and some part is still under review or preparation for publication. Following are the details of publications:

1. **D. Sharma**, D. Parfitt, B. Chen, B. Roebuck, DA Venero, SR Kada, D Fabijanic, ME Fitzpatrick, “Influence of cooling rate on the precipitation kinetics of nanoscale isothermal ω-phase in metastable β-Ti alloy, Ti–5Al–5Mo–5V–3Cr”, J. Alloy Compd., 859, 2021, 157822.
2. **D. Sharma**, D. Parfitt, B. Roebuck, SR Kada, D Fabijanic, ME Fitzpatrick, “Precipitation behaviour of single and duplex aged metastable β-Ti alloy, Ti–5Al–5Mo–5V–3Cr”, under review in Mat. Sci. Tech., 2021.
3. **D. Sharma**, SR Kada, D Fabijanic, D. Parfitt, B. Chen, B. Roebuck, ME Fitzpatrick, MR Barnett, “The ageing response of direct laser deposited metastable β-Ti alloy, Ti–5Al–5Mo–5V–3Cr” under review in Addit. Manuf., 2021

TABLE OF CONTENTS

LIST OF FIGURES……………...…………………………………….................XIII

LIST OF TABLES…...……..……………………….…….…………...............XXII

CHAPTERS

1. INTRODUCTION 1

1.1 Motivation 1

1.2 Contributions of the Dissertation 2

1.3 Structure of the Thesis.. 3

2. LITERATURE REVIEW 5

2.1 Titanium Alloys.. 5

2.1.1 α Titanium Alloys.. 5

2.1.2 Near α Titanium Alloys 6

2.1.3 α + β Titanium Alloys.. 6

2.1.4 β Titanium Alloys 6

2.2 Phases in β Titanium Alloys.. 7

2.3 Phase Transformations in β Titanium Alloys.. 12

2.3.1 β to α-phase Transformation.. 12

2.3.2 β to ω-phase Transformation 15

2.3.3 ω-phase-Assisted α-phase Nucleation 17

2.4 Ti-5553 β Titanium Alloy and its Importance 23

2.5 Additive Manufacturing 27

2.6 Research Gaps 31

2.7 Research Questions 32

3. EXPERIMENTAL METHODOLOGY 33

3.1 Material and its Processing 33

3.1.1 Conventionally Made or Wrought Alloy 33

3.1.2 Additively Manufactured Alloy 35

3.2 Heat Treatment Procedures 37

3.2.1 Solution Treatment 37

3.2.2 Ageing Treatment 39

3.3 Characterisation Tools 40

3.3.1 Metallography 40

3.3.2 Scanning Electron Microscopy (SEM) 40

3.3.3 Energy Dispersive Spectroscopy (EDS) 41

3.3.4 Electron Backscatter Diffraction (EBSD) 41

3.3.5 X-ray Diffraction (XRD) 41

3.3.6 Vickers Microhardness 42

3.3.7 Quantification of Microstructure 42

3.3.8 Small-angle Neutron Scattering (SANS) 43

3.3.9 Electrical Resistivity Measurement 45

4. PRECIPITATION BEHAVIOUR OF SINGLE AND DUPLEX AGED WROUGHT METASTABLE β-Ti ALLOY 48

4.1 Introduction 48

4.2 Experimental Details 49

4.3 Results 51

4.3.1 Microstructural Characterisation 51

4.3.2 XRD Analysis 58

4.3.3 Microhardness 59

4.3.4 Electrical Resistivity Measurement 61

4.4 Discussion 62

4.4.1 Precipitation Kinetics 62

4.4.2 Evolution of Intragranular α-phase Precipitates 64

4.4.3 Effect of Intragranular α-phase Precipitates on Microhardness 65

4.4.4 Correlation between Microstructure and Microhardness 67

4.5 Conclusions 67

5. PRECIPITATION KINETICS OF NANOSCALE ISOTHERMAL ω-PHASE IN β-Ti ALLOY AS A FUNCTION OF DIFFERENT COOLING RATES 69

5.1 Introduction 69

5.2 Experimental Details 70

5.3 Results 71

5.3.1 Microstructural Characterisation 71

5.3.2 Small-angle Neutron Scattering 73

5.3.3 Electrical Resistivity Measurement 74

5.3.4 Microhardness 77

5.4 Discussion 78

5.4.1 Interpretation of SANS Measurements 78

5.4.2 Model-independent Analysis 81

5.4.3 Model Fitting of SANS Data 86

5.4.4 Analysis of Initial Trends upon Heating 90

5.4.5 Precipitation Kinetics 91

5.4.6 Precipitation Mechanism 93

5.5 Conclusions 96

6. THE AGEING RESPONSE OF ADDITIVELY MANUFACTURED β-Ti ALLOY 98

6.1 Introduction 98

6.2 Experimental Details 98

6.3 Results 100

6.3.1 Microstructural Characterisation 100

6.3.2 Aged Microstructure 104

6.3.3 Microhardness 109

6.3.4 XRD Analysis 111

6.3.5 Electrical Resistivity Measurement 112

6.4 Discussion 114

6.4.1 Formation of Microstructure for As-built Samples 114

6.4.2 Evolution of Intragranular α-phase Precipitates 115

6.4.3 Effect of Intragranular α-phase on Microhardness 117

6.4.4 Evolution of Grain Boundary α-phase 118

6.4.5 Precipitation Kinetics 121

6.4.6 Precipitation Mechanism 122

6.4.7 Correlation between Microstructure and Microhardness 124

6.5 Conclusions 125

7. SUMMARY AND FUTURE WORK 127

8. References 132

LIST OF FIGURES

Fig. 2.1. Classification of Ti alloys based on their position on the β isomorphous phase diagram {redrawn from [13]}... 7

Fig. 2.2. (a) Crystal structure of bcc β-phase, and (b) crystal structure of hcp α-phase {redrawn from [13]}.. 9

Fig. 2.3. Effect of alloying elements on phase diagrams of Ti alloys {redrawn from [13]}.. 11

Fig. 2.4. Schematic phase diagram for β isomorphous Ti alloys showing metastable ω-phase and phase separation as β+β' {redrawn from [13]}. 11

Fig. 2.5. Microstructure of Ti alloys showing the (a) Allotriomorphic & Widmanstätten α-phase [42], and (b) intergranular & intragranular α-phase [43]................................ 13

Fig. 2.6. Microstructure of Ti alloys showing the morphology of α-phase as (a) acicular [54], (b) chevron-shaped [48], and (c) lamellar [43]... 14

Fig. 2.7. High-resolution images showing the nucleation of α-phase platelets in the core of a ω-phase via displacive mechanism [108].. 18

Fig. 2.8. Dark-field TEM image recorded with <113> β zone axis, showing α-phase at the β/ω interface [12].. 19

Fig. 2.9. Schematic diagram of the ω-assisted α-phase formation [109]. 19

Fig. 2.10. SEM micrograph of a duplex-aged sample aged at 600 °C for 1 h [8].......... 22

Fig. 2.11. Beta annealed, slow cooled and aged heat treatment cycle........................... 25

Fig. 2.12. Solution treated and single aged heat treatment cycle. 25

Fig. 2.13. The breakdown for the processing cost of wrought Ti alloys [126]. 28

Fig. 2.14. Cellular/cellular-dendritic solidification of the melt [11]. 30

Fig. 3.1. Photograph of the Ti-5553 β-Ti alloy disc obtained from TIMET. 1, 2, and 3 are the marked locations from where the samples were extracted to check the variations in the microstructure and the microhardness values in the disc. 34

Fig. 3.2. The SEM micrographs and the microhardness values taken from different locations (1,2, and 3) marked on the disc in Fig. 3.1... 35

Fig. 3.3. (a) Typical appearance of Ti-5553 β-Ti alloy powder used for producing the additively manufactured samples. (b) shows the particle size distribution for the gas atomised Ti-5553 β-Ti powder used in this work. 36

Fig. 3.4. The deposition track profile for depositing the double-wall (DW) samples.... 37

Fig. 3.5. The typical appearance of the double-wall sample after deposition. 37

Fig. 3.6. The cooling rate measurement curves for water quenching (WQ) and air cooling (AC) after solution treatment. The figure also shows the enlarged data around 2000s to highlight the difference between the cooling rates. 39

Fig. 3.7. SEM micrographs of the aged samples along with their corresponding drawings. 43

Fig. 3.8. Photograph of the LARMOR instrument set-up for in situ SANS experiment. 45

Fig. 3.9. The schematics of in situ SANS experiment to study the kinetics of isothermal ω-phase as a function of different cooling rate after solution treatment. 45

Fig. 3.10. Typical set-up of the electrical resistivity measurement system. 47

Fig. 3.11. The schematics of the electrical resistivity measurement set-up illustrating the working of the system. 47

Fig. 4.1. Schematics of the heat treatment cycles used in this work to understand the influence of different ageing approaches on the microstructure evolution and associated

mechanical properties of Ti-5553 β-Ti alloy. SA1 represents single ageing with fast heating rate, SA2 represents single ageing with slow heating rate, and DA represents duplex ageing approach. WQ indicates water quenching.. 50

Fig. 4.2. Schematics of the heat treatment cycles used to identify the precipitation mechanisms occurring during different ageing approaches by determining the dependence of electrical resistivity on the ageing temperature and ageing time. WQ indicates water quenching. 50

Fig. 4.3. The backscattered electron micrographs of the (a) as-received, (b) solution-treated and (c) the pre-aged (300 °C + 8 h) conditions of wrought Ti-5553 β-Ti alloy. 51

Fig. 4.4. BSE-SEM micrographs showing the grain boundary and intragranular α-phase precipitates for aged Ti-5553 β-Ti alloy at 500 °C for varied ageing time after following (a), (b) single ageing with fast heating rate (SA1), (c), (d) single ageing with slow heating rate (SA2), and (e) (f) duplex ageing (DA) approach....................................... 53

Fig. 4.5. BSE-SEM micrographs showing the grain boundary and intragranular α-phase precipitates for aged Ti-5553 β-Ti alloy at 600 °C for varied ageing time after following (a), (b) single ageing with fast heating rate (SA1), (c), (d) single ageing with slow heating rate (SA2), and (e) (f) duplex ageing (DA) approach....................................... 54

Fig. 4.6. BSE-SEM micrographs showing the grain boundary and intragranular α-phase precipitates for aged Ti-5553 β-Ti alloy at 700 °C for varied ageing time after following (a), (b) single ageing with fast heating rate (SA1), (c), (d) single ageing with slow heating rate (SA2), and (e) (f) duplex ageing (DA) approach....................................... 55

Fig. 4.7. The variation in the (a) volume fraction, (b) width and (c) interparticle spacing of intragranular α-phase precipitates for Ti-5553 β-Ti alloy aged via different ageing approaches at different temperatures and for different ageing time.............................. 57

Fig. 4.8. The evolution of XRD diffraction pattern after solution treatment (ST), pre-ageing and ageing at different temperatures for 0.5 h after single ageing with fast heating rate (SA1)... 59

Fig. 4.9. The microhardness characteristics of Ti-5553 β-Ti alloy heat treated via different ageing approaches at different temperatures and for different ageing time. SA1 represents single ageing with fast heating rate, SA2 represents single ageing with slow heating rate, and DA represents duplex ageing approach. WQ indicates water quenching. 61

Fig. 4.10. The relative electrical resistivity plots obtained from the solution-treated Ti-5553 β-Ti alloy during the heating period up to 700 °C for (a) single ageing with fast heating rate (SA1) and (b) single ageing with slow heating rate (SA2). (c) shows the relative electrical resistivity plot for pre-ageing-step (300 °C + 8 h) in duplex ageing (DA) measured during heating period up to 300 °C and during ageing at 300 °C up to 8h. 62

Fig. 4.11. Variation of mean hardness with inverse of square root of mean width of α-phase after ageing the AM Ti-5553 β-Ti alloy samples. 67

Fig. 5.1. The schematics of heat treatment cycle used in this work to understand the nucleation and growth kinetics of nanoscale isothermal ω-phase precipitates in Ti-5553 β-Ti alloy as a function of water quenching (WQ) and air cooling (AC) during solution treatment. 71

Fig. 5.2. The BSE-SEM microstructure of Ti-5553 β-Ti alloy samples after solution treatment (ST) under (a) water quenching (WQ) and (b) air cooling (AC), (c) and (d) show the BSE-SEM microstructure of aged samples (300 °C for 8 h) after WQ and AC, respectively. 72

Fig. 5.3. The XRD diffraction patterns of Ti-5553 β-Ti alloy samples after (a) solution treatment (ST) using water quenching (WQ) and air cooling (AC). The XRD patterns show the presence of solely β-phase. The doublets seen in the XRD data are due to the diffraction from both $K_{\alpha 1}$ and $K_{\alpha 2}$ emissions. (b) shows the XRD diffraction patterns after subsequent ageing the solution-treated samples at 300 °C for 8 h, indicating the presence of β-phase and small volume fraction of isothermal ω-phase and α″-phase. .. 73

Fig. 5.4. The one-dimensional intensity (I) vs momentum transfer (q) plots of SANS scattering for Ti-5553 β-Ti alloy samples measured at room temperature (RT), after heating period (100 s) and in situ at 300 °C up to 8 h after (a) water quenching (WQ) and (b) air cooling (AC). The mentioned time represent the end of the measurement. BKG refers to the background scattering. 74

Fig. 5.5. The evolution of electrical resistivity measurements for Ti-5553 β-Ti alloy recorded in-situ at room temperature, heating period to reach (a) 300 °C and (b) 325 °C, and during ageing at (c) 300 °C and (d) 325 °C up to 8 h for samples that were previously water-quenched (WQ) or air-cooled (AC) from the solution-treated condition. 77

Fig. 5.6. The characteristic evolution of Vickers microhardness for Ti-5553 β-Ti alloy as a function of ageing time up to 8 h at 300 °C. The plot also shows the comparison of microhardness values obtained for the current work with the available values in the literature for same alloy after water quenching at same ageing conditions................... 78

Fig. 5.7. One-dimensional plots of scattering intensity (I) vs scattering vector (q) for SANS measurements for Ti-5553 β-Ti alloy at room temperature (RT) and after the heating period (100 s of ageing data at 300 °C) after (a) water quenching (WQ) and (b) air cooling (AC) after solution treatment. 80

Fig. 5.8. One-dimensional plots for the whole measurement process for Ti-5553 β-Ti alloy samples after (a) water quenching (WQ) and (b) air cooling (AC) showing deviation in scattering from the Guinier-Porod regime during ageing, whilst (c) and (d) show the SANS signals produced during ageing at 300 °C up to 8 h after WQ and AC, respectively. 81

Fig. 5.9. The Kratky plots for the (a) water-quenched (WQ) and (b) air-cooled (AC) samples for the entire measurement process at 300 °C, and (c) shows the Q invariant fitting of the data to calculate the volume fraction. 83

Fig. 5.10. The evolution of ω-phase precipitate during the ageing time at 300 °C up to 8 h after water quenching and air cooling. (a) shows the characteristic polar size of the precipitates, whilst (b) shows the evolution in the equatorial dimension of the precipitate. 89

Fig. 5.11. The evolution of volume fraction of isothermal ω-phase precipitates obtained from the ellipsoid model fitting. It could be seen from the plot that the volume fraction increased as a function of ageing time. 90

Fig. 5.12. Kinetic curves showing the isothermal ω-phase transformed fraction vs. ageing time: at (a) 300 °C and (b) 325 °C. The air-cooled (AC) sample showed a delayed nucleation of isothermal ω-phase precipitates when compared to water-quenched (WQ) sample. 93

Fig. 5.13. The modified JMAK plots for Avrami exponents (m) during isothermal ω-phase transformation as a function of WQ and AC at (a) 300 and (b) 325 °C. 95

Fig. 6.1. The schematics of the heat treatment cycle used to understand the ageing response of additively manufactured (AM) Ti-5553 β-Ti alloy. The heat treatment was carried out using different parameters: (a) fast heating rate plus single ageing (SA1), (b)

slow heating rate plus single ageing (SA2), (c) duplex ageing (DA), and (d) solution treatment plus single ageing (ST). 99

Fig. 6.2. The schematics of the heat treatment cycle used to perform the electrical resistivity measurements on the as-built and the solution-treated samples to understand the kinetics of isothermal ω-phase during low-temperature (300 °C and 325 °C) ageing. 100

Fig. 6.3. SEM micrograph of as-built sample showing the presence of porosities at the (a) Top, (b) Middle, and (c) Bottom of the sample. 101

Fig. 6.4. (a) The EBSD map of the cross-section of the as-built sample showing the characteristics of β-phase along the build direction. (b) shows the SEM micrograph of the as-built sample showing the presence of solely β-phase and the cellular sub-structures after deposition. (c) shows the pole figures for the as-built sample showing the texture along the <100> direction with texture intensity as 4 times random. 102

Fig. 6.5. The energy dispersive spectroscopy maps and point analysis done on the sub-structures (point 1) and sub-structures boundaries (point 2) to find out their elemental composition. 103

Fig. 6.6. The BSE SEM microstructure of the solution-treated (ST) sample showing the presence of solely β-phase without any sub-structures. 104

Fig. 6.7. The BSE-SEM microstructure of aged (600 °C/0.5 h) Ti-5553 β-Ti alloy (a) directly after deposition (AB) and (b) after solution treatment (ST), illustrating the grain boundary and intragranular α-phase characteristics. 105

Fig. 6.8. BSE-SEM microstructure of aged (600 °C/0.5 h) Ti-5553 β-Ti alloy showing (a) the presence of sub-structures after ageing. (b) shows low magnification SEM micrograph showing uniform distribution of intragranular α-phase across the sub-

structures and sub-structure free regions. AB refers to the as-built sample. (c) and (d) shows the high magnification SEM micrographs from sub-structures and sub-structure free regions, respectively. No observable difference in the α-phase characteristics were observed across the different regions. 106

Fig. 6.9. The BSE SEM microstructure of the as-built Ti-5553 β-Ti alloy samples aged (a) using the fast heating rate at 500 °C and (b) 700 °C for 0.5 h. (c) and (d) shows the aged microstructure after slow heating and duplex ageing at 600 °C for 0.5 h, respectively. SA1 refers to the single ageing with fast heating rate, SA2 refers to the single ageing with slow heating rate, and DA refers to the duplex ageing. 107

Fig. 6.10. The characteristic variation in (a) volume fraction, (b) width of intragranular α-phase, and (c) interparticle spacing between the α-phase as a function of different ageing approaches... 108

Fig. 6.11. The characteristics of grain boundary α-phase precipitate for as-built (AB) samples as a function of ageing temperature, and for solution-treated (ST) sample after ageing. 109

Fig. 6.12. The hardness characteristics AM Ti-5553 β-Ti alloy as a function of different ageing approaches. The hardness values of as-built (AB) and solution-treated (ST) samples are also shown in the Fig. SA1 refers to the single ageing with fast heating rate, SA2 refers to the single ageing with slow heating rate, and DA refers to the duplex ageing. 111

Fig. 6.13. The evolution of XRD diffraction pattern for as-built, pre-aged (300 °C + 8 h) and single-aged after single ageing with fast heating rate. AB refers to the as-built sample... 112

Fig. 6.14. The electrical resistivity measurements for as-built (AB) and solution-treated (ST) samples during ageing at (a) 300 °C and (b) 325 °C for 15 h. 113

Fig. 6.15. The grain boundary misorientation mapping for (a) as-built and (b) solution-treated (ST) AM Ti-5553 β-Ti alloy. 116

Fig. 6.16. The nucleation and growth mechanism for grain boundary α-phase. Heterogenous nucleation happens at grain boundaries and diffusion of Al and O leads the growth of the grain boundary α-phase and precipitate free zones near grain boundaries. 119

Fig. 6.17. Kinetic curves showing the ω_{iso} transformed fraction vs. ageing time: at (a) 300 °C and (b) 325 °C. A delay in the nucleation of ω_{iso} precipitates was observed for as-built samples when compared to the solution-treated samples. AB refers to the as-built sample and ST refers to the solution-treated sample. 122

Fig. 6.18. The modified JMAK plots for Avrami exponents (m) during isothermal ω-phase transformation for as-built and solution-treated samples at (a) 300 and (b) 325 °C. AB refers to the as-built sample and ST refers to the solution-treated sample. 123

Fig. 6.19. Variation of mean hardness with the inverse of square root of mean width of α-phase after ageing the AM Ti-5553 β-Ti alloy samples. SA1 refers to the single ageing with fast heating rate, SA2 refers to the single ageing with slow heating rate, and DA refers to the duplex ageing. 125

LIST OF TABLES

Table 2.1. The heat treatment conditions for the formation of different ω-phases in β-Ti alloys. 8

Table 3.1. Chemical composition of the wrought Ti-5553 β-Ti alloy measured using ICP-AES. 34

Table 3.2. Chemical composition of Ti-5553 β-Ti alloy powder and the as-built samples used in the current work. 36

Table 5.1. Characteristics of ω_{iso} precipitates formed during ageing at 300 °C up to 8 h, and determined from the analysis of SANS data using Kratky plots. 83

Table 5.2. List of Avrami exponent (m) values along with corresponding precipitation mechanism predicted by them [165]. 95

Table 5.3. The Avrami exponent (m) and activation energy (Ea) values for entire nanoscale ω_{iso} precipitate transformation during ageing at 300 °C and 325 °C up to 8 h. 96

Table 6.1. The differences and the similarities in the precipitation behaviour of wrought and additively manufactured Ti-5553 β-Ti alloy. 120

Table 6.2. The Avrami exponent (m) and activation energy (Ea) values for entire nanoscale ω_{iso} precipitate transformation during ageing at 300 °C and 325 °C up to 8 h. 124

CHAPTER 1

INTRODUCTION

1.1 Motivation

The β titanium (Ti) alloys are important alloys from the Ti family [1]. Their outstanding specific strength, deeper hardenability and fatigue properties have gathered them considerable attention for aerospace applications such as landing gears and load-bearing bulkheads [2–4]. These desirable properties are highly dependent on the microstructure of the material, which itself is sensitive to the heat treatment conditions [5–7]. For example, a duplex-aged (300 °C/8 h + 600 °C/ 1 h) sample exhibited higher strength but lower ductility due to the refinement of α strengthening phase [8]. The balanced mechanical properties were obtained by designing a complex heat treatment cycle producing a better combination of refined intragranular α-phase (controlling strength) and discontinuous grain boundary α-phase (controlling ductility) for Ti–5Al–5Mo–5V–1Cr–1Fe β-Ti alloy [9]. However, a better understanding of the influence of different heat treatment parameters on the microstructure evolution to achieve balanced properties through a simple heat treatment process is needed. The availability of microstructure-property relationship data at different heat treatment conditions will also benefit β-Ti users in optimising the use of the material. Further, metastable isothermal ω-phase precipitates act as the nucleation site for the α strengthening phase, hence, a better understanding of the precipitation kinetics of these precipitates in the material will enable precise control and optimisation of the alloy properties.

Recently, a need for a quick and economical way to develop these alloys has arisen due to a desire for shorter product development cycles. This can be achieved by an additive manufacturing technique due to its capability to produce intricate shapes in shorter times with less wastage of material [10]. The unsustainable buy-to-fly ratio of wrought Ti alloys and the long lead time in conventional manufacturing have been other reasons for the attraction towards the additive manufacturing processes. However, due to the rapid cooling rates associated with additive manufacturing, the microstructure of the additively manufactured (AM) β-Ti alloy is quite distinct and consists of solely β-phase, which does not provide the required material properties [11]. Besides, the ageing response of AM β-Ti alloys is not understood and requires the development of a specific post-processing pathway to obtain a substantial improvement in the AM β-Ti alloys. Hence, critical evaluation and understanding of AM β-Ti alloys are necessary to support the potential application in the aerospace sector by establishing the correlation between the obtained microstructure and the resulting mechanical properties.

1.2 Contributions of the Dissertation

This present work provides important insights into the phase transformations occurring in the wrought (conventionally produced) and AM β-Ti alloy as a function of different heat treatment parameters. These heat treatment parameters influence the size, morphology, and volume fraction of the phases that are precipitated out from the β-phase. A deeper understanding of this will enable a tailored microstructure with balanced mechanical properties within shorter processing time (*i.e.* a reduced processing complexity). The influence of sub-structure formation in the AM alloy was also explored to see the subsequent effect on the microstructure after ageing. Ti–5Al–5V–5Mo–3Cr wt% (Ti-5553), a metastable β-Ti alloy system, was selected for this work due to its desirable properties for high strength applications and wider use in the aerospace industry [12].

High-end characterisation techniques such as small-angle neutron scattering (SANS) and electrical resistivity measurement were performed to study the *in situ* nucleation and growth kinetics of phase transformations as a function of heat treatment parameters. Additionally, scanning electron microscopy (SEM), energy dispersive spectroscopy (EDS), electron backscatter diffraction (EBSD) and X-ray diffraction (XRD) were used to understand the variability in the microstructural features. These techniques were also used to complement the nucleation and growth kinetics study. A Vickers' microhardness tester was used to measure the microhardness of the samples to establish the relationship between microstructure and the associated mechanical properties. A direct laser deposition technique, Laser Engineered Net Shaping (LENS), was employed to produce Ti-5553 β-Ti alloy to understand the difference in the precipitation behaviour of AM β-Ti alloy when compared to wrought alloy.

1.3 Structure of the Thesis

This dissertation is divided into seven chapters. Chapter 2 presents a general outline of the fundamentals of phases and the transformations that occur in the β-Ti alloys. The importance of Ti-5553 β-Ti alloy and the usage of additive manufacturing to produce β-Ti alloys are also presented. Chapter 3 describes the processing of the materials used and the heat treatment procedures used to achieve the objectives of the current work. The different characterisation techniques used to establish a fundamental understanding of phase transformations are also explained in this chapter. Chapter 4 marks the beginning of the results obtained for the current work. The chapter explains the influence of different ageing approaches on the microstructure and the associated mechanical properties for the wrought Ti-5553 β-Ti alloy. The obtained results are compared with past research to highlight the advantage of the current work. This chapter ends with a motivation to understand the precipitation kinetics of the β to ω-phase transformation. Chapter 5 clarifies the precipitation kinetics of β to ω-phase transformation with the help of SANS and electrical resistivity measurements. At the end of this chapter, the need for additive manufacturing to produce these alloys is justified. Chapter 6 talks about the understanding of phase transformations occurring in AM Ti-5553 β-Ti alloy as a function of different heat treatment conditions. The influence of sub-structures on the aged microstructure is also explained. Chapter 7 summarises the findings from the current experimental results and ends with the potential future work possibilities.

CHAPTER 2

LITERATURE REVIEW

This chapter primarily focuses on the fundamental concepts of β-Ti alloys that are required to achieve the objectives of this work. The chapter commences with the classification of Ti alloys as presented in section 2.1. The description of equilibrium and non-equilibrium phases observed in β-Ti alloys, and their crystallography is explained in section 2.2. Section 2.3 presents the influence of different heat treatment parameters on the phase transformation behaviour of β-Ti alloys. A critical review of the phase transformations in the Ti-5553 metastable β-Ti alloy is provided in section 2.4. This is followed by a review of additively manufactured β-Ti alloys in section 2.5.

2.1 Titanium Alloys

Ti alloys are the alloys that contain Ti as the major alloying element. Based on the composition of the alloy and the room temperature stability of the constituent phases, Ti alloys are classified as α, near α, α + β, and β alloys, where the β-Ti alloys are further classified as metastable and stable β alloys [13]. The categorisation of different Ti alloys based on their position on the β isomorphous phase diagram is shown in Fig. 2.1.

2.1.1 α Titanium Alloys

α-Ti alloys (*e.g.,* Ti–5Al–2.5Sn) are the alloys that consist of neutral alloying elements (Sn) and/or α-phase stabilising elements (Al, O). These are not heat treatable and exhibit solely α-phase at room temperature. These alloys are used in chemical industry applications such as heat exchangers and pressure vessels due to their remarkable creep and corrosion resistance.

2.1.2 Near α Titanium Alloys

Near α-Ti alloys (*e.g.,* Ti–6Al–SN–4Zr–2Mo) contain a small amount (≤ 2 wt%) of β stabilising elements (Mo, V) producing ~10 vol% of β-phase. These are mainly used in high-temperature applications in the aerospace industry.

2.1.3 α + β Titanium Alloys

α + β Ti alloys (*e.g.,* Ti–6Al–4V) consist of 4–6 wt% of β stabilising elements that leads to the formation of 5–40 vol% of β-phase at room temperature. These alloys can lead to Martensitic transformation (M_S; Fig. 2.1) whilst fast cooling from the β-phase region. These alloys can be heat treated and can produce a variety of microstructures leading to different mechanical properties. These alloys are used in biomedical and aerospace applications.

2.1.4 β Titanium Alloys

β-Ti alloys derive their name from the stabilisation of high volume fraction of the β-phase at room temperature whilst rapidly cooling from temperatures above the beta-transus temperature (T_β) [13]. This is done by adding enough concentration of β-phase stabilising elements (e.g. Mo, V, Cr) [14]. Metastable and stable β-Ti alloys contain around 10–15 wt% and 30 wt% of β-phase stabilising elements, respectively. Metastable β-Ti alloys can produce an α-phase volume fraction of > 50%, whilst stable β-Ti alloys exhibit solely β-phase. Metastable β-Ti alloys are heat treatable and their mechanical properties can be controlled by controlling the size, shape and volume fraction of the α-phase precipitated from the β-phase matrix. Metastable β-Ti alloys are used in aerospace application whilst stable β-Ti alloys are not produced commercially.

This work deals with a metastable β-Ti alloy (Ti-5553), which is hereafter referred as a β-Ti alloy.

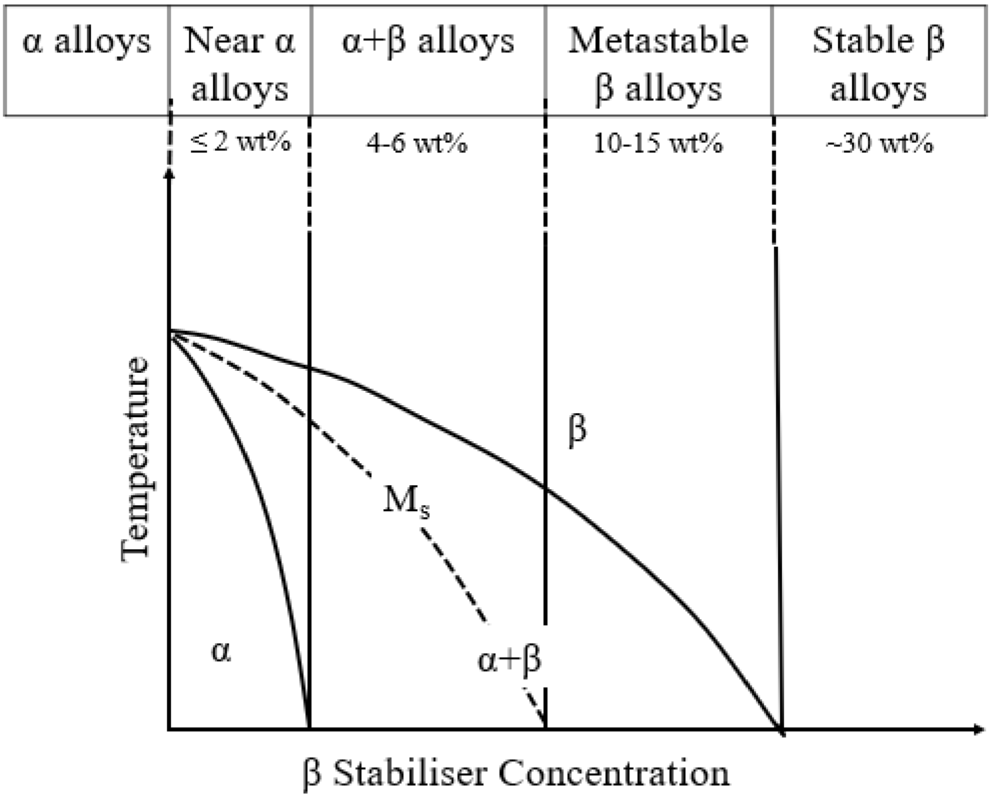

Fig. 2.1. Classification of Ti alloys based on their position on the β isomorphous phase diagram {redrawn from [13]}.

2.2 Phases in β Titanium Alloys

Titanium primarily exhibits two equilibrium allotropes: low-temperature hexagonal closed-packed (hcp) α-phase and high-temperature body-centred cubic (bcc) β-phase (at 1 atm pressure) [13,15]. This allotropic transformation takes place above T_β. This temperature of transformation, during slow heating or slow cooling, is primarily dependent on the alloying additions, *i.e.* purity of the metal [15]. A metastable ω-phase has also been observed in β-Ti alloys [16]. The metastable ω-phase can be broadly classified into three categories based on its process of formation: (i) an athermal ω-phase (ω_{ath}, 3-4 nm), which is formed during rapid cooling from above the T_β

temperature due to the partial collapse of the {111} planes of bcc β-phase due to a shuffle mechanism [16,17]; (ii) an isothermal ω-phase (ω_{iso}, 5-50 nm), which is a continuation of ω_{ath} and forms during the subsequent isothermal ageing at low temperatures (~300°C) due to thermally activated diffusion phenomena leading to a full collapse of {111} planes of bcc β-phase [16], and (iii) a deformation-induced ω-phase, which is formed due to the applied stress and/or strain [18,19]. The heat treatment conditions for the formation of different ω-phases in β-Ti alloys are summarised in Table 2.1.

Table 2.1. The heat treatment conditions for the formation of different ω-phases in β-Ti alloys.

Type of ω-phase	Heat treatment condition
Athermal ω-phase	Formed during rapid cooling from above the T_β temperature after solution treatment
Isothermal ω-phase	Either formed during isothermal ageing at ~300 °C or during slow heating (~5 °C/min) below 450 °C

The bcc β-phase belongs to the $Im\bar{3}m$ space group and its unit cell is shown in Fig. 2.2 (a), whilst the α-phase belongs to the P63mmc space group with hcp unit cell shown in Fig. 2.2 (b) [13,15,20]. The stability of β-phase at higher temperatures is due to its ability to accommodate higher vibrational entropy due to its open structure[1], which leads to the lower Gibbs free energy of the phase at elevated temperatures [21].

---

[1] BCC structure has a low packing density, hence exhibiting low co-ordination number. This provides a higher degree of freedom to absorb more energy leading to greater entropy and stability at higher temperature.

The typical equilibrium α-phase in β-Ti alloys is precipitated by either ageing it in the α/β region or slow cooling it from above T_β [22,23].

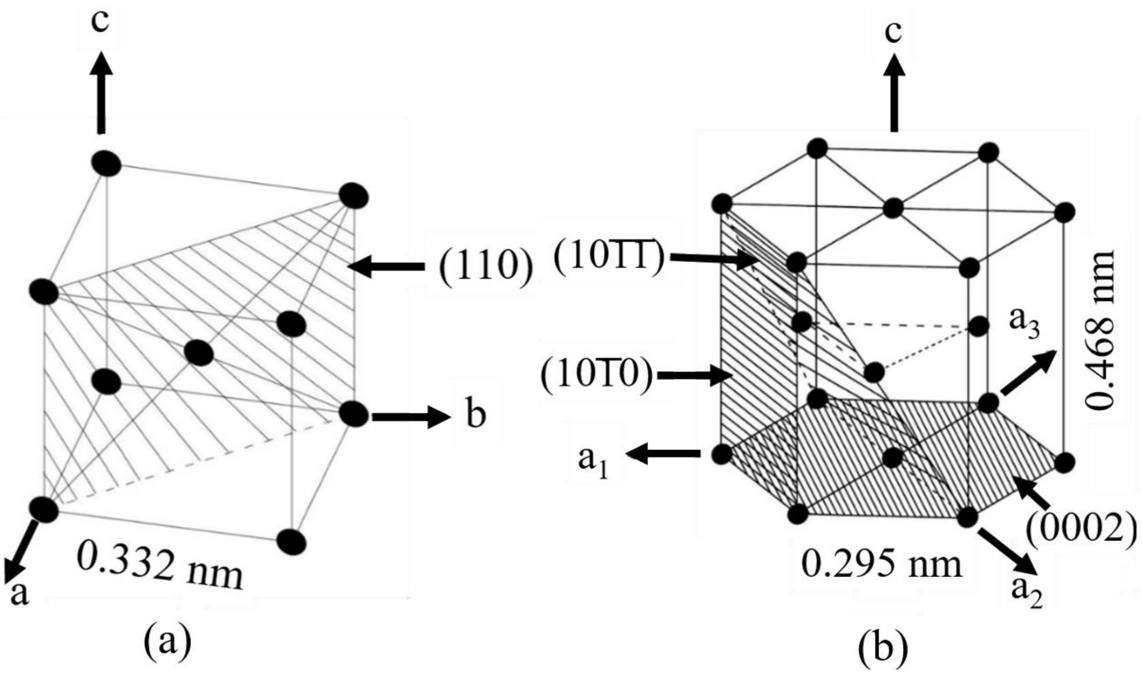

Fig. 2.2. (a) Crystal structure of bcc β-phase, and (b) crystal structure of hcp α-phase {redrawn from [13]}.

An ideal ω-phase possesses a non-close packed hexagonal unit cell [24] and depending on the extent of the phase transformation, the space group of ω-phase can be either p6/mmm or p-3m1. For the early-stage transformation, ω-phase exhibits a trigonal symmetry, whilst for transformation completion, ω-phase has a hexagonal symmetry. The trigonal symmetry of ω-phase in the early stages of the phase transformation is postulated to generate diffuse intensity spots in selected area electron diffraction instead of sharp ω spots, under transmission electron microscopy (TEM) [25].

The formation and stability of the phases are also dependent on the concentration of different alloying elements in the alloy. The alloying elements are primarily classified as α- and β-phase stabilisers depending on whether they increase or decrease

T_β to stabilise either α or β-phase. Substitutional element Al, and interstitial elements such as O, N, C are used as α-phase stabilisers. Some other elements such as B, Ga, and Ge can also be used as α-phase stabilisers, however, only Al is primarily used due to its high solid solubility in both α and β-phase. These α-phase stabilisers shift the T_β temperature upwards depending on the concentration of alloying elements, as shown in Fig. 2.3. The effectiveness of these α-phase stabilisers is calculated using an Al equivalency number as given below [13]:

$$[\mathrm{Al}]_{eq} = [\mathrm{Al}] + 0.17\,[\mathrm{Zr}] + 0.33\,[\mathrm{Sn}] + 10\,[\mathrm{O} + \mathrm{C} + 2\mathrm{N}]$$

The β-phase stabilisers are classified as β isomorphous and β eutectoid forming systems. These alloying elements lower T_β and allow the β-phase to be stable at lower temperatures, as shown in Fig. 2.3. Ti with V, Mo, Nb, Ta or Hf are β isomorphous systems and form solid solutions at most temperatures. Fe, Cr, Mn, Co, Ni, Cu, W, Au, Ag, Pt and Pd are β eutectoid forming systems due to the formation of a eutectoid compound at certain temperatures [13]. Some of the β isomorphous systems undergo a β-phase separation into β (solute rich) and β' (solute lean) at higher β stabilising element concentrations, as shown in the phase diagram in Fig. 2.4. This is essentially due to the positive enthalpy of mixing of these elements leading to a positive curvature of the free energy composition plot of β-phase. The phase separation leads to the precipitation of α-phase from either β′ or β/β′ interface [13]. The phase diagram also illustrates a superimposed region of the ω-phase formation. Additions of β stabilisers are also known to lower the martensitic start temperature below room temperature. This feature is used to get a quantitative value for the β-phase stabilisation effect of individual elements in terms of Mo equivalency [13]. The Mo equivalency is calculated as follows:

$$[\mathrm{Mo}]_{eq} = [\mathrm{Mo}] + 0.22[\mathrm{Ta}] + 0.28\,[\mathrm{Nb}] + 0.44\,[\mathrm{W}] + 0.67[\mathrm{V}] + 1.6\,[\mathrm{Cr}] + 1.25\,[\mathrm{Ni}] + 1.7\,[\mathrm{Mn}] + 1.7\,[\mathrm{Co}] + 2.9\,[\mathrm{Fe}]$$

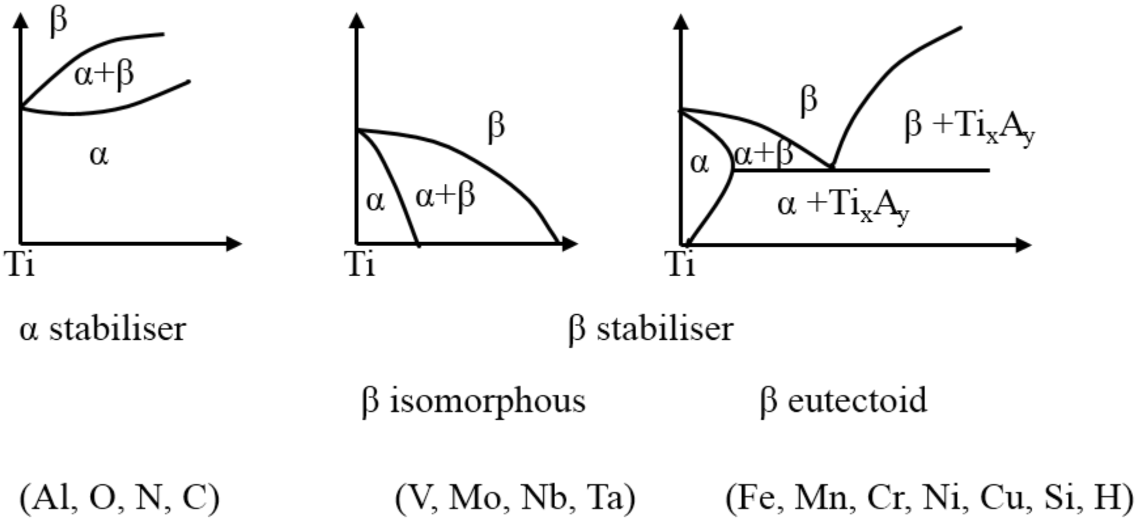

Fig. 2.3. Effect of alloying elements on phase diagrams of Ti alloys {redrawn from [13]}.

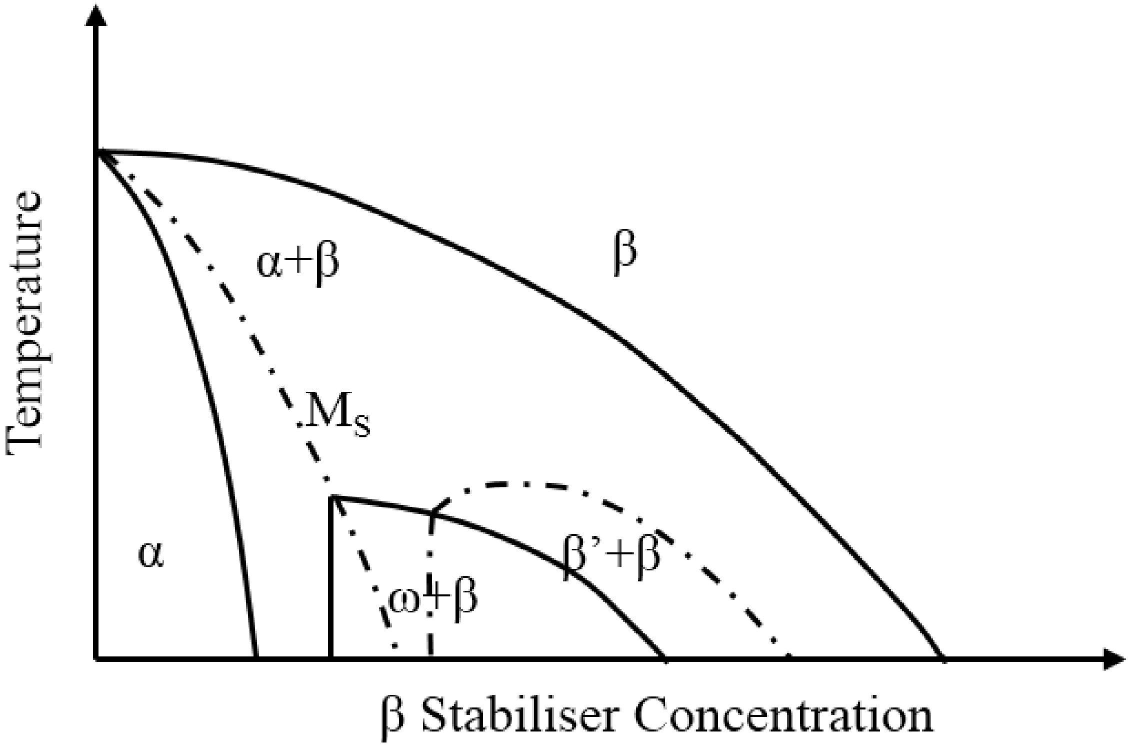

Fig. 2.4. Schematic phase diagram for β isomorphous Ti alloys showing metastable ω-phase and phase separation as β+β' {redrawn from [13]}.

2.3 Phase Transformations in β Titanium Alloys

2.3.1 β to α-phase Transformation

The β to α-phase transformation occurs after either slowly cooling the material from above T_β or ageing it in the α/β region (Fig. 2.4). This transformation occurs due to a non-classical pseudo-spinodal decomposition mechanism, where the small compositional fluctuations in the β-phase during heat treatments provide sufficient activation energy for the nucleation of α-phase [26]. The final properties of β-Ti alloys are influenced by the size, morphology, volume fraction, and the distribution of α-phase precipitate in the β-phase [27–29]. These microstructural features are critically controlled by the heat treatment parameters, such as cooling rate, heating rate, ageing temperature and ageing time [7,30–34].

Depending on the nucleation site, the α-phase predominantly appears as: an allotriomorphic phase that precipitates along the prior β-phase grain boundaries; a grain boundary Widmanstätten α-phase that nucleates at the allotriomorphic α-phase and grows into the β-phase matrix; an intragranular Widmanstätten α-phase that nucleates within the β-phase; an intergranular α-phase which grows from grain boundary α-phase into the β-phase; and an intragranular α-phase where the α-phase precipitates within the β-phase at the dislocation sites, a precursor metastable ω-phase, and the other inclusions [35–40]. All these features of α-phase are shown in Fig. 2.5. The growth of intragranular and grain boundary α-phase during β to α-phase transformation happens due to the diffusion of α stabilising elements (Al and O) in the β-phase matrix [9,41]. The intragranular α-phase primarily controls the strength of the alloy, whilst the grain boundary α-phase controls the ductility of the alloy [9,41].

Fig. 2.5. Microstructure of Ti alloys showing the (a) Allotriomorphic & Widmanstätten α-phase [42], and (b) intergranular & intragranular α-phase [43].

Depending on the heat treatment parameters, different morphologies of the α-phase precipitates were reported. For example, an acicular α-phase morphology was observed when β-Ti alloys were aged between 500°C and 700°C [23,44–47], whilst a chevron-shaped α-phase morphology was obtained during the ageing at the temperature of ~400°C [48], as shown in Fig. 2.6 (a) and (b) respectively. The acicular α-phase formed during heat treatments also showed three different α variants arranged in a self-accommodating cluster morphology having a triangular arrangement (Fig. 2.6 (a)) [12]. These three variants share a common $\{11\bar{2}0\}\alpha//\{111\}\ \beta$ poles. The (0001) planes of the α variants lie parallel to {011} β plane, and each makes an angle of 60° with the other two [49]. The clustering of these α variants happens to reduce the overall strain energy via the self-accommodation principle [50,51] because the formation of α-phase leads to the straining of the β-phase matrix. The internal structure of a chevron consisted of a major and smaller α lath, where the smaller lath nucleated from the major lath via sympathetic nucleation [48]. Colonies of lamellar α-phase, as shown in Fig. 2.6 (c), were reported when the β-Ti alloy was slowly cooled (2°C /min) from above T_β after solution treatment to the ageing temperature. This heat treatment cycle was termed as beta annealed, slow cooled and aged heat treatment cycle [14,22,23,52]. A better combination of strength and ductility was obtained for the material containing lamellar-acicular α-phase in its microstructure [23]. The Burgers orientation relationship observed between α and β-phase is given below [53]:

$$(0001)\alpha \| \{011\}\beta;\ <11\bar{2}0>\alpha \| <1\bar{1}1>\beta; \{11\bar{0}0\}\alpha \| \{121\}\beta$$

Fig. 2.6. Microstructure of Ti alloys showing the morphology of α-phase as (a) acicular [54], (b) chevron-shaped [48], and (c) lamellar [43].

The controlled precipitation of fine and un-deformable α-phase in the β-phase matrix produced higher yield strength in β-Ti alloys [55–58]. However, such a higher strength can also lead to the loss in ductility due to α-phase refinement [59–62]. A better combination of refined intragranular α-phase (controlling strength) and discontinuous grain boundary α-phase (controlling ductility) led to higher ultimate tensile strength (~1111 MPa) alongside higher ductility (~12.5%) for Ti–5Al–5Mo–5V–1Cr–1Fe β-Ti alloy [9]. This goal was achieved via a specially designed and complex heat treatment pathway. A better understanding of the influence of different heat treatment parameters on the microstructure evolution can help in achieving the balanced properties in β-Ti alloys through simple heat treatment processes. For example, balanced mechanical properties (~1265 MPa + 9% elongation) were obtained when β-Ti alloys were directly aged at 600 °C for 1 h [8]. This was achieved due to the nonuniform size and distribution of α-phase in the β-phase matrix. This led to the presence of distinct lamella spacing and undulating interface assimilating more plastic dissipation. However, there is a need to explore a wider range of ageing temperatures and ageing time to have a more critical understanding of the relationship between ageing parameters and the obtained mechanical properties, especially for Ti-5553 metastable β-Ti alloy.

The influence of different heat treatment parameters on the microstructure evolution in other β and α+β Ti alloys have been studied previously [63–69]. The coarser α-phase precipitates obtained at higher ageing temperatures (~600°C-700°C) and longer ageing time led to the improved ductility of the material, but the strength of the material was greatly reduced [27,28,70]. In contrast, fine α-phase precipitates were observed at lower temperatures (~400°C-500°C) and the lower ageing time leading to higher strength but reduced ductility [5,35,71–75]. Moreover, higher heating rates have also led to the coarsening of the α-phase and hence giving improved ductility but reduced strength [30,31,76–79]. Thus, there is a great need to explore the influence of a combination of heat treatment parameters such as different heating rates, ageing temperatures, and ageing time. This will help in understanding the material behaviour that is important for optimising the ageing parameters and obtaining balanced mechanical properties.

2.3.2 β to ω-phase Transformation

In the beginning, the ω-phase was found to show an embrittlement effect on the Ti alloys [80], however, in the later stages numerous experiments have been performed on it to understand its complex morphology, kinetics, and most importantly the interplay between ω and α-phase leading to refined α-phase precipitates, which provides higher strength to β-Ti alloys [81–85]. Based on the morphology, ω-phase can be present with either a cuboidal or ellipsoidal shape depending on the lattice misfits between ω and β-phases. The critical lattice misfit magnitude has been reported as 0.5%, below which the morphology will be ellipsoidal, and higher misfit values will lead to the cuboidal morphology of ω-phase [25]. The high misfit binary alloys of Ti-V, Ti-Cr, Ti-Mn, and Ti-Fe are reported to have a cuboidal morphology due to the reduction in elastic energy of the matrix, whilst the low misfit binary alloys of Ti-Mo and Ti-Nb are shown to have ω-phase with ellipsoidal morphology facilitating minimisation of anisotropic surface energy [12]. The orientation relationship observed for this transformation is given as [24]: $[111]_\beta \parallel [0001]_\omega$; $(11\bar{0})_\beta \parallel (112\bar{0})_\omega$

Several high-end characterisation techniques have been used to characterise the formation of this nanoscale ω-phase from the decomposition of β-phase [17,54,94,86–93]. Jones *et al.* [91] used *in situ* synchrotron X-ray diffraction and they reported that the embryonic ω-phase formed during rapid cooling from above the T_β correlate to form the final athermal ω-phase at a lower temperature. Coakley *et al.* [95] used SANS to understand the precipitation behaviour of isothermal ω-phase formation during low-temperature (300 °C) ageing up to 8 h, where the volume fraction of isothermal ω-phase was found to be increased during the ageing process [18,87,95,96]. Although there have been numerous research investigations [17,54,94,86–93] carried out on the ω-phase formation mostly during quenching and subsequent isothermal ageing, the effect of cooling rate (after solution treatment) on β to isothermal ω-phase transformation, in terms of microstructure evolution, and its subsequent phase transformation kinetics is still not studied. This necessitates further investigation to understand the microstructural evolution and precipitation kinetics for β to isothermal ω-phase transformation. Understanding the influence of different cooling rates is highly important for structural applications in the aerospace industry because the section thickness may determine the achievable cooling rate and therefore can affect the mechanical properties. Furthermore, these data may help clarify the thermodynamic understanding of the isothermal ω-phase precipitation from the parent β-phase matrix. Recently, Chen *et al.* [97] reported that the formation of isothermal ω-phase precipitates during low-temperature (300 °C) ageing is influenced by the cooling rates from the solution treatment temperature of Ti–6Cr–5Mo–5V–4Al β-Ti alloy. Their TEM studies qualitatively showed that the number density of isothermal ω-phase precipitates increased with more rapid cooling. However, an in-depth quantitative understanding of the evolved microstructure is required to precisely control and optimise the mechanical properties. In addition, due to the small volume of samples, TEM is unable to easily provide statistical information about the path leading to final desired microstructure. A high-end technique such as SANS can serve this purpose because it has the ability to provide information for a far larger volume of sample than TEM, whilst probing the precipitates of size in the range of 1–100 nm [98,99]. SANS is especially interesting due to its ability to probe the three-dimensional structural information of the material at the nanoscale [95,100]. In addition, the electrical resistivity measurements during these transformations can also help in deriving the thermodynamic information such as the activation energy for precipitation [101].

2.3.3 ω-phase-Assisted α-phase Nucleation

Fine and uniformly distributed α-phase precipitates leading to high strength can be obtained by allowing isothermal ω-phase-assisted α-phase nucleation [3,102–106]. As explained in section 2.3.2, isothermal ω-phase exhibits two types of morphologies: cuboidal and ellipsoidal. Cuboidal ω-phase generated in the high lattice misfit systems leads to the nucleation of α-phase precipitates at the ledges of ω/β interface, which was recently characterised using scanning transmission electron microscopy (STEM) and atom probe tomography (APT) [107]. However, there have been different explanations for the ω-phase-assisted α-phase nucleation in low misfit systems: (i) α-phase precipitates nucleate inside the ω-phase due to a displacive mechanism, as shown in Fig. 2.7 [108]. (ii) α-phase nucleates at the ω/β interface due to the rejection of α-phase stabilisers (Al and O) at the interface, as shown in Fig. 2.8 [12]. (iii) Mixed-mode transformation, which states that α-phase first nucleates at the ω/β interface due to the rejection of α-phase stabilisers, such as Al and O and then it grows rapidly into the ω-phase due to a displacive mechanism whilst it grows into the β-phase matrix very slowly due to diffusion, as shown in Fig. 2.9 [109].

This item has been removed due to 3rd Party Copyright. The unabridged version of the thesis can be found in the Lanchester Library, Coventry University.

Fig. 2.7. High-resolution images showing the nucleation of α-phase platelets in the core of a ω-phase via displacive mechanism [108].

Fig. 2.8. Dark-field TEM image recorded with <113> β zone axis, showing α-phase at the β/ω interface [12].

Fig. 2.9. Schematic diagram of the ω-assisted α-phase formation [109].

In a recent attempt to understand the interplay between ω and α-phase, high-angle annular dark-field (HAADF) imaging mode under STEM was used [40]. They also performed a phase-field simulation to see the effect of misfit strain, where it was found that the rejection of α-phase stabiliser to the ω/β interface reduces the stress field associated with the ω-phase. This leads to a reduction in the activation energy required for the α-phase nucleation [40]. However, some researchers also reported that ω-phase does not have a direct role to play whilst they introduced a new mechanism called pseudo-spinodal mechanism, where the α-phase was observed to precipitate from the compositionally depleted pockets formed in the β-phase [110]. Later, this confusion was aggravated when it was reported that ω-phase plays an indirect role in the α-phase nucleation and was proposed to activate the pseudo-spinodal effect from different compositional pockets, rich and lean at high and low temperatures, respectively [111]. In an attempt to answer the questions on the role of ω-phase and the relative contribution of composition partitioning and misfit strain for nucleation of α-phase, Li *et al.* [112] showed that the α-phase does not nucleate directly from the ω-phase until it reaches a critical size from incommensurate embryonic ω-phase to the commensurate isothermal ω-phase. They also reported that misfit strain contributes as a major portion in the nucleation of α-phase from ω-phase. In their other work [113], they explained that the misfit strain only contributes to convert the coherent ω/β interface to semi-coherent ω/β interface during ageing at low temperature (~300°C) up to 48 h, where the ledges and local enrichment of oxygen at the semi-coherent ω/β interface provide the activation energy required for the α-phase nucleation [113]. From the literature researched, although the results from *ex situ* studies, it could be argued that isothermal ω-phase does have a direct or indirect role to play for α-phase nucleation. Hence, it becomes important to understand the kinetics of isothermal ω-phase to precisely control and optimise the mechanical properties. It is also important to clarify the role of isothermal ω-phase on α-phase nucleation at different temperatures, whether it is direct or indirect.

The use of high-end *in situ* characterisation via SANS and electrical resistivity measurements can make better sense of these questions due to their ability to track minor constitutional changes in the material at the nanoscale [101,114].

Moreover, this transformation is also affected by the heat treatment parameters due to their direct effect on the ω-phase transformation [17]. Recently, it has been shown that the slower heating (~5°C/min) rate has led to the nucleation of ω-phase at a lower temperature of ~300°C and leading to the refined α-phase precipitation in the final microstructure after ageing at higher temperature [40,95]. The ω-phase formation was found to be absent at a higher heating rate (~84°C/min) [54]. Besides, the higher cooling rate has been found to increase the isothermal ω-phase precipitation by affecting the solute partitioning during the cooling process from the higher temperatures [97,115]. However, there is no clear evidence on the thermodynamics and kinetics of the isothermal ω-phase formation as a function of cooling rate after solution treatment. Also, deconvolution of precipitate size, shape and volume fraction has not been presented, warranting further investigation. This understanding will enable designing a better and simple heat treatment pathway for the best use of the β-Ti alloys in industry.

In addition to these efforts to understand isothermal ω-phase-assisted α-phase precipitation, several attempts have been made to improve the performance of the β-Ti alloys by exploiting the isothermal ω-phase-assisted α-phase precipitation via the duplex ageing procedure [104,116,117]. The main concept behind duplex ageing is to perform the ageing process in two steps, *i.e.* first to allow the isothermal ω-phase to grow in size and number density at a lower temperature of ~ 300°C and then directly raise the temperature to the desired ageing temperature for allowing the α-phase to grow from already precipitated isothermal ω-phase. It has been demonstrated that a more homogenous and fine distribution (Fig. 2.10) of α-phase precipitates can be obtained by duplex ageing in contrast to the single ageing procedure leading to improved mechanical properties [116]. This led to higher levels of hardness and strength values but reduced ductility [8,118], whilst some researchers also reported a good balance of strength and ductility via duplex ageing [116]. Ren *et al.* [8] reported a very low ductility of ~2% after duplex ageing, although, the ultimate tensile strength reported was quite higher (~1368 MPa). This behaviour was attributed to the presence of refined and uniformly distributed α-phase that led to flat interfaces between the intragranular precipitates and the grain boundary. The duplex aged samples also showed the presence of precipitate free zones (PFZ) near the grain boundaries (Fig. 2.10). The formation of PFZ is attributed to the diffusion of α stabilisers (Al and O) to the grain boundaries from the adjacent areas contributing to the growth of grain boundary α-phase [9]. The ageing temperatures and ageing time exploited for duplex ageing were very limited. There is further scope for investigation of ω-phase-assisted α-phase nucleation kinetics due to wide window of ω-phase and α-phase temperatures.

Fig. 2.10. SEM micrograph of a duplex-aged sample aged at 600 °C for 1 h [8].

2.4 Ti-5553 β Titanium Alloy and its Importance

The Ti-5553 is a metstable β-Ti alloy that is a modified version of a Russian alloy VT-22, which was developed for high-performance aerospace applications [3]. In comparison to the other β-Ti alloys, it offers good quenchability by avoiding the transformation of any other phase during the cooling period, leading to greater control on microstructure during heat treatment. Depending on the microstructure, this alloy can offer a high ultimate tensile strength of ~1200 MPa with good ductility (~14 %) and toughness. This alloy offers excellent specific strength and high-cycle fatigue properties in comparison to the most widely used Ti–6Al–4V [23,27]. Therefore, this has replaced the other competing alloys such as Ti–10V–2Fe–3Al β-Ti alloy in aerospace applications [14,27]. Moreover, Boeing has preferred this alloy over other alloys [2,27]. However, it is worthwhile to mention that the properties of Ti-5553 β-Ti alloy are greatly affected by its microstructure, which is sensitive to the heat treatment parameters. As a result, a detailed investigation is required to understand the microstructural evolution as a function of different heat treatment parameters.

Typically, for Ti-5553 alloy, an athermal ω-phase and isothermal ω-phase precipitates from the β-phase [23,95]. The isothermal ω-phase is observed either during low-temperature (~300 °C) ageing or when a slow heating rate (5°C/min) is used to reach the ageing temperature [40,119]. For higher heating rates (~84°C/min) isothermal ω-phase does not precipitate and instead an orthorhombic α″-phase is observed, which evolves towards the hcp α-phase at higher temperatures [54,120]. α″-phase is also observed during subsequent ageing at low temperatures (~325°C to 425°C) after either direct quenching to these temperatures or quenching to room temperature first and subsequently raising the temperature at the high heating rate [120–122]. This is reported to be formed by the diffusionless process [87].

The heat treatment pathways followed so far by researchers to understand the phase precipitation in Ti-5553 β-Ti alloy mainly focused on the single ageing process after solution treatment. These heat treatment cycles follow either the direct rapid cooling from above T_β to the ageing temperature or rapid cooling to the room temperature followed by subsequent ageing. Mainly, the heat treatment cycles used were centred around the two heat treatment cycles, *i.e.* beta annealed, slow cooled and aged, and solution-treated and single aged, as shown in Fig. 2.11 and Fig. 2.12 respectively [23,27,95]. Both these heat treatment cycles involve single-step ageing after the solution treatment stage, where the beta annealed slow cooled and aged heat treatment cycle involves controlled cooling (2°C/min) after the solution treatment to the desired ageing temperature, whilst in the solution-treated and single aged conditions the desired temperature is set for ageing after solution treatment. However, the temperature window for the formation of the α strengthening phase is quite wide and the characteristics of the α-phase, such as size and shape, are affected by the heat treatment parameters. Therefore, the study of microstructure evolution as a function of different combinations of ageing parameters such as different heating rate, different ageing temperature and ageing time can help in optimising the mechanical properties with simple heat treatment processes. The influence of duplex ageing [8] and the slow heating [123] was also explored, but the ageing temperatures and ageing time exploited were very limited and has left a scope to further optimise the ageing parameters. This will help in better utilising the advantages of duplex ageing and slow heating leading to balanced mechanical properties for β-Ti alloys. The improved strength after duplex ageing and single ageing after slow heating was primarily attributed to the refinement of α-phase precipitates due to isothermal ω-phase assisted α-phase nucleation during duplex ageing. However, Zheng *et al.* [111] reported that as the ageing temperature is increased, isothermal ω-phase has an indirect role to play in the refinement of the α-phase precipitates. Hence, it is important to understand the precipitation mechanism during these single ageing and duplex ageing approaches.

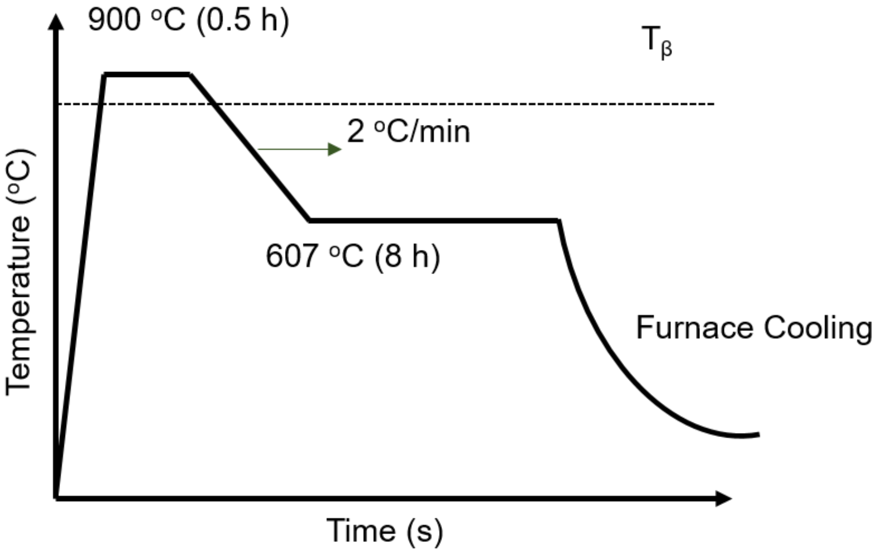

Fig. 2.11. Beta annealed, slow cooled and aged heat treatment cycle.

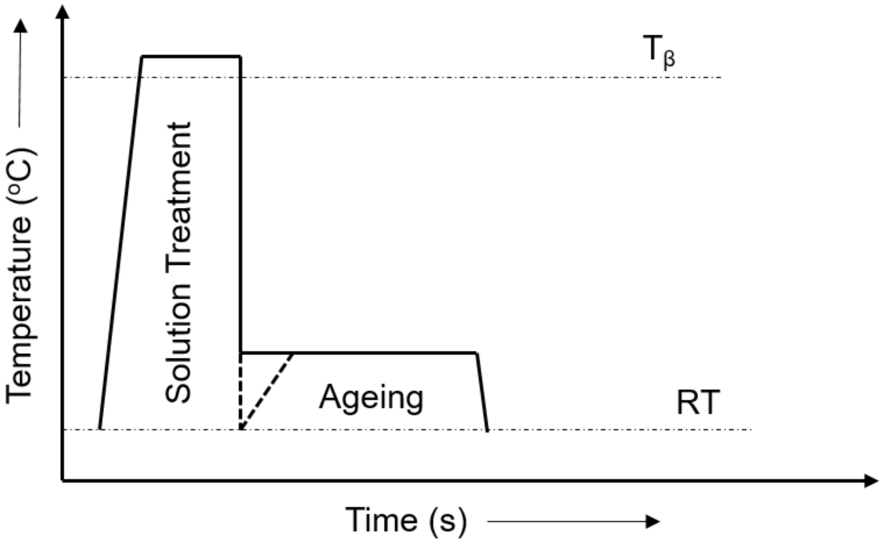

Fig. 2.12. Solution treated and single aged heat treatment cycle.

It has also been reported that the cooling rate after the solution treatment affects the size of α-phase precipitates [42,77]. Also, the cooling rate affects the precipitation kinetics of isothermal ω-phase [97], however, there are still some questions unanswered for Ti-5553 β-Ti alloy: (i) There is a need to better understand the behaviour of the material under duplex ageing parameters that can provide the desired combination of mechanical properties. (ii) The influence of different heat treatment conditions such as heating rate, ageing temperatures, and ageing time on microstructure evolution during single ageing should be studied extensively because there is a wide temperature window for the formation α-phase, hence, a better understanding of the microstructural evolution in the material can help in designing the simple heat treatment steps to obtain better mechanical properties. The availability of microstructure-property relationship data at different heat treatment conditions will lead to the better utilisation of the Ti-5553 β-Ti alloy. (iii) There is a need to clarify the role (direct or indirect) of isothermal ω-phase on α-phase precipitation during different ageing approaches and at different ageing temperatures. (iv) There is a need to study the kinetics of isothermal ω-phase as a function of cooling rate. A higher cooling rate has shown to shorten the isothermal ω-phase precipitation [97], which may help in obtaining the desired properties in short processing times. The deconvolution of the isothermal ω-phase as a function of cooling rate is also important to precisely optimise the microstructure evolution. This will further enable understanding of the effect of cooling rate on the section thickness for structural applications in the aerospace application.

2.5 Additive Manufacturing

In the modern era, additive manufacturing is a widely accepted technology in producing industrial parts ranging from orthopaedic implants to aircraft components due to its capability to produce complex shapes in less time with less wastage of material [10]. Due to the increased scientific understanding of these methods, they are now getting wider attention in fabricating net-shaped Ti alloy components for aerospace applications [10].

Although the β-Ti alloys possess good properties such as high specific strength and deeper hardenability, with the cast and forged material [124], however, their wide-scale use is restricted to only high-value components due to high cost [125]. This high cost wrought alloys is because of the multi-step and energy-intensive processes such as forging, casting, machining, and thermomechanical processing. The cost of producing wrought Ti alloys can be broken down into two parts as per reference [126]: Cost of ingot (~50%) and cost of processing (~50%). The proper breakdown of the cost for wrought alloy production is shown in Fig. 2.13. The majority of the Ti alloy parts are prepared using forging at a slow speed that produces large scrap, up to 95% of the raw material [127]. Hence, the additive manufacturing of titanium alloys for aerospace is attractive due to design and near net shape benefits [10]. There are several variants of additive manufacturing such as blown powder deposition under direct laser deposition category, and selective laser melting under the powder bed fusion category [128,129]. The direct laser deposition is beneficial because it provides a high deposition rate and wider processing window to fabricate larger items in comparison to the other metal-based additive manufacturing methods [128]. It has the potential to produce exact dimensions for high-value components in aerospace and military industries. Besides, direct laser deposition provides a relatively excellent density, better metallurgical bonding, precise deposition, and minimal distortion and microcracking, hence making it a better tool for processing high-value components [128,130].

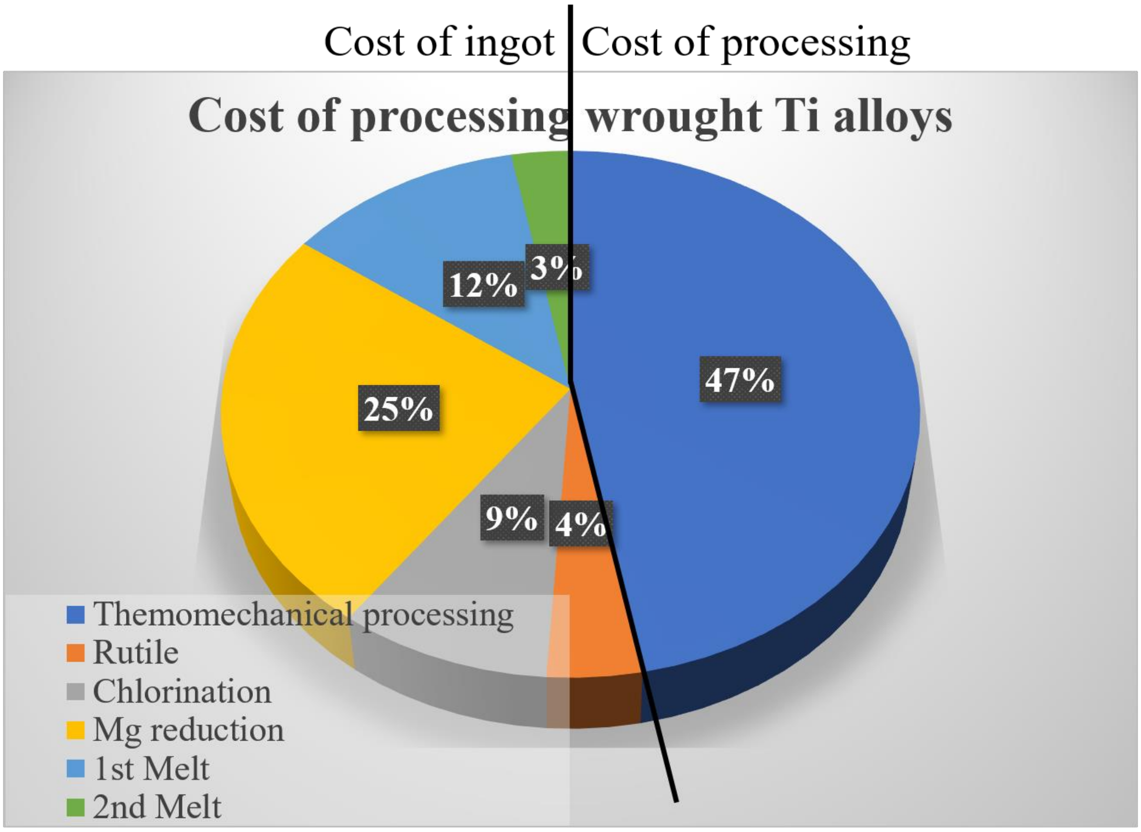

Fig. 2.13. The breakdown for the processing cost of wrought Ti alloys [126].

Ti-5553 β-Ti alloy is mostly processed by selective laser melting [11,131], where Carlton *et al.* [132] recently reported the influence of single ageing on the mechanical properties of the selective laser melting built Ti-5553 β-Ti alloy. However, a detailed understanding of the effect of microstructural features on the mechanical properties was not presented. Besides, there is a need to understand the evolution of microstructural features as a function of different ageing conditions because there is a wide window of temperatures and time for the formation of α-phase. It was also reported that Ti-5553 β-

Ti alloy can be deposited using direct laser deposition with less porosity in the microstructure [133,134]. The inherent rapid cooling rates associated with direct laser deposition led to the formation of solely β-phase in the as-built condition that does not provide the desired mechanical properties [11]. The bimodal (α+β) microstructure was produced after *in situ* dwelling (*i.e.* switching off the laser beam) and *in situ* annealing (*i.e.* laser scanning without feeding powder) after each layer to get the desired properties. However, an inhomogeneous microstructure was observed after *in situ* dwelling and *in situ* annealing that led to the variation in the microhardness at different locations [131]. This variation in the microstructure from top to bottom was reported to be because of the different thermal history, where the bottom region had more chances to get to the ageing temperature of 600 °C hence producing more α-phase at the bottom region compared to the top region (maintained at a higher temperature) that was dominated by β-phase. The laser deposited samples showed anisotropy in the mechanical properties [135] and the aged samples showed better mechanical properties for other types of titanium alloys when compared to the most widely used mill annealed alloys [10]. Hence, the post-processing of these samples was recommended to obtain the minimum required properties and performance consistency [10]. However, the ageing response of direct laser deposition built β-Ti alloys is not understood and requires the development of a specific post-processing pathway to obtain a substantial improvement in the direct laser deposition built β-Ti alloys. The critical evaluation and understanding of direct laser deposition built β-Ti alloy will support the potential application of additive manufacturing in the aerospace sector. It is also very important to understand whether the AM alloy can be directly used in the applications instead of the wrought alloy. The microstructure of the AM samples just after the deposition is unique and exhibits the presence of the sub-structures (Fig. 2.14) in the β-phase grains [11]. Therefore, it is important to understand the influence of these sub-structures on the aged microstructure of AM T-5553 β-Ti alloy.

As understood from section 2.3.3, isothermal ω-phase-assisted α-phase nucleation during duplex ageing and slow heating has been used to obtain the refined intragranular α-phase precipitates to get higher microhardness in the wrought material. Therefore, it is important to study the response of these ageing treatments on the AM samples. This will help in clarifying the precipitation behaviour of the AM material with respect to the wrought material. This will enable better utilization of the additive manufacturing technique to produce β-Ti alloy parts. Since isothermal ω-phase influences the formation of α strengthening phase, therefore, it is also important to understand the precipitation kinetics of isothermal ω-phase in AM β-Ti material to better control and optimise the mechanical properties.

Fig. 2.14. Cellular/cellular-dendritic solidification of the melt [11].

2.6 Research Gaps

Based on the literature, the following research gaps have been identified:

- The duplex ageing treatments can produce balanced mechanical properties. However, the temperature region explored is limited and there is further scope to optimise the ageing parameters. The characteristics of α strengthening phase such as shape and size (which control the mechanical properties) are also influenced by the heat treatment parameters. Therefore, the study of microstructure evolution as a function of different combinations of ageing parameters such as different heating rate, different ageing temperature and ageing time is necessary to optimise the mechanical properties with simple heat treatment processes.
- The isothermal ω-phase has been seen to affect the nucleation of α strengthening phase, hence, there is a need to understand the kinetics of potent nucleant isothermal ω-phase as a function of the different cooling rate which might be useful in achieving the desired properties in shorter processing time during duplex ageing. Also, there is a need to deconvolute the variation in size, shape, and volume fraction of the isothermal ω-phase as a function of cooling rate. Understanding the influence of cooling rate is important for controlling the section thickness in structural applications. It is also important to clarify the role (direct or indirect) of isothermal ω-phase on α-phase nucleation during different ageing approaches and at different ageing temperatures.
- The microstructures and properties of the AM Ti-5553 alloy is already studied in powder bed processing. Limited study is done on net-shape processing such as

LENS. Also, the ageing properties of these alloys need to be known for better use of AM alloy. This will enable the better use of additive manufacturing methods for producing β-Ti alloy parts. This will also help in developing a precise pathway for post-processing of AM β-Ti alloy samples, generating a good balance of properties in comparison to the wrought Ti-5553 β-Ti alloy.

2.7 Research Questions

The key questions which are aimed to be addressed through this work are given below:

- What is the relationship between the microstructural features and the mechanical properties of the wrought Ti-5553 β-Ti alloy as a function of single ageing (using different heating rates) and duplex ageing at different ageing temperatures for varied ageing times?
- What is the role (direct or indirect) of isothermal ω-phase on α-phase nucleation during different ageing approaches and at different ageing temperatures?
- How are the kinetics of isothermal ω-phase affected as a function of different cooling rate after solution treatment? What difference does different cooling rate cause in terms of the precipitation pathways of the isothermal ω-phase?
- What is the ageing response of the AM Ti-5553 β-Ti alloy and how is it different from the wrought Ti-5553 β-Ti alloy? How do the sub-structures in the as-built condition affect the microstructure of the aged sample?

CHAPTER 3

EXPERIMENTAL METHODOLOGY

This chapter presents the heat treatment procedures and the detailed description of characterisation tools used in this work. The chapter begins with an introduction to the material used in this work and its processing routes.

3.1 Material and its Processing

For the current work, the Ti-5553 β-Ti alloy, used in this research, was prepared using two processing routes as explained below.

3.1.1 Conventionally Made or Wrought Alloy

The conventionally prepared or wrought alloy was obtained from TIMET. The chemical composition of the alloy as measured using inductively coupled plasma atomic emission spectroscopy (ICP-AES) is mentioned in Table 3.1. The material provided was given in the form of discs of size ø160 mm × 15 mm that were cut from the end of a billet. The photograph of one such disc is shown in Fig. 3.1. The disc was forged at 815 °C with several reheats following the initial recrystallisation at 960 °C and subsequent air quenching. For further heat treatment experiments, the discs obtained were sectioned into samples of size 40 mm × 15 mm × 15 mm using electrical discharge machining (EDM). The microstructure and the microhardness variations in the disc were also studied by examining the samples from different locations (1, 2, and 3) marked on the disc in Fig. 3.1. The SEM micrographs and the microhardness values taken from these locations are shown in Fig. 3.2. The surface parallel to the plane of the paper in Fig. 3.1 was examined for all the characterisations. The results (Fig. 3.2) indicate that the microstructure and the microhardness values at different locations are similar. This indicates that the final microstructure and the microhardness results after ageing will not be affected by the location from where the samples were extracted.

Table 3.1. Chemical composition of the wrought Ti-5553 β-Ti alloy measured using ICP-AES.

Elements (wt%)	Mo	V	Al	Cr	Zr	Fe	Co	C	O	Nb	Ti
	4.81	4.59	5.51	2.97	<0.01	0.33	<0.01	0.02	0.045	<0.01	Bal

Fig. 3.1. Photograph of the Ti-5553 β-Ti alloy disc obtained from TIMET. 1, 2, and 3 are the marked locations from where the samples were extracted to check the variations in the microstructure and the microhardness values in the disc.

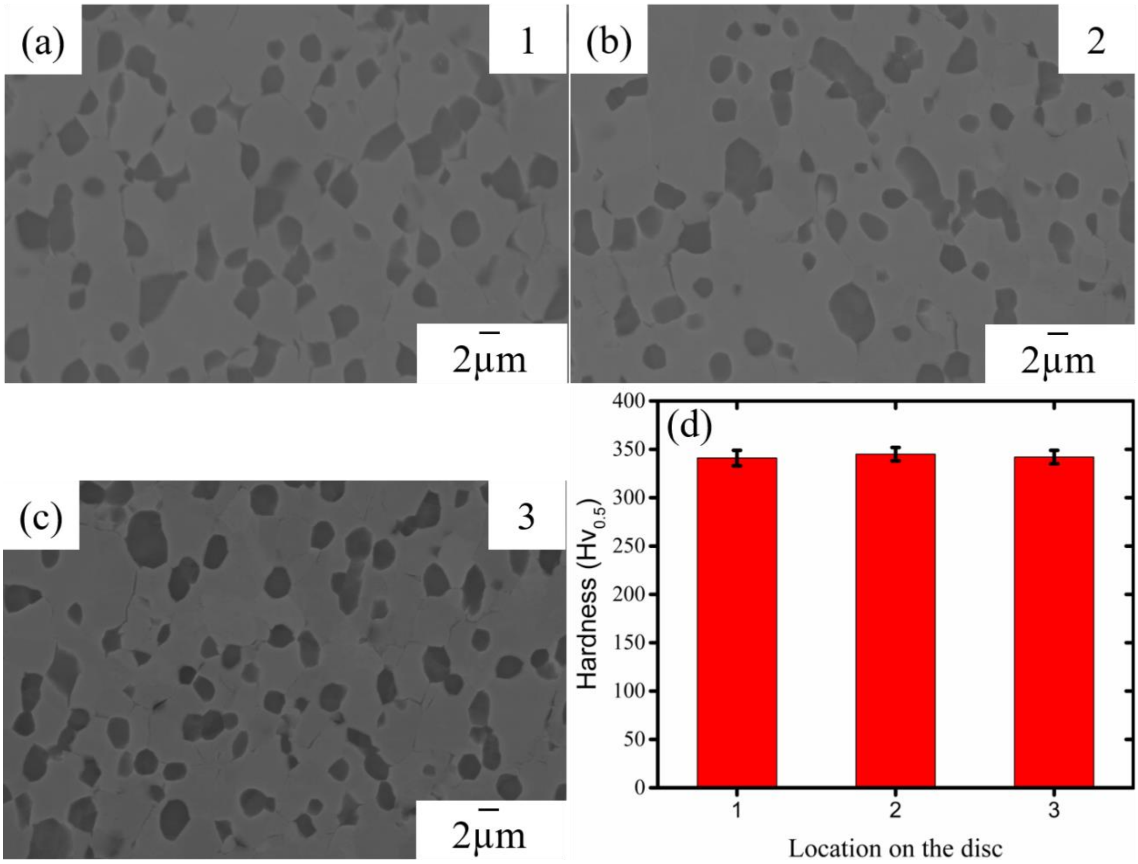

Fig. 3.2. The SEM micrographs and the microhardness values taken from different locations (1,2, and 3) marked on the disc in Fig. 3.1.

3.1.2 Additively Manufactured Alloy

Gas-atomised spherical Ti-5553 β-Ti alloy powder was obtained from AP&C company as a starting material. The chemical composition of the powder, measured using ICP-AES, is presented in Table 3.2. The typical appearance of the as-received powder is shown in Fig. 3.3 (a). The particle size distribution was calculated using SEM images, where the particles lied in the range of 16–148 µm, and the average size was calculated as 64 ± 34 µm. The particle size distribution is also presented in Fig. 3.3 (b). The double walls (40 mm × 10 mm × ~1.5 mm) of Ti-5553 β-Ti alloy were manufactured in an OPTOMEC LENS MR-7 system equipped with a 1 kW IPG Fiber Laser System. The chemical composition of the as-built samples is shown in Table 3.2.

The Al content (4.98 wt%) of the as-built samples decreased with respect to Al content (5.04 wt%) in the powder. This is because of the evaporation of Al at high temperature of additive manufacturing processes [136]. The oxygen content (0.1 wt%) in the as-built sample was found to be more than the oxygen content (0.065 wt%) in the powder. This is because of the oxygen pick up during high-temperature additive manufacturing processes [136]. The schematic of the deposition track profile is shown in Fig. 3.4. The typical appearance of the double-wall samples can be seen in Fig. 3.5. The laser power, feed rate and scanning speed during the build are 300W, 6g/min and 635 mm/min, respectively. The laser spot size was 0.25 mm. The oxygen concentration was contained within the range of 2-18 ppm during the building process. The melt pool overlap is about 50% and the layer thickness along the build direction was 0.254 mm.

Table 3.2. Chemical composition of the Ti-5553 β-Ti alloy powder and the as-built samples used in the current work.

Elements (wt%)	Mo	V	Al	Cr	Zr	Fe	Co	C	O	Nb	Ti
Powder	5.08	4.52	5.04	2.86	<0.01	0.36	<0.01	<0.01	0.065	<0.01	Bal
As-built Sample	5.10	4.54	4.98	2.86	<0.01	0.38	<0.01	0.01	0.1	<0.01	Bal

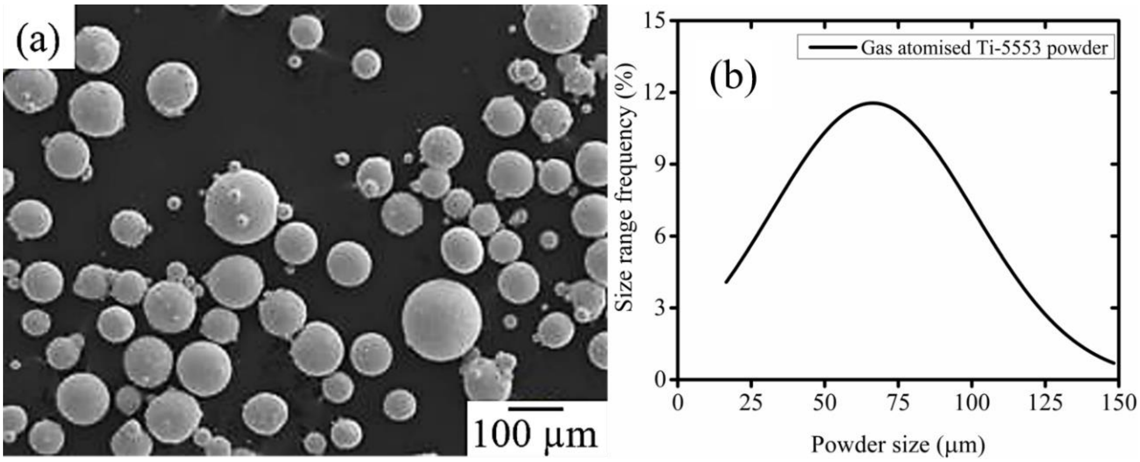

Fig. 3.3. (a) Typical appearance of Ti-5553 β-Ti alloy powder used for producing the additively manufactured samples. (b) shows the particle size distribution for the gas atomised Ti-5553 β-Ti powder used in this work.

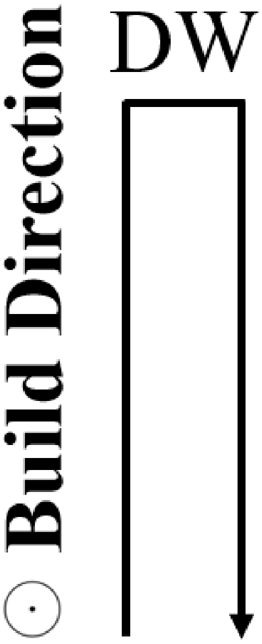

Fig. 3.4. The deposition track profile for depositing the double-wall (DW) samples.

Fig. 3.5. The typical appearance of the double-wall sample after deposition.

3.2 Heat Treatment Procedures

3.2.1 Solution Treatment

The wrought Ti-5553 β-Ti alloy samples (40 mm × 15 mm × 15 mm), sectioned from the disc, were first ground on all sides using 320 grit size SiC abrasive paper to clean the surface. These samples were then coated with a Bonderite L-GP 12 Acheson coating to minimise the oxidation and the formation of α-case on Ti-5553 β-Ti alloy samples during the solution treatment. The samples were dried for a day before the solution treatment. The solution treatment was done at 900 °C (above T_β) for 0.5 h followed by rapid cooling to room temperature via different cooling rates: water quenching (Chapter 4 & 5) or air cooling (Chapter 5); depending on the objective of the work. The solution treatment was performed in a pre-heated and a well-calibrated tube furnace under argon gas (industrial grade) with a flow rate of 10 l/min. An N-type thermocouple having a diameter of 3 mm was used to measure the solution treatment temperature and cooling rate. The solution treatment temperature was maintained within ± 2 °C. The thermocouple was fixed with high-temperature adhesive to a hole at the centre of a reference sample (40 mm × 15 mm × 15 mm). The reference sample was kept inside the furnace along with the to-be solution treated samples. The average cooling rate was measured as ~0.5 °C/s and ~20 °C/s for air cooling and water quenching, respectively. The cooling rate curves obtained from the thermocouple are shown in Fig. 3.6.

A few AM samples were also solution treated (for Chapter 6) similarly as the wrought alloy to dissolve the sub-structures formed after deposition. This was done to study the influence of sub-structures on the microstructure after ageing. All the AM samples were only water quenched after solution treatment. Before solution treatment, the AM samples were ground on all sides up to 600 µm grit size SiC paper to remove the oxidised layer formed during deposition.

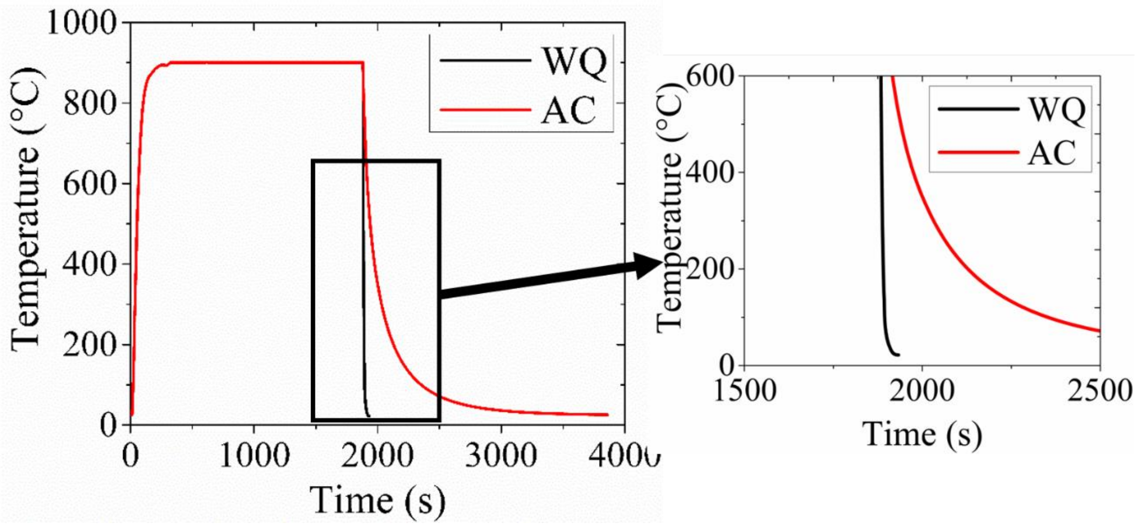

Fig. 3.6. The cooling rate measurement curves for water quenching (WQ) and air cooling (AC) after solution treatment. The figure also shows the enlarged data around the 2000 s to highlight the difference between the cooling rates.

3.2.2 Ageing Treatment

Before ageing, the wrought (solution-treated) and the AM (solution-treated and as-built) samples were ground on all the sides up to 600 µm SiC paper to remove the developed oxide layer and the α-case. These samples were further sectioned to 10 mm × 15 mm × 15 mm and 10 mm × 10 mm × 1.5 mm, respectively. A Struers precision cut-off machine (Secotom-50) was used to cut these dimensions. The sectioned samples were aged at the chosen ageing temperatures for the chosen ageing time to observe the microstructural changes and determine the microstructure-property relationship. The detailed information on ageing parameters is given in the respective results chapters. Overall, the ageing was done using three different heat treatment pathways: (i) the samples were slowly heated to the desired ageing temperature – the samples were kept in the furnace at room temperature, and then the temperature was raised at ~5 °C/min, (ii) the samples were fast heated to the desired ageing temperature – ageing was done in a pre-heated furnace that produced a heating rate of ~100 °C/min, and (iii) the samples were duplex aged – the samples were first pre-aged in a pre-heated furnace at 300 °C for 8 h and then the sample was quickly shifted to another furnace pre-heated at a higher temperature. The ageing treatments were carried out under argon gas maintained at a flow rate of 10 l/min. The samples were also coated and dried before the ageing treatments, same as for the solution treatment. All the single ageing treatments were carried out in a tube furnace, whilst a combination of tube and chamber furnaces was used to perform the duplex ageing. Similar to the solution treatment procedure, an N-type thermocouple was used to measure the ageing temperature and heating rate. The ageing temperatures were maintained within ± 2 °C.

3.3 Characterisation Tools

3.3.1 Metallography

The wrought and AM samples were prepared using standard metallographic procedures for SEM, EDS, EBSD, XRD and Vickers' microhardness characterisation. The sectioned samples were mounted in 2″ mount using the hot mounting procedure on a Struers' hot mounting machine (CitoPress-15) to examine the cross-section. The cross-section was mechanically ground up to 1200 μm SiC abrasive papers followed by polishing using diamond suspension down to 1 μm. Subsequently, the samples were finally polished using vibratory polishing with colloidal silica having 0.02 μm particle size. After polishing, the samples were cleaned in distilled water for 0.25 h by ultrasonic cleaning.

3.3.2 Scanning Electron Microscopy (SEM)

The microstructures of the wrought and AM samples were examined using backscatter electron (BSE) imaging in a Zeiss Gemini Sigma 500VP SEM operating at an accelerating voltage of 20 kV. The best contrast for BSE micrographs to detect α and β-phases was obtained at an aperture size of 60 µm.

3.3.3 Energy Dispersive Spectroscopy (EDS)

The EDS was performed to find out the elemental composition of the sub-structures observed in the AM samples. This was performed using an X-Max^N detector from Oxford instruments installed in the same SEM, which was operated at an accelerating voltage of 20 kV.

3.3.4 Electron Backscatter Diffraction (EBSD)

The EBSD measurements were performed to find out the local misorientations, grain boundary mapping and texture in the AM samples. A NordlysNano detector from Oxford instruments installed in the same SEM was used to perform the EBSD acquisition. An aperture size of 300 µm was used to collect the large area scans. The instrument was set up at an accelerating voltage of 20 kV, whilst the working distance and the step size was kept as 8-16 mm and 0.2 µm, respectively. The build direction of the AM sample was aligned parallel to the Y direction of the instrument for EBSD measurements. The sample surface angle with respect to the horizontal plane was kept as 70°. The EBSD data were analysed using HKL Channel 5 software.

3.3.5 X-ray Diffraction (XRD)

The XRD measurements were carried using a Rigaku SmartLab X-ray diffractometer equipped with CuKα radiation operating with an applied voltage of 40 kV and a current of 30 mA. The diffraction patterns were collected in the angular 2θ range of 35° to 100° at a scan rate of 1°/min. The treatment of the XRD data, such as background determination, was performed in the Xpert HighScore Plus software. The peak phases were indexed using the previously published crystallographic data on Ti alloys [95,100].

3.3.6 Vickers Microhardness

Samples prepared for microstructural examination were also tested using a Vickers microhardness tester (using D80 Durascan-70 by EmcoTest) using a load of 0.5 kgf (Hv0.5). This was done to investigate the likely effect of phase precipitation on mechanical properties. About 40 measurements were taken for each sample.

3.3.7 Quantification of Microstructure

The microstructures after solution treatment and ageing were quantified using the ImageJ software [137]. The line intercept method was used to quantify the phase characteristics such as β grain size, the width of α-phase, interparticle spacing between the α-phase and volume fraction of α-phase in the microstructure. In order to perform the quantitative analysis using ImageJ, the image processing was done in the ImageJ software itself to create the drawings of each microstructure. Drawings were created by first reducing the bandpass filter of the images followed by the thresholding of the images. The drawings along with the corresponding SEM micrographs are shown in Fig. 3.7. The drawings look similar to the SEM micrographs. These drawings were then used to perform all the quantitative analysis.

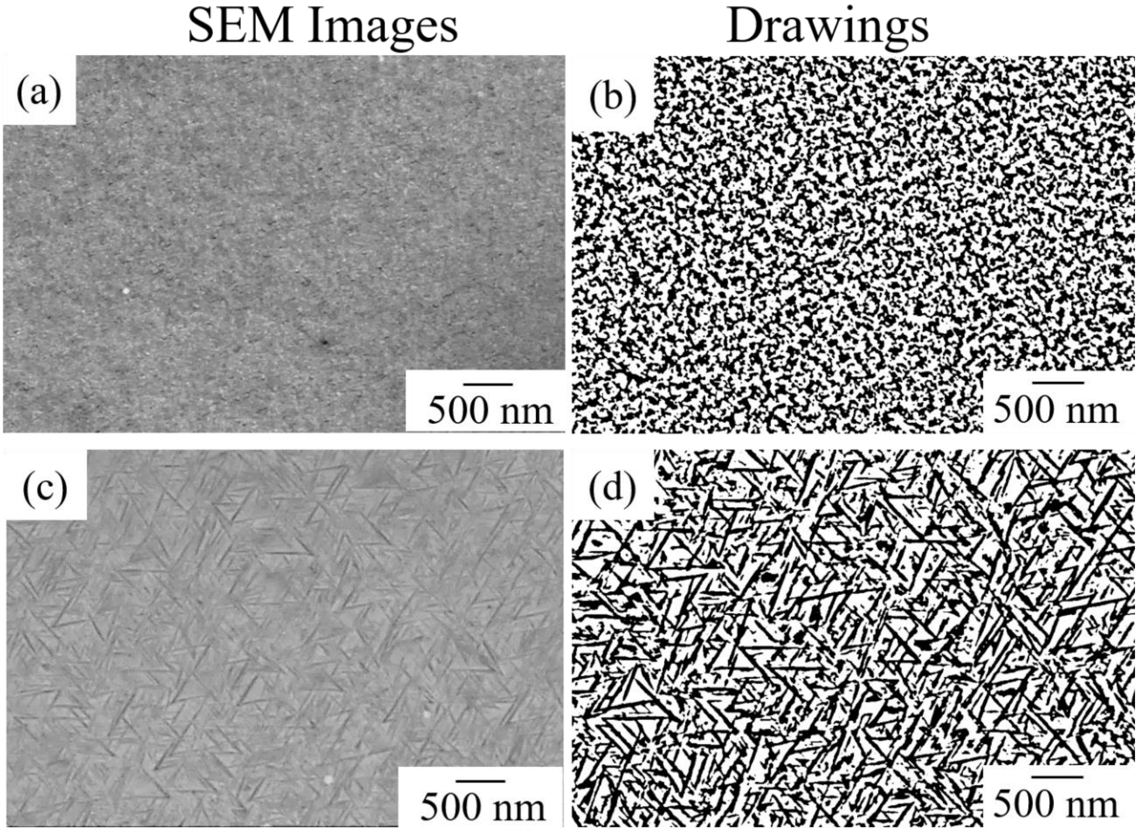

Fig. 3.7. SEM micrographs of the aged samples along with their corresponding drawings.

3.3.8 Small-angle Neutron Scattering (SANS)

The use of SANS to study precipitate evolution in engineering alloys has gathered considerable attention in the recent past due to its ability to provide full and precise structural information of nanoscale precipitates [95,100]. The SANS technique provides information for a far larger volume of sample than TEM and is still able to probe precipitates of size in the range of 1–100 nm [98,99]. The technique measures the coherent elastic scattering of the incident neutron beam from precipitates at small angles less than 10° based on the contrast variation principle, *i.e.* the difference in the scattering length densities (SLD) between the parent phase and precipitate [138].

The samples of size 20 mm × 15 mm × ~1 mm were sectioned from the solution-treated samples for SANS measurements (for Chapter 5). These samples were then polished up to 1 µm using diamond suspension. The SANS measurements were performed on the LARMOR beamline of ISIS Pulsed Neutron Source, UK. Polychromatic neutrons (λ = 0.9 to 13.3 Å) were used for measuring the scattering from the system. The detector configuration provided a momentum transfer (q) range of 0.007 – 0.7 Å, where $q = 4\pi\sin\theta/\lambda$ and the scattering angle is 2θ, and λ is the neutron wavelength. The sample scattering was measured by exposing the samples to a neutron beam of size 12 mm × 12 mm. The overall set-up of the instrument can be seen in Fig. 3.8. The schematics of the SANS experiment can also be seen in Fig. 3.9.

The measured raw SANS data were reduced to absolute SANS scattering intensities (I) using standard procedures in the Mantid software [139]; *i.e.* by correcting the data for transmission and background measurements. The data was azimuthally averaged for plotting the one-dimensional (1D) I *vs* q plots. The data were also checked for any Bragg's peak, which was not observed in the data collected. A K-type thermocouple of diameter 1 mm was attached to the surface of the sample through the sample holder to measure the ageing temperature and the heating rate during *in situ* SANS measurements. The ageing temperature was maintained within ± 2 °C. A radiant air furnace [140] was used for ageing the samples. All the measurements were performed under argon gas (industrial grade).

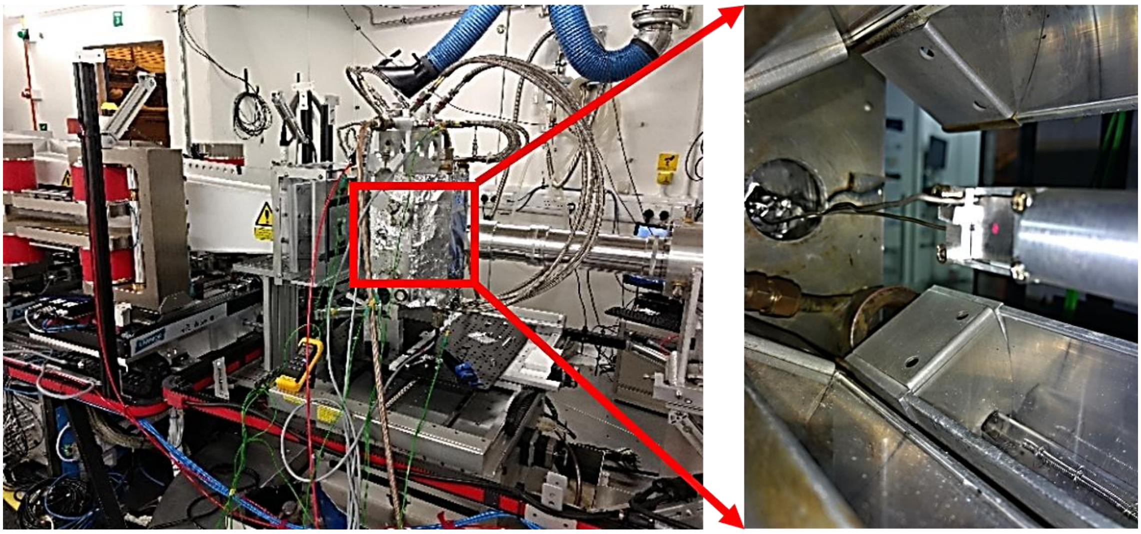

Fig. 3.8. Photograph of the LARMOR instrument set-up for *in situ* SANS experiment.

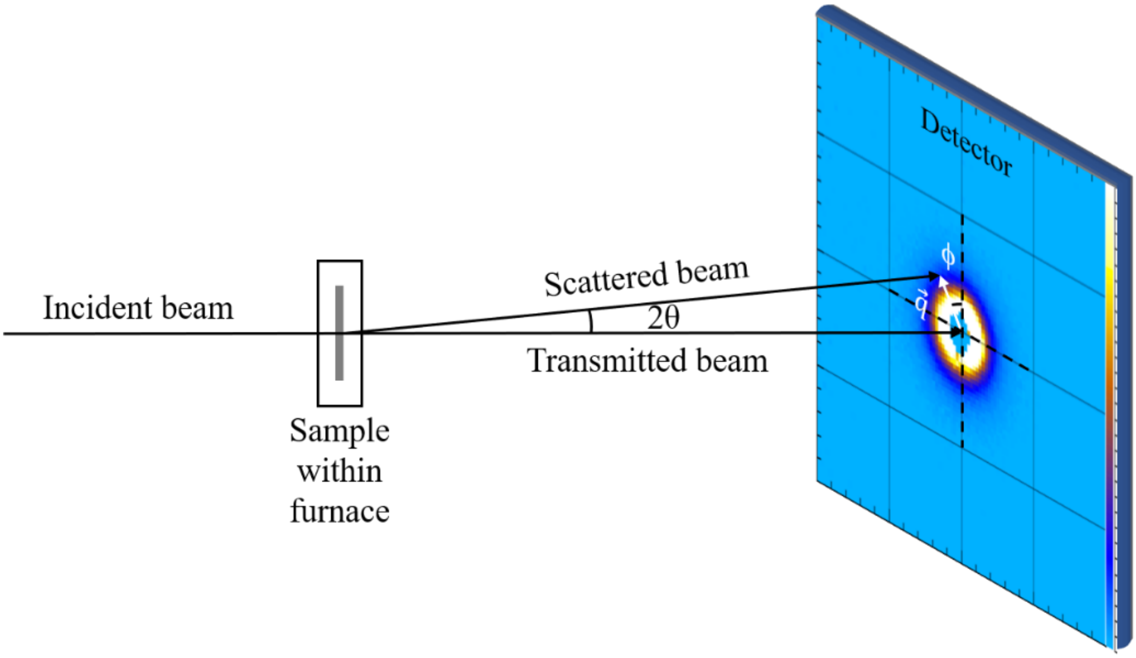

Fig. 3.9. The schematics of *in situ* SANS experiment to study the kinetics of isothermal ω-phase as a function of different cooling rate after solution treatment.

3.3.9 Electrical Resistivity Measurement

The formation of different precipitates from the β-phase matrix in the Ti alloys has also been detected by means of electrical resistivity measurements [101,122]. This is due to its high sensitivity to the minor constitutional changes in the material during quenching, heating and ageing [141]. This technique is especially interesting due to its capability to derive thermodynamic information such as the activation energy for precipitation [101].

A miniaturised multi-property test system [142] was used (for Chapter 4, 5 & 6) to *in situ* measure the electrical resistivity (using the 4-point method) during heat treatments performed under argon. The detailed information on the heat treatment parameters or pathways is presented in the relevant chapters. The typical set-up of the electrical resistivity measurement system is shown in Fig. 3.10. The working of the system can be understood from the schematics in Fig. 3.11. Matchstick samples of dimensions 40 mm × 2 mm × 1 mm were cut from the ground (up to 600 µm using SiC abrasive paper) wrought (solution-treated) and AM (solution-treated and as-built) samples using EDM. The measurements were done on the matchstick samples after grinding up to 1200 grit size SiC abrasive paper. The samples were held between the water-cooled grips, whilst a direct current was used to heat them. The electrical resistivity was measured across the central 2 mm of the sample using a Pt-Rh probe. Pt/Pt-13%Rh thermocouple wires having a diameter of 0.1 mm were used to measure the temperature of the sample. The thermocouple was spot welded to the centre of the test sample. The temperature during the measurements was maintained within ± 1 °C. The electrical resistivity (ρ) of the samples was calculated using Equation 3.1.

$$\rho = \frac{VA}{Il} \tag{3.1}$$

where V is the drop in the voltage, A refers to the cross-sectional area of the sample, I is the current and l refers to the gauge length between the potential probes. An increment of ~0.01% in electrical resistivity was calculated due to a change in the length during heating that was neglected for further data analysis.

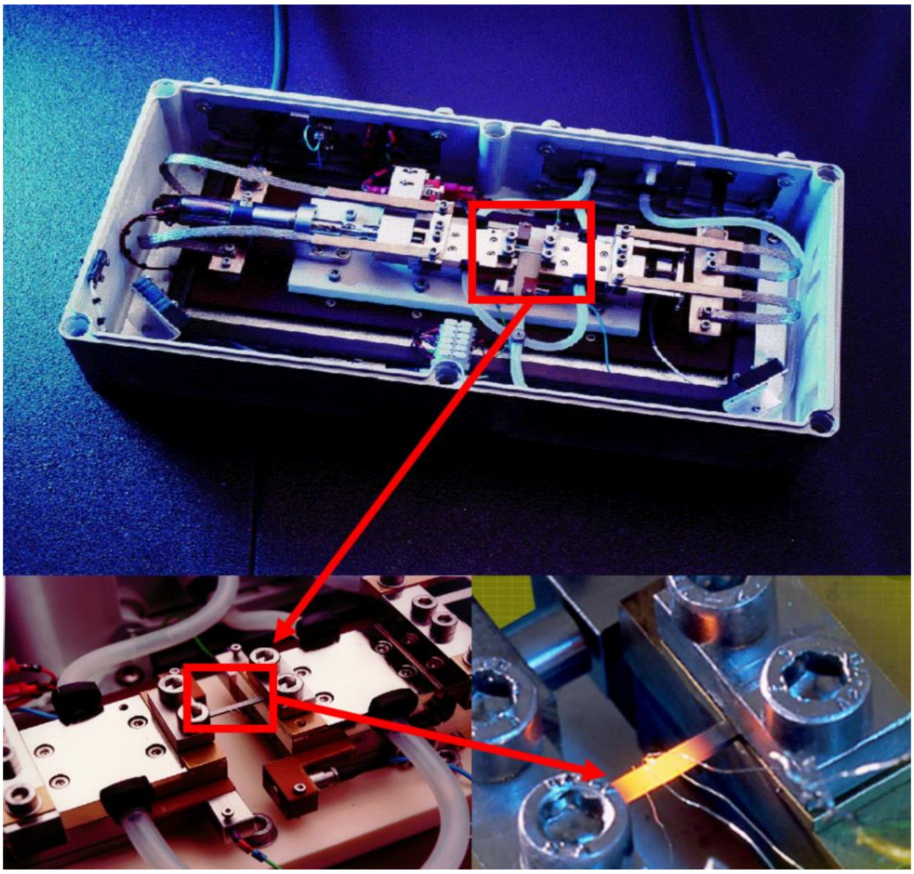

Fig. 3.10. Typical set-up of the electrical resistivity measurement system.

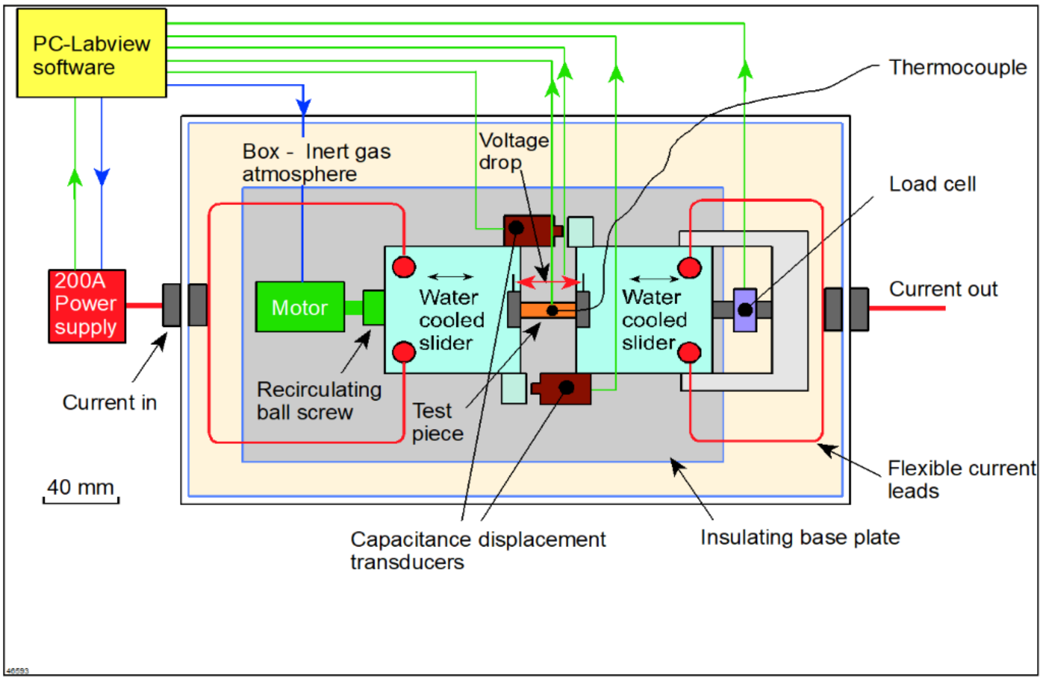

Fig. 3.11. The schematics of the electrical resistivity measurement set-up illustrating the working of the system.

CHAPTER 4

PRECIPITATION BEHAVIOUR OF SINGLE AND DUPLEX AGED WROUGHT METASTABLE β-Ti ALLOY

4.1 Introduction

As stated in the Literature Review (Chapter 2), the mechanical properties of β-Ti alloys are primarily controlled by the size, volume fraction, morphology, and the distribution of the α strengthening phase precipitates in the β-phase matrix. One of the ways to control these characteristics of α-phase precipitates is to use different ageing approaches – single ageing and duplex ageing, to get the desired final microstructure [117]. In single ageing, the homogenised alloy is aged at the temperature necessary for α-phase precipitates to nucleate by a non-classical pseudo-spinodal mechanism [26], whereas in the case of duplex ageing, pre-ageing treatment at a lower temperature (~250 °C – 350 °C) is employed to allow the precipitation of metastable isothermal ω-phase precipitates, which then act as potential nucleation sites for the α-phase precipitates at higher ageing temperatures. The refined α-phase precipitates formed in the latter process leads to improved strength in β-Ti alloys [40].

This chapter presents a comparative study of the influence of different ageing approaches on the microstructures and microhardness of wrought Ti-5553 β-Ti alloy when aged at different temperatures and for different ageing time. *In situ* electrical resistivity measurement was performed to understand the precipitation mechanism during these ageing approaches (section 4.3.4). The evolution of different microstructures as a function of these ageing approaches at different ageing conditions is presented in section 4.3.1. A correlation between the microstructure and the microhardness was established (section 4.4.4) to understand the likely effect of different microstructures on the mechanical properties.

4.2 Experimental Details

The ground and solution-treated samples of dimensions 10 mm × 15 mm × 15 mm were prepared (details in section 3.2) for ageing treatments. All solution-treated samples were water-quenched to room temperature. The ageing approaches followed for the work in this chapter were broadly classified into two types – single ageing and duplex ageing. The samples were aged at 500 °C, 600 °C and 700 °C for 0.5 h and 6 h using single ageing and duplex ageing. The schematics of the ageing treatments are depicted in Fig. 4.1. These different ageing parameters were chosen to see their influence on the obtained microstructure and the associated microhardness. All the aged samples were finally water-quenched to room temperature. For single ageing, two different heating rates, slow (~5 °C/min) and fast (~100 °C/min), were used to reach the ageing temperature. Further details on the ageing procedure is provided in section 3.2. The samples were also aged at 300 °C for 8 h to allow the precipitation of isothermal ω-phase in the low-temperature ageing step during duplex ageing. This step is hereafter labelled as a pre-ageing step.

In situ electrical resistivity measurements were also performed to understand the precipitation kinetics of the wrought Ti-5553 β-Ti alloy during different ageing approaches. The measurements were taken during the heating period up to 700 °C with high (~100 °C/min) and slow heating rate (~5 °C/min), whilst for duplex ageing, the measurements were taken during the heating period up to 300 °C and pre-ageing-step *i.e.* at 300 °C up to 8 h. The schematic of *in* situ electrical resistivity measurement of solution-treated samples is depicted in Fig. 4.2.

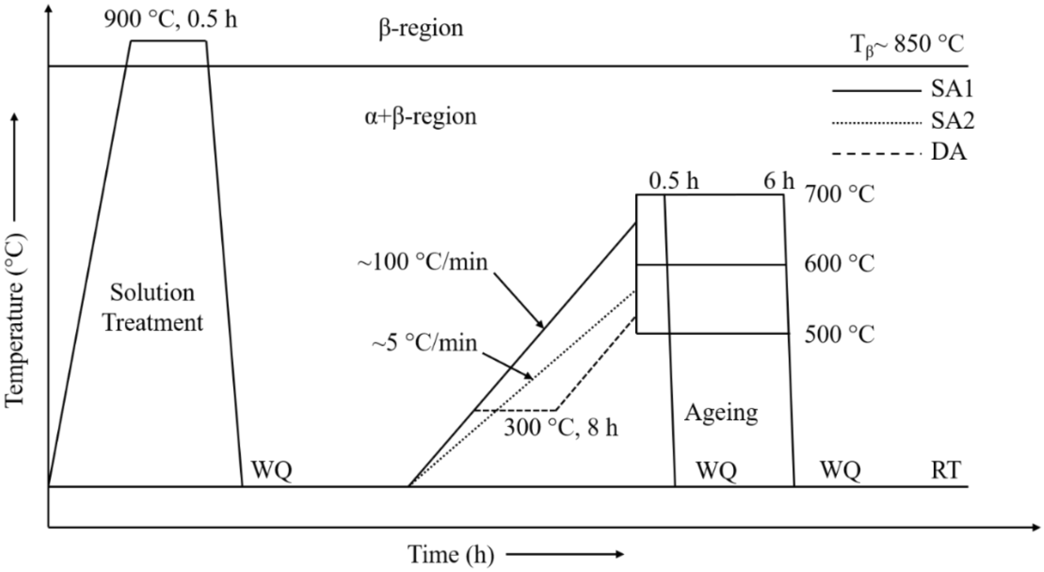

Fig. 4.1. Schematics of the heat treatment cycles used in this work to understand the influence of different ageing approaches on the microstructure evolution and associated mechanical properties of Ti-5553 β-Ti alloy. SA1 represents single ageing with fast heating rate, SA2 represents single ageing with slow heating rate, and DA represents duplex ageing approach. WQ indicates water quenching.

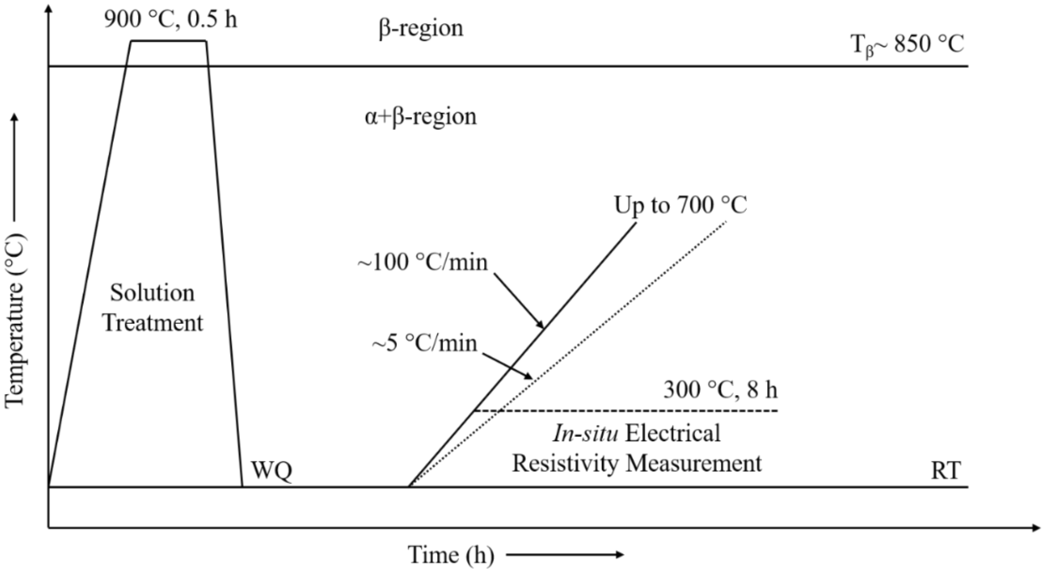

Fig. 4.2. Schematics of the heat treatment cycles used to identify the precipitation mechanisms occurring during different ageing approaches by determining the dependence of electrical resistivity on the ageing temperature and ageing time. WQ indicates water quenching.

4.3 Results

4.3.1 Microstructural Characterisation

The backscattered electron micrograph of as-received Ti-5553 β-Ti alloy, as shown in Fig. 4.3 (a), exhibits the presence of large globular and ellipsoidal α-phase precipitates along with some fine acicular α-phase precipitates. Following solution treatment, the microstructure consisted of equiaxed large β grains (Fig. 4.3 (b)) having an average grain size of 245 ± 75 µm (after measuring 100 grains). Following isothermal ageing at 300 °C for 8 h, there is no evidence of α-phase precipitates in the SEM micrograph as shown in Fig. 4.3 (c).

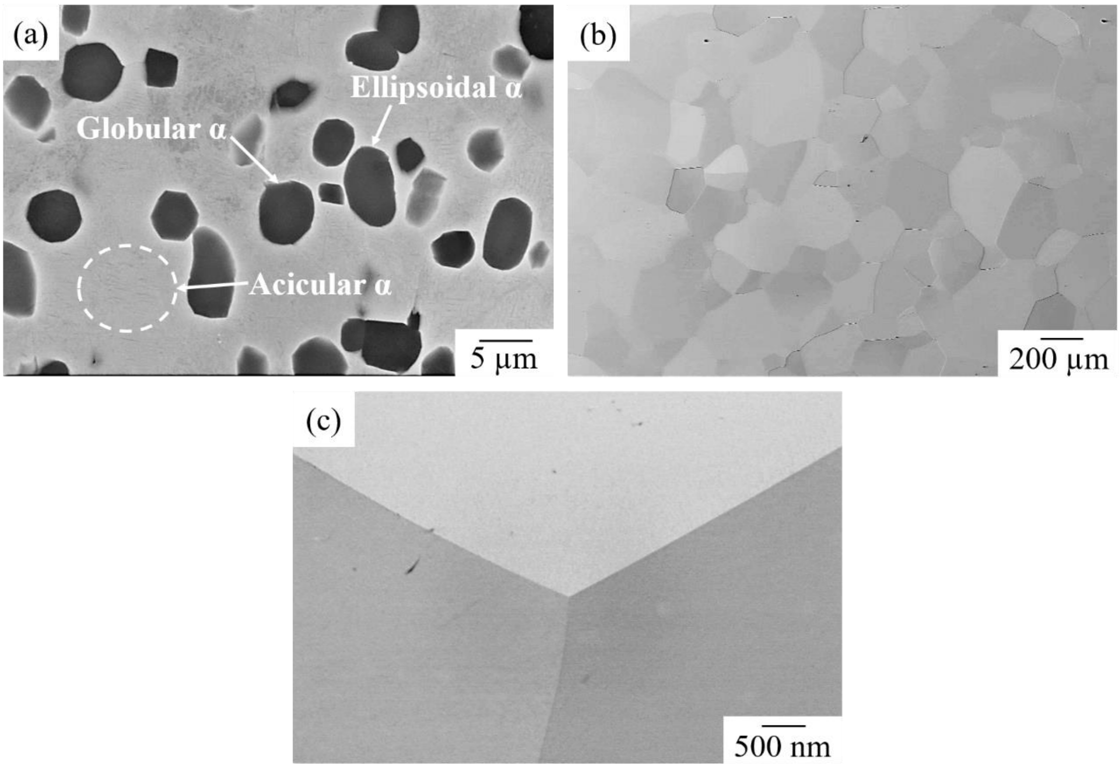

Fig. 4.3. The backscattered electron micrographs of the (a) as-received, (b) solution-treated and (c) the pre-aged (300 °C + 8 h) conditions of wrought Ti-5553 β-Ti alloy.

The BSE-SEM microstructures obtained after ageing at 500 °C, 600 °C and 700 °C following the heat treatment processes (Fig. 4.1) are shown in Fig. 4.4, Fig. 4.5 and

Fig. 4.6, respectively. Overall, single ageing with slow heating rate and duplex ageing produced a uniform microstructure for all ageing conditions, but in the case of single ageing with fast heating rate, a nonuniform microstructure was observed where larger size α-phase precipitates were observed near to the grain boundary. In addition, single ageing with slow heating rate and duplex ageing produced approximately the similar microstructure at all ageing conditions, but markedly different than single ageing with fast heating rate. The intragranular α-phase after single ageing with fast heating rate showed acicular morphology self-accommodated in triangular clusters, where precipitates tend to grow in different directions, meaning the α-phase possesses three variants. This is in line with the observations of Nag *et al.* [12], where the angular separation between the (0001) planes of α variants was reported to be 60° with each other. However, it is important to note here that the acicular α-phase precipitates obtained by single ageing with slow heating rate and duplex ageing do not show sharp ends as obtained for single ageing with fast heating rate. A thick and continuous grain boundary α-phase can also be seen for single ageing with fast heating rate whilst single ageing with slow heating rate and duplex ageing showed thin and continuous grain boundary α-phase. Further, single ageing with fast heating rate also led to the formation of Widmanstätten α-phase near to the grain boundaries. The microstructures obtained after single ageing with slow heating rate and duplex ageing also showed the presence of precipitate free zones (PFZ) near the grain boundaries. The width of the PFZ grew with the increase in ageing temperature.

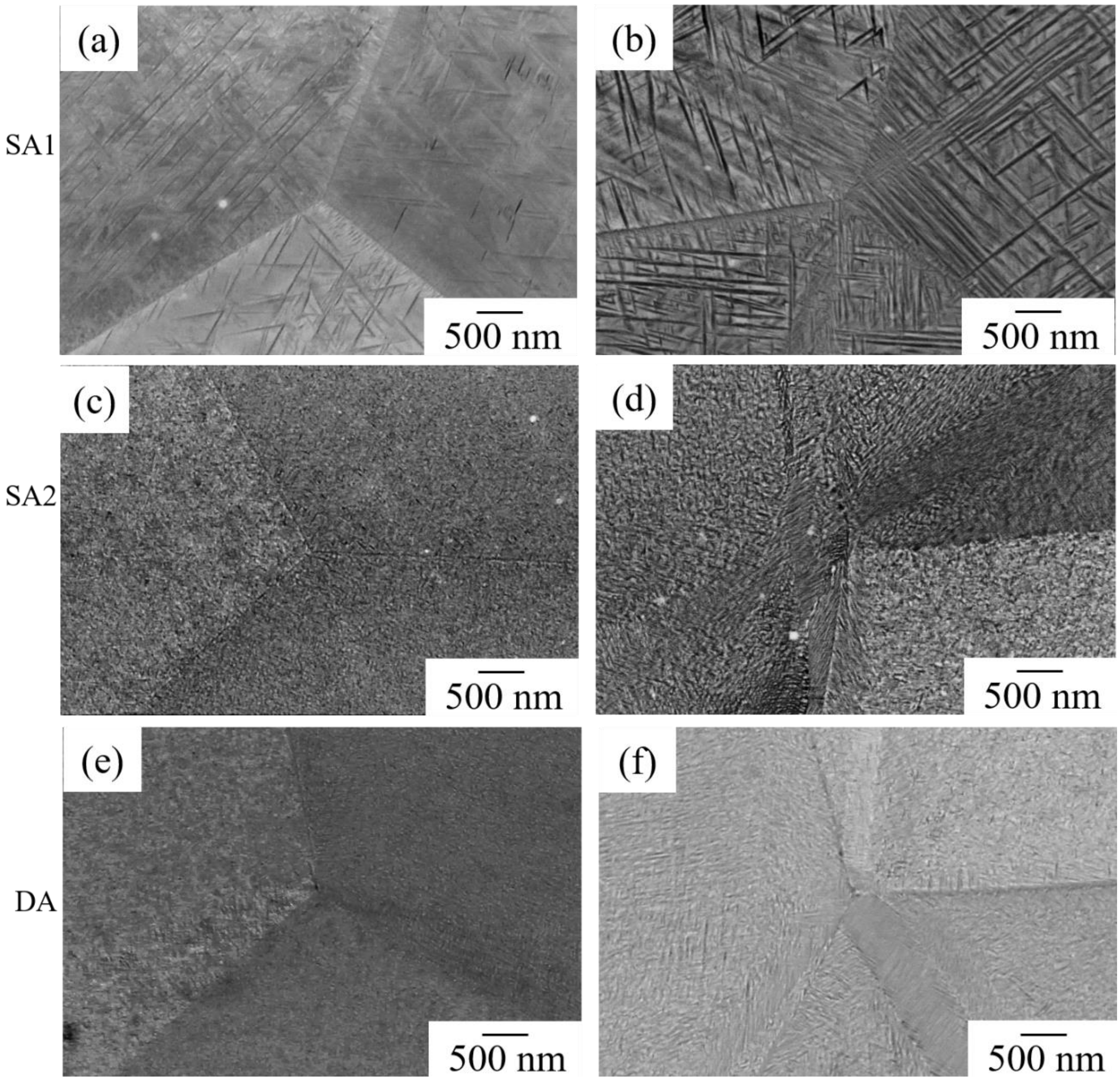

Fig. 4.4. BSE-SEM micrographs showing the grain boundary and intragranular α-phase precipitates for aged Ti-5553 β-Ti alloy at 500 °C for varied ageing time after following (a), (b) single ageing with fast heating rate (SA1), (c), (d) single ageing with slow heating rate (SA2), and (e) (f) duplex ageing (DA) approach.

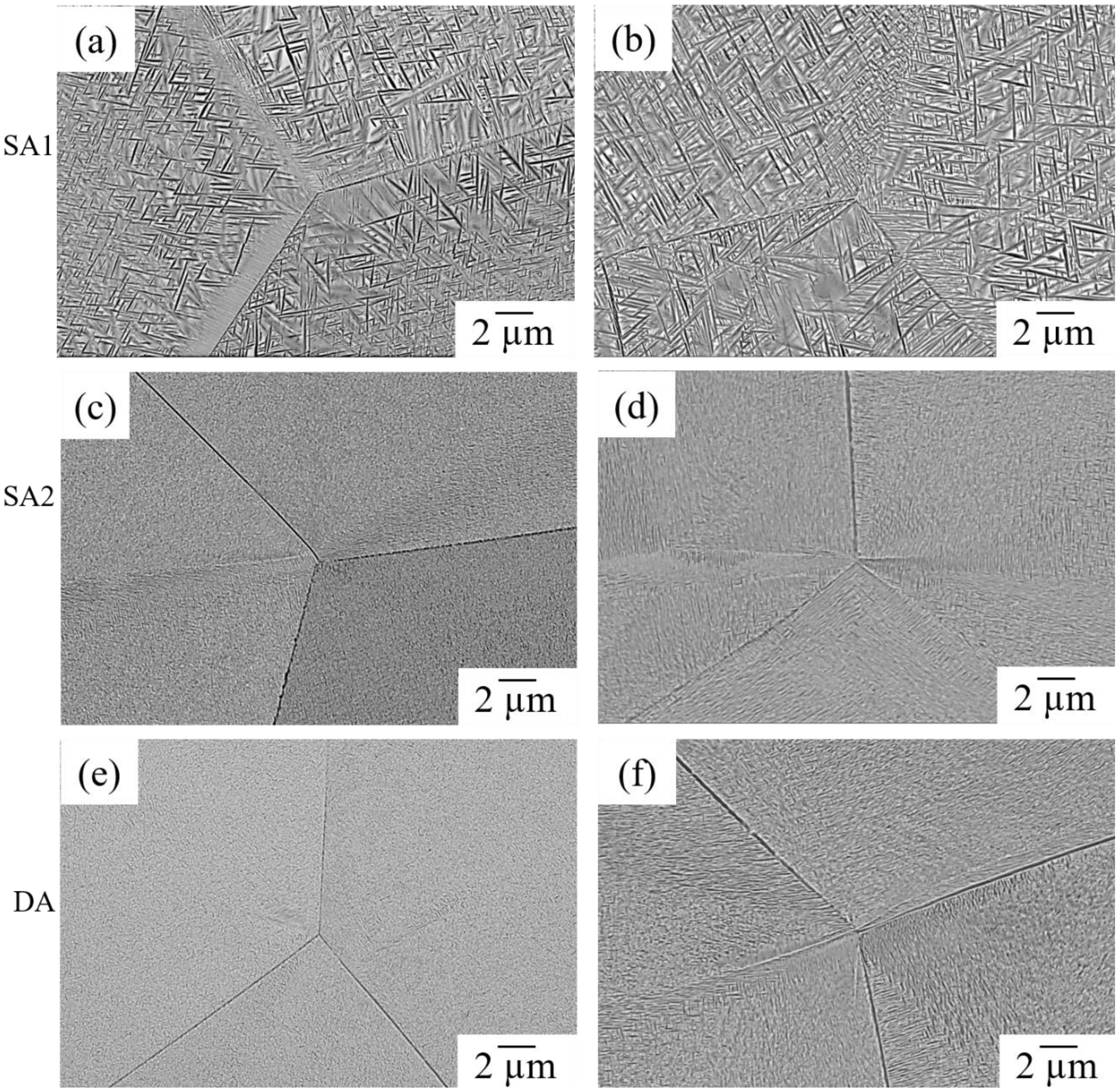

Fig. 4.5. BSE-SEM micrographs showing the grain boundary and intragranular α-phase precipitates for aged Ti-5553 β-Ti alloy at 600 °C for varied ageing time after following (a), (b) single ageing with fast heating rate (SA1), (c), (d) single ageing with slow heating rate (SA2), and (e) (f) duplex ageing (DA) approach.

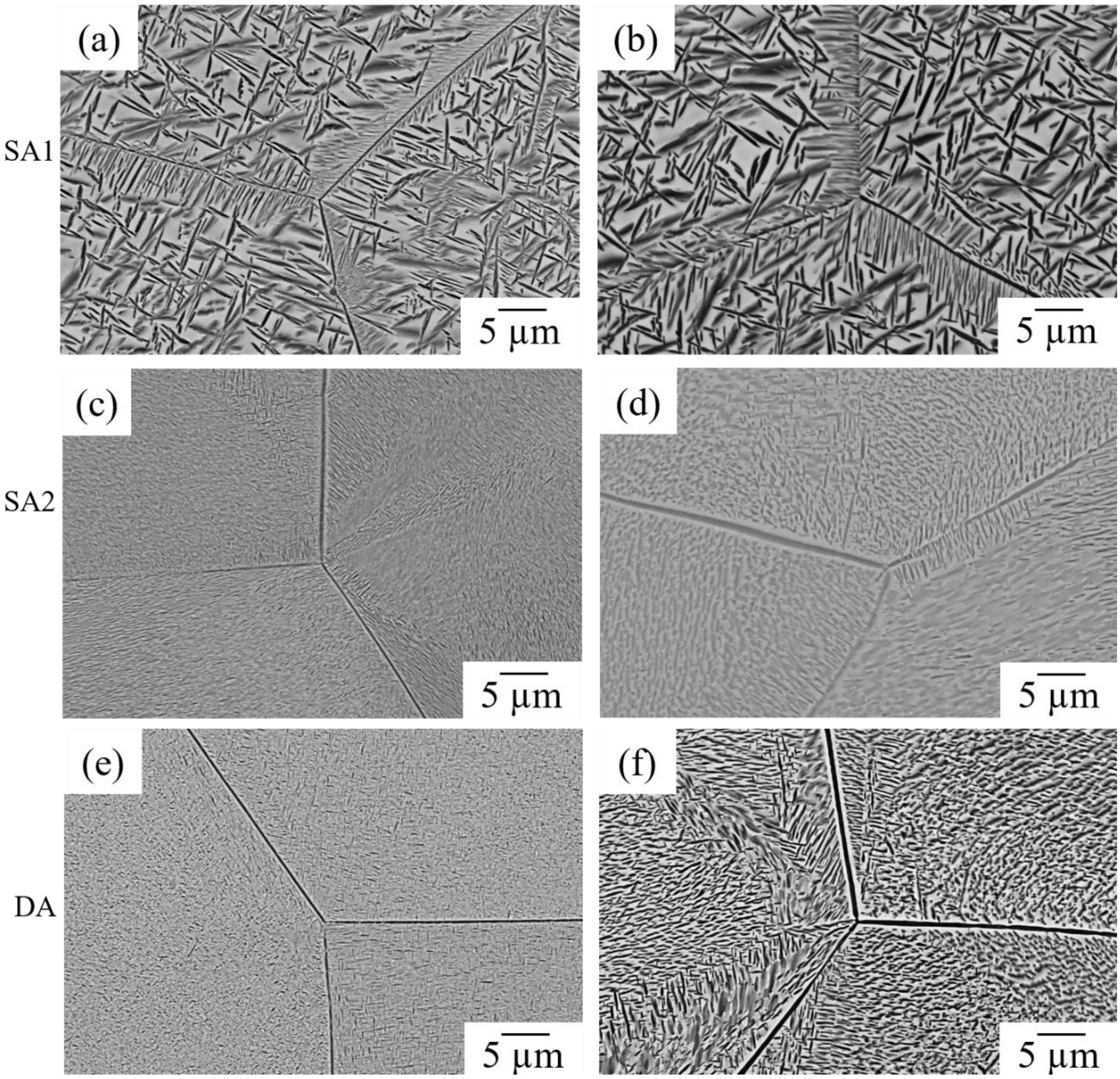

Fig. 4.6. BSE-SEM micrographs showing the grain boundary and intragranular α-phase precipitates for aged Ti-5553 β-Ti alloy at 700 °C for varied ageing time after following (a), (b) single ageing with fast heating rate (SA1), (c), (d) single ageing with slow heating rate (SA2), and (e) (f) duplex ageing (DA) approach.

The volume fraction, width and interparticle spacing of intragranular α-phase precipitates are presented in Fig. 4.7 (a), (b) and (c), respectively. The width of α-phase precipitates near grain boundaries in single ageing with fast heating rate varied in the range of ~30 nm to ~700 nm as ageing temperature increased from 500 °C to 700 °C. However, the intragranular α-phase precipitates for single ageing with fast heating rate are more-or-less uniformly distributed (Fig. 4.7).

The microstructures obtained after ageing at 500 °C exhibited much finer α-phase precipitates than α-phase precipitates observed in microstructures obtained after ageing at other higher temperatures (600 °C and 700 °C). This is shown in Fig. 4.7 (b). The width of α-phase precipitates remained approximately constant (Fig. 4.7 (b)) as ageing time was increased, but the volume fraction (Fig. 4.7 (a)) of α-phase increased indicating an increase in the number density. The interparticle spacing remained approximately the same throughout the ageing time at 500 °C, as shown in Fig. 4.7(c).

After ageing at 600 °C, the width of α-phase grew (Fig. 4.7 (b)) with increase in ageing time. However, the volume fraction of the α-phase remained approximately constant (Fig. 4.7 (a)) for all ageing treatments. It is important to note here that the volume fraction of intragranular α-phase precipitates is highest (~52%) at 600 °C (Fig. 4.7 (a)) for all kinds of ageing approaches. The single ageing with slow heating rate and duplex ageing showed much finer α-phase than single ageing with fast heating rate at the beginning (0.5 h) of the ageing at 600 °C, but the difference in the α-phase width was reduced after ageing for 6 h. The interparticle spacing between the α-phase precipitates increased with ageing time (Fig. 4.7 (c)).

The microstructures obtained after ageing at 700 °C exhibited the largest width for α-phase (Fig. 4.7 (b)) when compared to microstructures obtained at all other ageing temperatures. However, the volume fraction obtained at this temperature is the lowest and remained approximately constant during the ageing time (Fig. 4.7 (a)). This might be due to its proximity to the T_β (~850 °C). The width of intragranular α-phase precipitates grew for single ageing with slow heating rate and duplex ageing approach as the ageing time was increased, however, the width of intragranular α-phase remained approximately the same (Fig. 4.7 (b) for single ageing with fast heating rate approach even after ageing for 6 h. The microstructure obtained at the beginning (0.5 h) of single ageing with slow heating rate and duplex ageing showed the presence of finer α-phase precipitates when compared to single ageing with fast heating rate approach. However, the samples aged for 6 h exhibited approximately the same width for intragranular α-phase precipitates irrespective of the ageing approach. The interparticle spacing remained the highest at this temperature, and remained approximately the same for single ageing with fast heating rate, but increased for single ageing with slow heating rate and duplex ageing with ageing time.

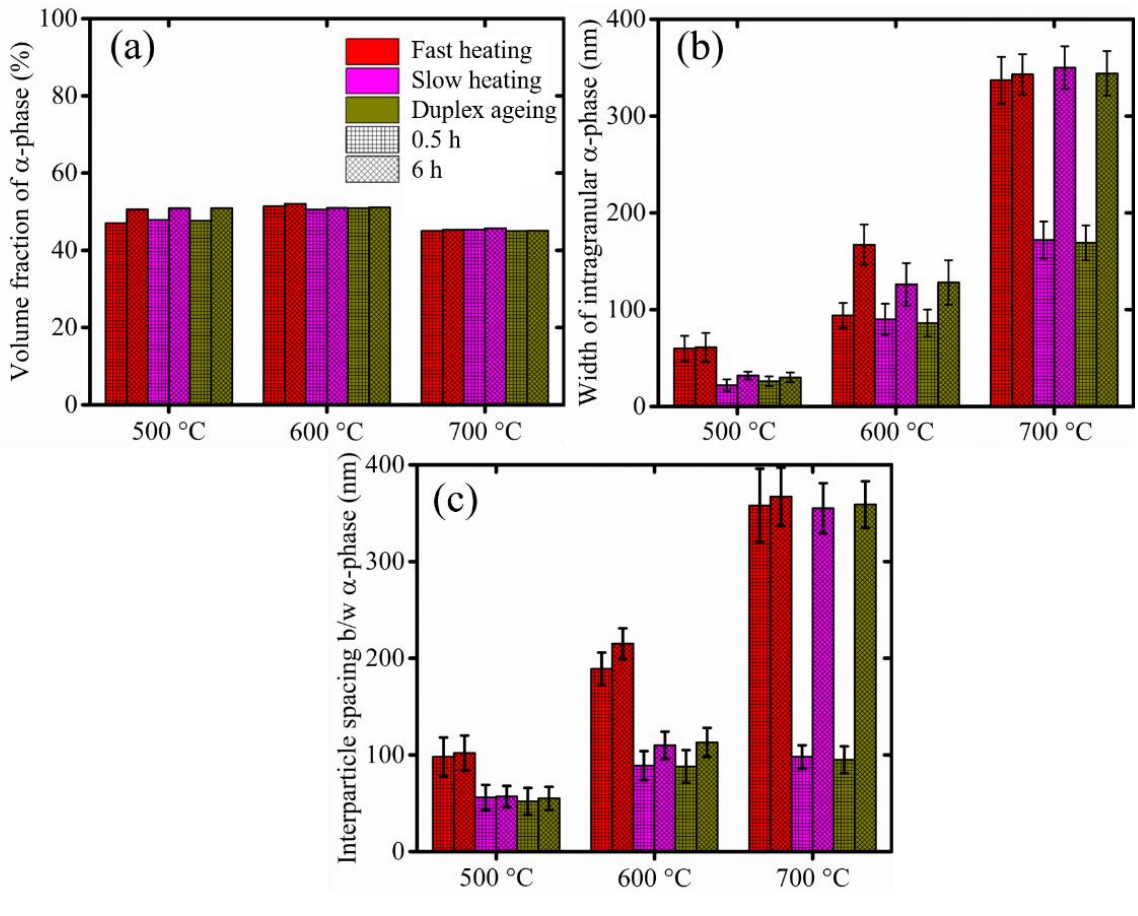

Fig. 4.7. The variation in the (a) volume fraction, (b) width and (c) interparticle spacing of intragranular α-phase precipitates for Ti-5553 β-Ti alloy aged via different ageing approaches at different temperatures and for different ageing time.

4.3.2 XRD Analysis

Fig. 4.8 shows the XRD pattern following solution treatment, pre-ageing (300 °C + 8 h) and single ageing (with fast heating rate) at different temperatures for 0.5 h. The peaks were identified and labelled following the peak indexing procedure described in section 3.3.5. The XRD pattern after solution treatment indicates the presence of solely β-phase matrix. The pre-aged sample (300 °C + 8 h) showed the presence of solely β-phase under SEM (Fig. 4.3 (c)), but a small volume fraction of isothermal ω-phase and α″ precipitates can be confirmed from the XRD diffraction patterns (Fig. 4.8). This is in line with earlier observations [57]. It is also important to note here that the diffraction patterns for solution-treated and pre-aged samples are significantly different. The pre-aged sample exhibits broader peaks than the solution-treated sample. This can be attributed to the coherency strains [95] present in the β-phase matrix due to the presence of coherent isothermal ω-phase [80]. The XRD patterns at higher temperature showed the presence of α-phase precipitates along with the β-phase matrix. This could also be seen from the SEM images (Fig. 4.4, Fig. 4.5 and Fig. 4.6).

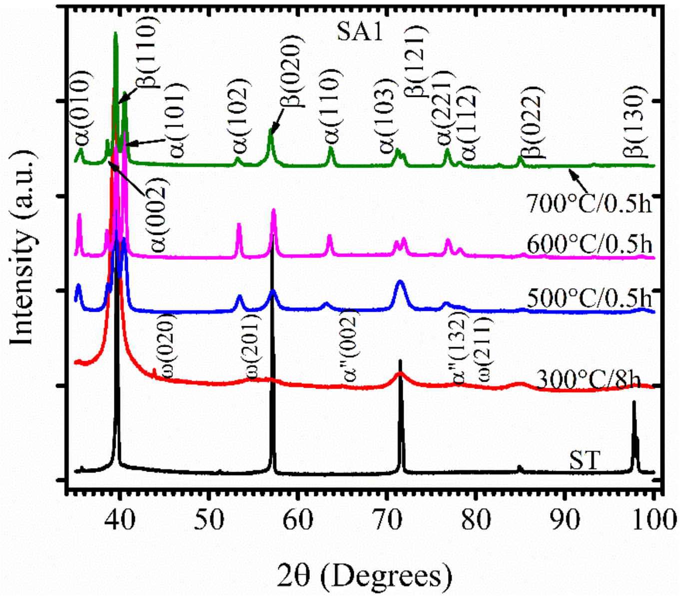

Fig. 4.8. The evolution of XRD diffraction pattern after solution treatment (ST), pre-ageing and ageing at different temperatures for 0.5 h after single ageing with fast heating rate (SA1).

4.3.3 Microhardness

Fig. 4.9 shows the changes in the microhardness values following the ageing at 500 °C, 600 °C and 700 °C for 0.5 h and 6 h using single ageing (with different heating rate) and duplex ageing heat treatment routes depicted in Fig. 4.1. For reference, the microhardness of as-received material was measured as 345 ± 7 Hv. The microhardness of the pre-aged sample (300 °C + 8 h) was measured as 474 ± 9 Hv and is not presented in Fig. 4.9. The hardness of the solution-treated sample is similar to Manda *et al.* [143], however, the pre-aged sample showed higher hardness compared to literature [57]. This additional increment in hardness could be due to the presence of α″ in the microstructure (see XRD Fig. 4.8) [144]. From the changes in the hardness in Fig. 4.9, the following points are noted.

1. The single ageing with slow heating rate and duplex ageing led to approximately similar microhardness at all ageing conditions.

2. The hardness of the aged samples in the α region (500 °C – 700 °C) decreased with increase in temperature.
3. After ageing at 500 °C, the microhardness increased from 0.5 h to 6 h of ageing. However, the microhardness obtained for single ageing with slow heating rate and duplex ageing was much higher than single ageing with fast heating rate, at all ageing times. The microhardness (~518 ± 8 Hv) of the sample aged at 500 °C for 0.5 h via duplex ageing is consistent with that of Coakley *et al.* [95] for a similar heat treatment profile (300 °C/0.5 h + 500 °C/2 h).
4. After ageing at 600 °C, the microhardness showed a decreasing trend as ageing time was increased. Single ageing with slow heating rate and duplex ageing showed higher microhardness than single ageing with fast heating rate, at all ageing times. However, the difference in the microhardness of single ageing with slow heating rate and duplex ageing with respect to single ageing with fast heating rate decreased with ageing time.
5. The samples aged at 700 °C exhibited the lowest microhardness compared to all other ageing temperatures. For single ageing with slow heating rate and duplex ageing, the microhardness decreased as ageing time was increased, however, the microhardness for single ageing with fast heating rate showed very small variation with an increase in ageing time. However, the samples aged via single ageing with slow heating rate and duplex ageing showed higher microhardness at the beginning of the ageing time (0.5 h) with respect to single ageing with fast heating rate. The samples aged for 6 h showed approximately the same microhardness irrespective of the ageing approach.

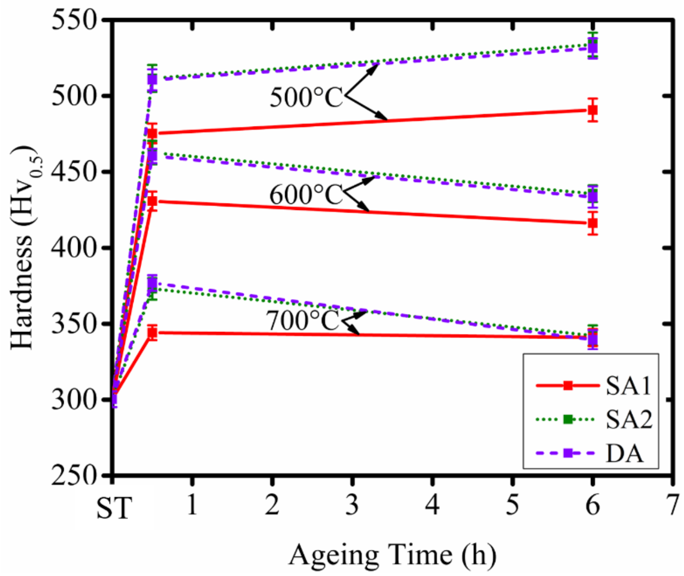

Fig. 4.9. The microhardness characteristics of Ti-5553 β-Ti alloy heat treated via different ageing approaches at different temperatures and for different ageing time. SA1 represents single ageing with fast heating rate, SA2 represents single ageing with slow heating rate, and DA represents duplex ageing approach. WQ indicates water quenching.

4.3.4 Electrical Resistivity Measurement

The change in electrical resistivity as a function of temperature during single ageing with different heating rates is shown in Fig. 4.10 (a). The electrical resistivity is normalised with respect to the room temperature electrical resistivity. It is clear from the figure that the initial change in the electrical resistivity remained the same between two processes. This confirms consistency in microstructures among different solution-treated samples.

During single ageing with fast heating rate, the electrical resistivity first dropped as the temperature was raised. The drop was observed up to ~550 °C. Following this, the electrical resistivity increased indicating a phase transformation at higher temperature. For single ageing with slow heating rate, there was a similar drop in the electrical resistivity up to ~320 °C and then the electrical resistivity increased between

~320 °C and ~500 °C. The electrical resistivity dropped again up to ~600 °C and then increased again indicating a lot of phase transformations during single ageing with slow heating rate.

Fig. 4.10 (b) shows the change in the electrical resistivity up to the pre-ageing step (300 °C + 8 h) of duplex ageing. The electrical resistivity dropped as the temperature was increased. The resistivity then increased further before becoming approximately saturated after ~5 h of ageing.

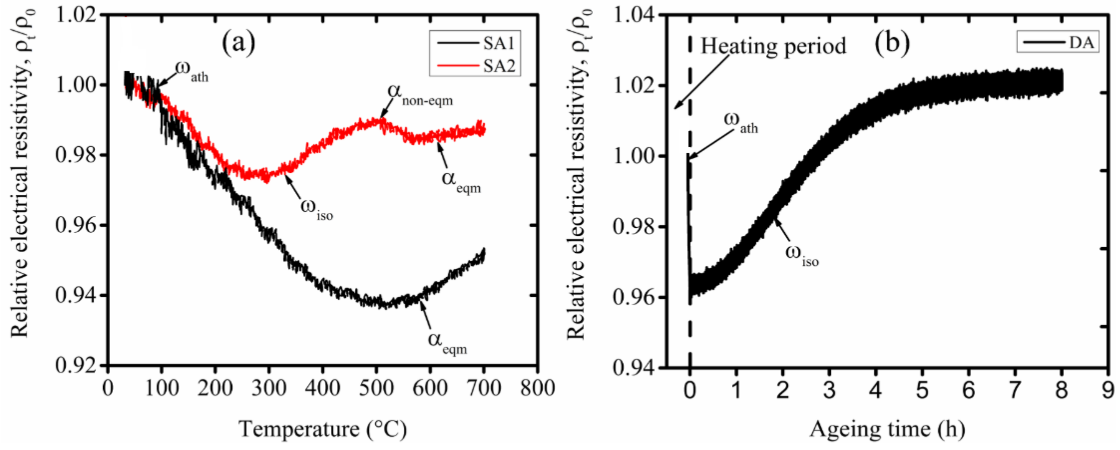

Fig. 4.10. The relative electrical resistivity plots obtained from the solution-treated Ti-5553 β-Ti alloy during the heating period up to 700 °C for (a) single ageing with fast heating rate (SA1) and (b) single ageing with slow heating rate (SA2). (c) shows the relative electrical resistivity plot for pre-ageing-step (300 °C + 8 h) in duplex ageing (DA) measured during heating period up to 300 °C and during ageing at 300 °C up to 8h.

4.4 Discussion

4.4.1 Precipitation Kinetics

The microhardness measurements revealed similar variation in mechanical properties during single ageing with slow heating rate and duplex ageing approaches, however, significantly different than the single ageing with fast heating rate approach. This indicates that single ageing with slow heating rate and duplex ageing approaches follow similar precipitation behaviour, but different than the single ageing with fast heating rate approach. Hence, the precipitation behaviour during different ageing approaches has been understood via *in situ* measured electrical resistivity results (Fig. 4.10).

Irrespective of the ageing approach, the initial drop in the electrical resistivity could be attributed to the partial dissolution of athermal ω-phase formed during rapid cooling, which disappears reversibly on heating [12,94,101]. In the case of single ageing with slow heating rate, the increase in electrical resistivity after ~320 °C can be attributed to the formation of isothermal ω-phase [94]. The decrease in the electrical resistivity at ~500 °C is an indication of the formation of isothermal ω-phase-assisted α-phase precipitates. The electrical resistivity decreases due to the progressive vanishing of isothermal ω-phase [17,94]. The α-phase precipitates formed via isothermal ω-phase-assisted α-phase precipitation are reported to have non-equilibrium ($\alpha_{non\text{-}eqm}$) nature just after the precipitation and tend to attain equilibrium (α_{eqm}) after further ageing [111]. Therefore, this decrease in the electrical resistivity can be associated with the formation of non-equilibrium α-phase precipitates from isothermal ω-phase. The increase in the electrical resistivity at ~600 °C can be related to the formation of equilibrium α-phase as reported in the literature [101,111]. The important point to note here is that Zheng *et al.* [111], through their *ex situ* TEM study, reported that the $\alpha_{non\text{-}eqm}$ dissolves in the matrix at higher temperatures and then re-precipitates as α_{eqm}. Through these observations, they concluded that the ω_{iso} precipitates have an indirect role in the refinement of the α-phase precipitates at higher temperatures. However, there are no such indications for the dissolution of the $\alpha_{non\text{-}eqm}$ in the current *in situ* electrical resistivity study. The current study suggests that there is a direct role of ω_{iso} precipitates in the refinement of the α-phase precipitates.

At the pre-ageing-step, the increase in the electrical resistivity can be associated with the nucleation of isothermal ω-phase. It could be seen from Fig. 4.10 that it took around 0.25 h ageing time to see the start of formation of isothermal ω-phase, which is in line with the literature [145]. The resistivity becomes constant after ~5 h of ageing indicating the saturation for the formation of isothermal ω-phase. This also validates that no α-phase has formed at the pre-ageing-step as observed using XRD (Fig. 4.8) and SEM (Fig. 4.3 (c)). Hence, the α-phase observed in the microstructure at higher temperatures after duplex ageing is formed due to isothermal ω-phase-assisted α-phase precipitation. Therefore, single ageing with slow heating rate and duplex ageing show similar microstructural characteristics as their precipitation behaviour is the same.

For single ageing with fast heating rate, the increase in the electrical resistivity observed at ~550 °C is an indication of the nucleation of equilibrium α-phase due to the pseudo-spinodal mechanism as reported earlier [26]. No formation of isothermal ω-phase (ω_{iso}) can be seen during single ageing with fast heating rate. This means that the precipitation mechanism for single ageing with fast heating rate is markedly different, and therefore, a difference in the microstructure and microhardness was seen in comparison to single ageing with slow heating rate and duplex ageing.

4.4.2 Evolution of Intragranular α-phase Precipitates

The width of intragranular α-phase and interparticle spacing increased as a function of ageing temperature. The observance of coarser intragranular α-phase at higher temperature can be attributed to faster diffusion kinetics at higher temperature

[146]. The precipitation of coarser α-phase leads to a region with more β-stabilisers in the surrounding region of the precipitates. The precipitation of α-phase is difficult in this region because of high stability of the region due to enrichment in β-stabilisers. Hence, it gives broader β stabilised regions surrounding the precipitates, leading to higher interparticle spacing. The refined α-phase for single ageing with slow heating rate and duplex ageing is due to the isothermal ω-phase-assisted α-phase nucleation, as seen from electrical resistivity results (Fig. 4.10).

At 500 °C, the width of intragranular α-phase and interparticle spacing remained almost the same with increased ageing time, irrespective of the ageing approach. This could be because the α-phase starts precipitating at around this temperature, as seen from electrical resistivity results (Fig. 4.10). This indicates that the α-phase precipitation did not reach the equilibrium condition before it starts coarsening. This could also be understood from the fact that volume fraction increases and the width of intragranular α-phase and interparticle spacing remained approximately the same.

At 600 °C, the volume fraction remained the same for both the ageing times, but the width of the intragranular α-phase and interparticle spacing increased, irrespective of the ageing approach. This indicates that the α-phase precipitation reached the equilibrium condition at this temperature.

4.4.3 Effect of Intragranular α-phase Precipitates on Microhardness

The effect of interparticle spacing upon the eventual mechanical properties in Ti–6Mo–5V–3Al–2Fe β-Ti alloy has been considered previously [146]. This suggests that the reduction in interparticle spacing observed here on its own would lead to an increase in hardness of the samples after ageing. This reduction in the interparticle spacing can also be correlated with the refinement of the α-phase width during ageing leading to higher microhardness, as stated above. In addition, refinement of α-phase width can directly be linked to the increase in yield strength and hardness [10,136]. We conclude therefore that the increase in hardness after single ageing with slow heating rate and duplex ageing is solely due to the refinement of the α-phase. A similar proportional increase would be expected in the yield and fatigue strength of the material [147,148].

At 500 °C, the microhardness increased as a function of ageing time for all the ageing approaches. This is due to the increased number density (Fig. 4.7) of the precipitates leading to reduced interparticle spacing. The single ageing with fast heating rate approach showed reduced microhardness due to coarser α-phase in comparison to single ageing with slow heating rate and duplex ageing approach.

At 600 °C, the microhardness showed a decreasing trend (Fig. 4.9) as a function of ageing time. This happened due to the coarsening of the α-phase (Fig. 4.7). The single ageing with slow heating rate and duplex ageing approach showed higher hardness than single ageing with fast heating rate due to the finer microstructure.

At 700 °C, the microhardness remained the same for both the ageing times during the single ageing with fast heating rate approach. This is due to the similar size and volume fraction of α-phase at both the ageing times (Fig. 4.7). The single ageing with slow heating rate and duplex ageing showed higher hardness at the beginning because of the refined microstructure, but the size of the α-phase after single ageing with slow heating rate and duplex ageing became the same as single ageing with fast heating rate after ageing for 6 h leading to the same hardness at this ageing condition.

4.4.4 Correlation between Microstructure and Microhardness

A correlation between the microhardness values and the width of α-phase (d) was established for all the aged samples. A high value of correlation coefficient, $R^2 = 0.95$ was observed for the fitted regression lines. The mean width of α-phase was considered as the best microstructural feature to control the microhardness values. The dependence of microhardness and the width of α-phase is represented in Fig. 4.11 and the relation is given in Equation 4.1.

$$H_v = 348 + 247/\sqrt{d} \tag{4.1}$$

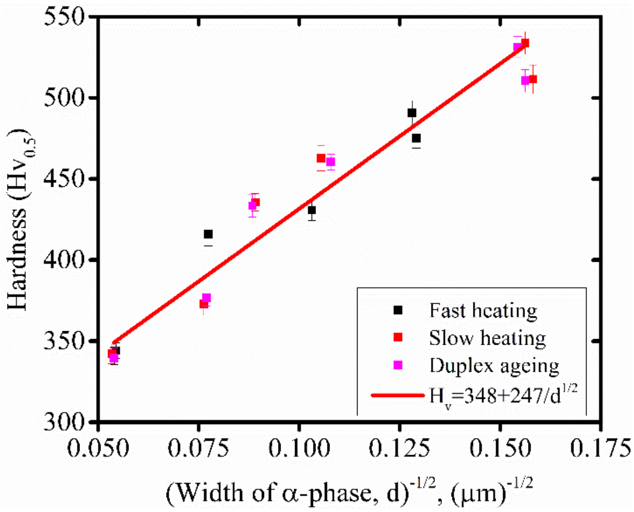

Fig. 4.11. Variation of mean hardness with inverse of square root of mean width of α-phase after ageing the AM Ti-5553 β-Ti alloy samples.

4.5 Conclusions

A study was carried out to understand the influence of different ageing approaches on microstructure evolution and the associated effect on hardness in Ti-5553 β-Ti alloy. The following conclusions can be made:

1. Duplex ageing and single ageing with slow heating rate yield similar microhardness and microstructure results at all ageing conditions. This can be attributed to the same precipitation mechanism in both cases, as observed via *in situ* electrical resistivity measurement.
2. Single ageing with slow heating rate and duplex ageing yield uniform microstructures in comparison to ageing with fast heating rate.
3. The study supports previous reports that the isothermal ω-phase plays a direct role in the nucleation of refined α-phase precipitates, warranting detailed investigation into the precipitation kinetics of isothermal ω-phase to better control the mechanical properties of the material.
4. Single ageing with slow heating rate and duplex ageing generally produce higher microhardness in comparison to single ageing with fast heating rate, however, the difference in the microhardness after single ageing with slow heating rate and duplex ageing with respect to single ageing with fast heating rate tends to decrease with ageing time at higher temperatures (600 °C and 700 °C).
5. A correlation ($H_v = 348 + 247/\sqrt{d}$) between the microhardness values and the width of α-phase (d) was estabilished for all the aged samples.

The results in this chapter demonstrated that isothermal ω-phase plays a direct role in the refinement of α-phase precipitates leading to higher microhardness. Thus, it leads to the following chapter to understand the precipitation kinetics of isothermal ω-phase that will help in utilising the advantages of isothermal ω-phase α-phase nucleation to better control the alloy properties.

CHAPTER 5

PRECIPITATION KINETICS OF NANOSCALE ISOTHERMAL ω-PHASE IN β-Ti ALLOY AS A FUNCTION OF DIFFERENT COOLING RATES

5.1 Introduction

The duplex-aged samples and the single aged samples with slow heating rate in the previous chapter exhibited higher hardness for the wrought Ti-5553 β-Ti alloy compared to the single-aged samples with fast heating rate. This happened due to the isothermal ω-phase-assisted nucleation process leading to a highly refined α-phase distribution, which has previously shown improved alloy strength [8,40,116]. Hence, it is important to understand the kinetics of isothermal ω-phase formation in order to precisely control and optimise the alloy properties.

For this chapter, samples of a Ti-5553 β-Ti alloy produced using air cooling and water quenching after solution treatment were used to establish the influence of the cooling rate on the kinetics of nanoscale isothermal ω-phase precipitates. *In situ* SANS measurements (section 5.3.2) were used to quantify the evolved microstructure and understand the nucleation and growth kinetics of isothermal ω-phase precipitates during low-temperature (300 °C) ageing. Complementary *in situ* electrical resistivity measurements (section 5.3.3) conducted during ageing at 300 °C and 325 °C provided additional insight into the precipitate mechanism and activation energy. These *in situ* measurements were supported by conventional SEM and XRD measurements to confirm the phases present. With this combined approach, the kinetics of isothermal ω-phase precipitates transformation from the β-phase matrix under different cooling rates are clarified. Finally, Vickers microhardness measurements (section 5.3.4) were used to see the likely effect of the evolved microstructure on the mechanical properties.

5.2 Experimental Details

The schematics of the entire experiments are shown in Fig. 5.1. *In situ* SANS and electrical resistivity measurements were recorded at room temperature, during the heating period, and during the entire ageing process. Room temperature data were collected first, and then sample temperature was raised to the ageing temperature (300 °C or 325 °C) with a heating rate of ~100 °C/min, and was held for 8 h whilst the measurements were recorded. The detailed description of SANS and electrical resistivity measurements can be seen in sections 3.3.8 and 3.3.9, respectively.

For SANS data analysis, the complete 60 min of room temperature data was averaged, but for ageing, the data were combined into 15-minute bins with the exception of 100 s of data averaged just after the sample reached the ageing temperature to show the data at the end of the heating period. An ellipsoid model fitting was applied to deconvolute the evolved microstructure. This model was chosen based on the understanding of precipitate shape from the literature [17,95].

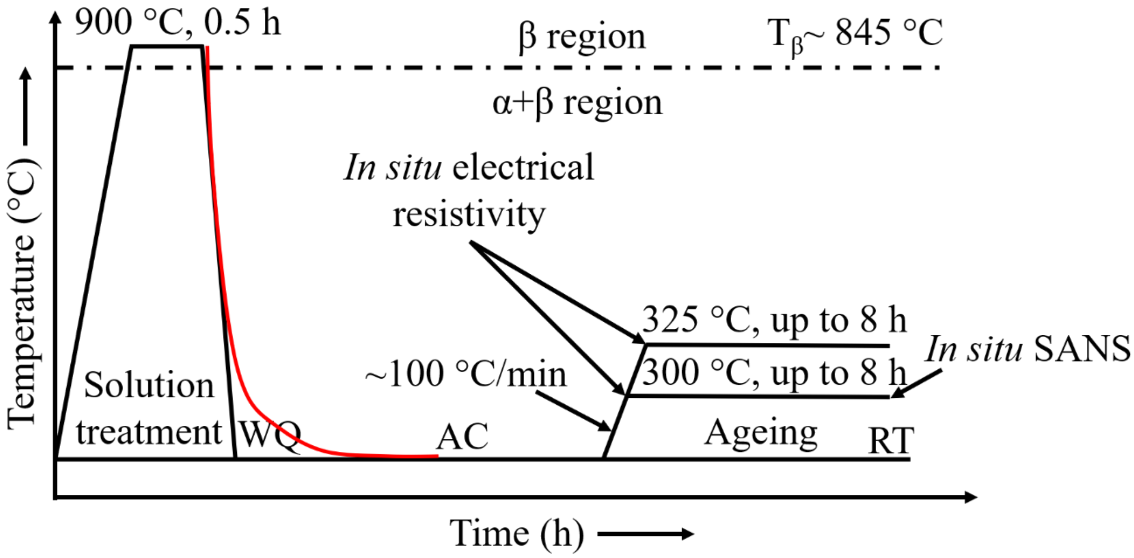

Fig. 5.1. The schematics of heat treatment cycle used in this work to understand the nucleation and growth kinetics of nanoscale isothermal ω-phase precipitates in Ti-5553 β-Ti alloy as a function of water quenching (WQ) and air cooling (AC) during solution treatment.

The solution-treated samples after water quenching and air cooling were also subsequently aged at 300 °C for a sequence of times (1 h, 2 h, 4 h and 8 h). The ageing was performed in a pre-heated tube furnace under argon gas with a heating rate of ~100 °C/min. Samples were water-quenched after ageing.

5.3 Results

5.3.1 Microstructural Characterisation

The BSE-SEM micrographs of samples after water quenching and air cooling exhibited a homogenised microstructure (Fig. 5.2 (a) and (b), respectively), where the XRD analysis (Fig. 5.3 (a)) indicated the presence of solely β-phase in the microstructure. The average β grain size for water-quenched and air-cooled samples was measured as 245 ± 75 µm and 225 ± 85 µm, respectively. Note that the presence of an inevitable ω_{ath} (without the size or volume fraction difference) has been reported consistently for the air-cooled and the water-quenched Ti-5553 β-Ti alloy after solution treatment when examined under TEM [8,143,149]. Since the present solution treatment conditions are same as the previous work on the same alloy, it is reasonable to assume the formation of ω_{ath} (undetected by SEM and XRD) in both samples after solution treatment. The average microhardness values were measured as 300 ± 5 Hv and 298 ± 4 Hv for water-quenched and air-cooled samples, respectively. The BSE-SEM micrographs (Fig. 5.2 (c) and (d)) for the samples aged at 300 °C for 8 h after solution treatment (both water-quenched and air-cooled) also showed homogenised microstructure. However, the presence of a small volume fraction of isothermal ω-phase precipitates and α″-phase, in the β-phase matrix, can be inferred in the aged condition from the XRD patterns (Fig. 5.3 (b)). This is in agreement with the TEM and XRD observations in the literature [57,120] for Ti-5553 β-Ti alloy during ageing.

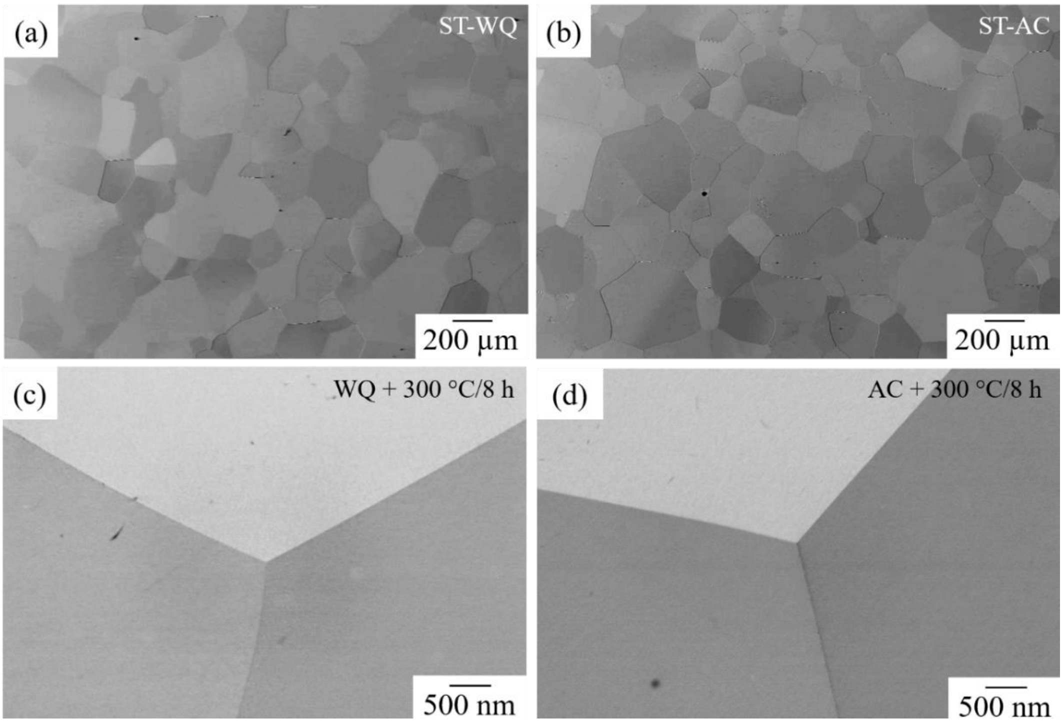

Fig. 5.2. The BSE-SEM microstructure of Ti-5553 β-Ti alloy samples after solution treatment (ST) under (a) water quenching (WQ) and (b) air cooling (AC), (c) and (d) show the BSE-SEM microstructure of aged samples (300 °C for 8 h) after WQ and AC, respectively.

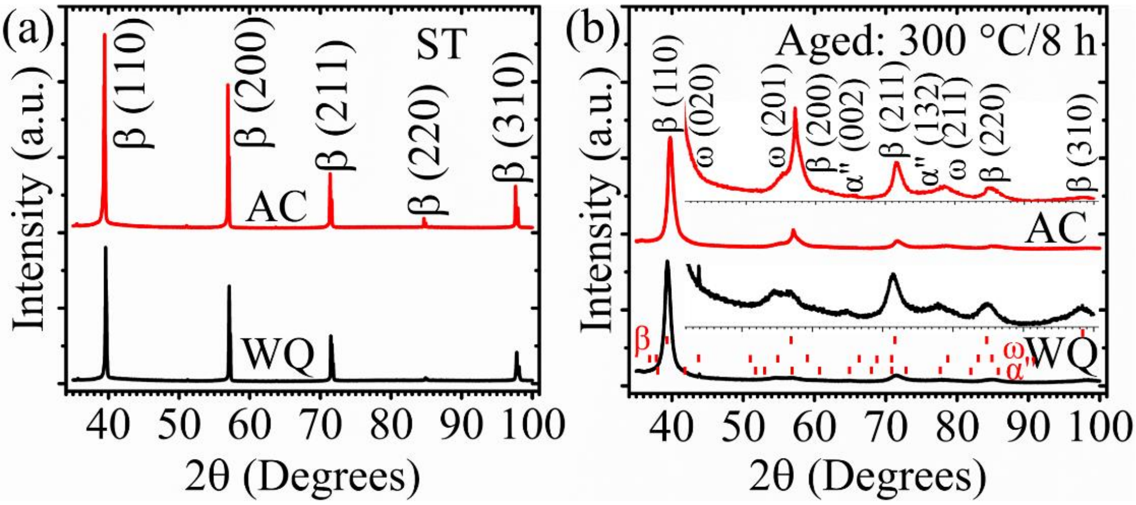

Fig. 5.3. The XRD diffraction patterns of Ti-5553 β-Ti alloy samples after (a) solution treatment (ST) using water quenching (WQ) and air cooling (AC). The XRD patterns show the presence of solely β-phase. The doublets seen in the XRD data are due to the diffraction from both $K_{\alpha1}$ and $K_{\alpha2}$ emissions. (b) shows the XRD diffraction patterns after subsequent ageing the solution-treated samples at 300 °C for 8 h, indicating the presence of β-phase and small volume fraction of isothermal ω-phase and α″-phase.

5.3.2 Small-angle Neutron Scattering

One-dimensional *I vs q* plots for all the SANS measurements after water quenching and air cooling are shown in Fig. 5.4 (a) and (b), respectively. The error bars (~±0.01 cm^{-1}) for each point are not presented in the plots (Fig. 5.4) to assist in delineating the data. The scattering curves after water quenching and air cooling are significantly different in terms of shape and evolution rate. The scattering curve for the air-cooled sample evolves quite slowly when compared to the water-quenched sample.

The scattering intensity decreased with respect to room temperature scattering when the sample temperature was increased to the ageing temperature (300 °C). This occurred for both cooling rates. During the ageing period, the first additional scattering or deviation from the room temperature scattering was observed after 0.25 h and 1.25 h for water-quenched (at ~0.05 $Å^{-1}$) and air-cooled (at ~0.08 $Å^{-1}$) samples, respectively; for the water-quenched sample the deviation was in agreement with similar SANS measurements obtained by Coakley *et al*. [95]. This additional scattering can be associated with the nucleation of isothermal ω-phase precipitates [57]. The α″ does not affect the SANS signal as observed previously [87] because it is formed by a diffusionless process [120], creating no contrast difference between the precipitate and the matrix. The ageing temperature (300 °C) is lower than the minimum stress relief temperature (480 °C), therefore, the presence of residual stresses caused by rapid cooling after solution treatment can be expected in the samples. However, the small dimensions of the samples that were extracted for the SANS means that there will have been considerable relaxation of any residual stress. Furthermore, SANS does not look at lattice-scale deformations, but structures at higher-order length scales [138].

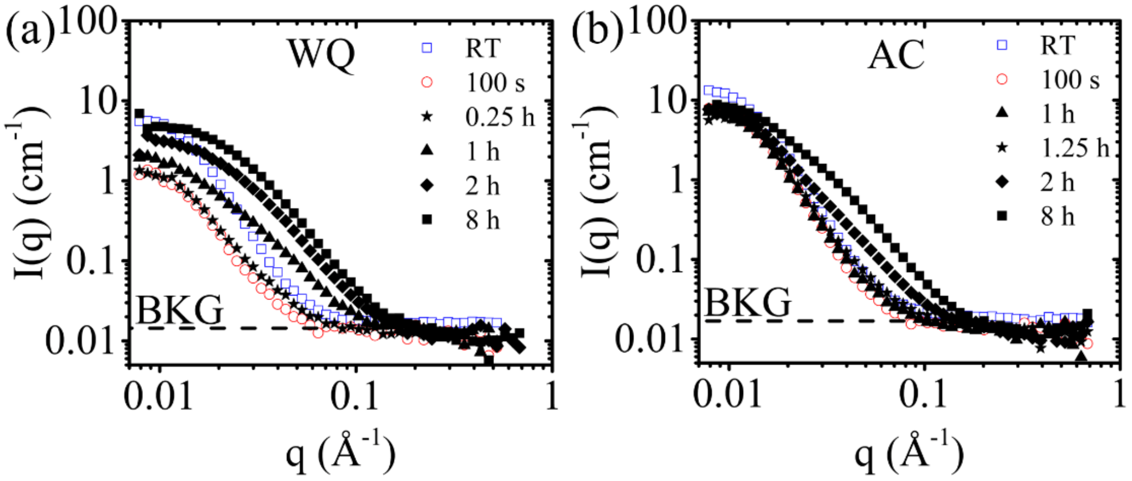

Fig. 5.4. The one-dimensional intensity (*I*) vs momentum transfer (*q*) plots of SANS scattering for Ti-5553 β-Ti alloy samples measured at room temperature (RT), after heating period (100 s) and *in situ* at 300 °C up to 8 h after (a) water quenching (WQ) and (b) air cooling (AC). The mentioned time represent the end of the measurement. BKG refers to the background scattering.

5.3.3 Electrical Resistivity Measurement

The electrical resistivity measurements for water-quenched and air-cooled samples were recorded during the entire ageing process, heating from room temperature to both 300 °C and 325 °C for up to 8 h. Relative electrical resistivity results are plotted

(Fig. 5.5) to understand the change in the kinetics of isothermal ω-phase precipitates as a function of cooling rate from solution treatment temperature (*i.e.* water quenching or by air cooling). The solution-treated condition is considered as the reference state in order to calculate the relative electrical resistivity change.

Both air-cooled and water-quenched samples show a similar drop in the electrical resistivity as the temperature was raised to the ageing temperatures (300 °C and 325 °C), as shown in Fig. 5.5 (a) and (b). This decrease in the electrical resistivity can be associated with the partial dissolution of athermal ω-phase [80,141,150–153].

The evolution of the electrical resistivity during ageing at 300 °C correlates with the kinetics for isothermal ω-phase formation determined by SANS analysis. The first increase in the electrical resistivity (discarding the initial drop during the heating period) can be associated with the time to nucleate isothermal ω-phase precipitates [101]. This occurs for the water-quenched sample (Fig. 5.5 (c)) after ~0.25 h of ageing, which is consistent with the changes in SANS data that showed a marked increase in scattering between 0.25 and 1 h. In comparison, for the air-cooled sample the initial increase in electrical resistivity was delayed relative to the water-quenched sample to ~1.25 h. These delayed kinetics are also observed in the scattering intensity derived from the SANS data. The formation of α″-phase in Ti-5553 β-Ti alloy happens rapidly after ~2 h of ageing at 325 °C [120]. We did not observe any clear deviation in the electrical resistivity curves (Fig. 5.5) due to the formation of α″-phase. This is in line with the previous observations [54,94,154], where electrical resistivity measurements were used to examine the precipitation sequences during continuous heating of β-Ti alloys to higher temperatures. The observations from the literature suggest that there was no clear deviation when α″-phase transformation happened. We contend therefore that the possible presence of α″-phase does not affect the electrical resistivity data. The electrical resistivity measurements basically show the interaction with the interfacial energy produced by the growing surface of the precipitates, and will not generate any changes as an effect of the lattice distortions. Hence, it is stated that the expected presence of residual stresses will not affect the measurements in the current work. The similarity in the intital results of electrical resistivity measurements for the water-quenched and the air-cooled samples also indicate that either there were no residual stresses in the samples due to relaxation during cutting of the samples or the electrical resistivity does not interact with the residual stresses produced, because the difference in the residual stress values for different cooling rate is expected.

After this initial increase in electrical resistivity during ageing at 300 °C, the electrical resistivity increased further (Fig. 5.5) and attained an approximate saturation condition after ~5 h and ~6 h of ageing the water-quenched and air-cooled samples, respectively.

For the samples aged at 325 °C, a reduction in the precipitate nucleation time was observed. The first increase in electrical resistivity for water-quenched sample was observed almost immediately upon reaching the ageing temperature; however, the nucleation time was considerably delayed (~1 h) for the air-cooled sample. As for the samples measured at 300 °C the electrical resistivity increased further (Fig. 5.5 (d)) and attained an approximate saturation condition after ~3 h and ~5 h of ageing the water-quenched and air-cooled samples, respectively.

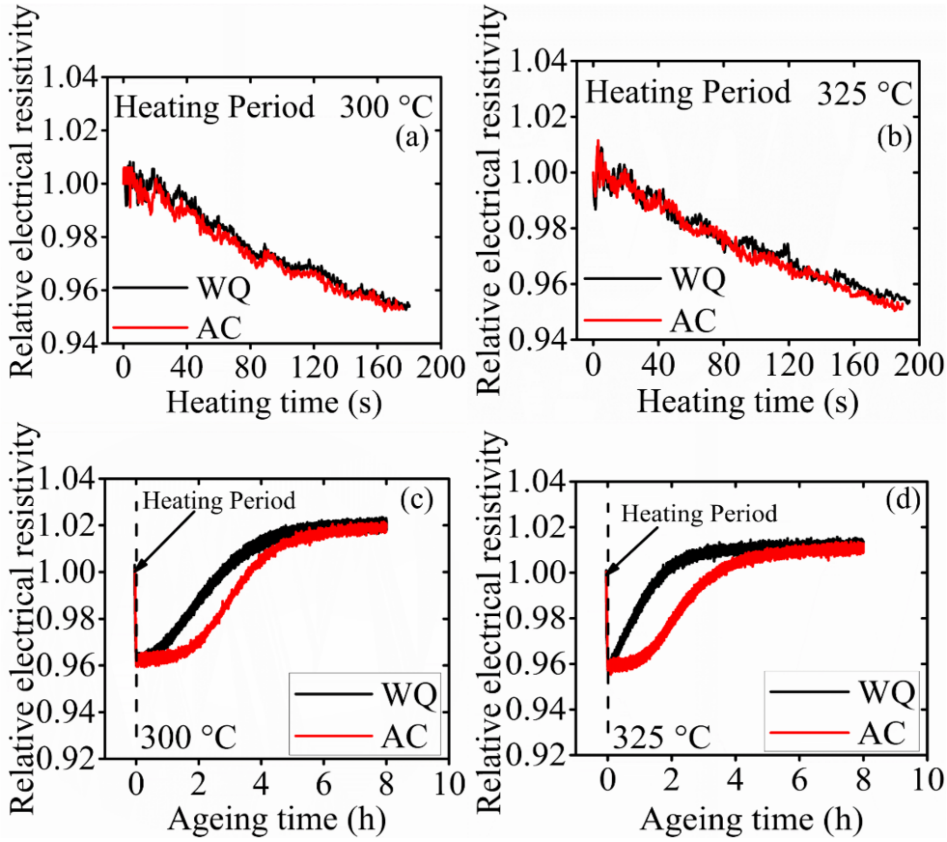

Fig. 5.5. The evolution of electrical resistivity measurements for Ti-5553 β-Ti alloy recorded in-situ at room temperature, heating period to reach (a) 300 °C and (b) 325 °C, and during ageing at (c) 300 °C and (d) 325 °C up to 8 h for samples that were previously water-quenched (WQ) or air-cooled (AC) from the solution-treated condition.

5.3.4 Microhardness

The evolution of Vickers microhardness characteristics for the solution-treated and the aged alloy is shown in Fig. 5.6. The figure also shows the comparison of the microhardness values for the current work with the literature on water-quenched Ti-5553 β-Ti alloy. The water-quenched samples showed higher hardness after ageing when compared to the air-cooled samples. The obtained microhardness values for the current work are on the higher side when compared to the literature, as shown in Fig. 5.6. This additional increment in the hardness with respect to the literature values could be due to the presence of α″. The increment in the hardness by α″ is also dependent on its volume fraction in the matrix [144].

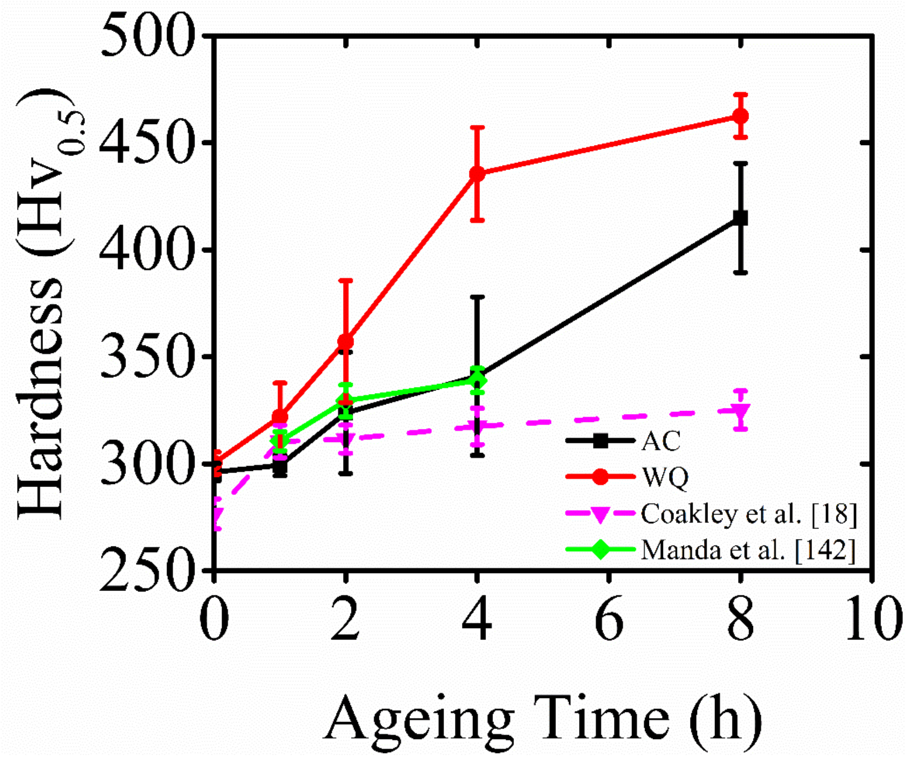

Fig. 5.6. The characteristic evolution of Vickers microhardness for Ti-5553 β-Ti alloy as a function of ageing time up to 8 h at 300 °C. The plot also shows the comparison of microhardness values obtained for the current work with the available values in the literature for same alloy after water quenching at same ageing conditions.

5.4 Discussion

5.4.1 Interpretation of SANS Measurements

Although the SEM showed a homogenised microstructure at room temperature, the virgin samples presented a SANS signal that can be described by Guinier and Porod models. The Guinier and Porod regimes are labelled as region I and region II in Fig. 5.7. Similarly, the SANS signals after the heating period (100 s of ageing data) can be divided into Guinier and Porod regimes, as shown in Fig. 5.7. The Porod regime exhibits q^{-4} behaviour (region II). The exponent –4 is related to a smooth interface between the precipitates and the matrix [138,155]. However, the Guinier regime (region I) shows an exponent value of 0. The Guinier regime is related to the real space regions of size > q^{-1} *i.e.* regions >> precipitates size. As explained in section 5.3.1, the inevitable ω_{ath} must be present in the solution-treated condition for metastable β-Ti alloys after water quenching and air cooling [18,26]. Thus, the scattering observed from region II at room temperature can be associated with the interfaces of athermal ω-phase and β-phase matrix [16,95,157]; although, there was no obvious scattering from the athermal ω-phase precipitates themselves. This can be due to the fact that athermal ω-phase and β-phases have the same composition [87]. This observation is similar to the observation of Coakley *et al.* [95] where they did not observe any scattering from athermal ω-phase in their SANS measurement work on water-quenched Ti-5553 β-Ti alloy samples: however, they did observe a similar decay of SANS signals at room temperature. In addition, they did not observe any scattering from the Guinier regime (region I), though this may be due to the *q* range they used (~0.01– 0.3 Å). It is also important to note here that the intensity of scattering decreased as the temperature was raised from room temperature to the ageing temperature (300 °C). This was not observed by Coakley *et al.* [95]. The drop in the intensity was much more pronounced in the water-quenched sample (Fig. 6 (a)) than the air-cooled sample (Fig. 6 (b)). The scattering curves in region II at room temperature and after heating seem to have the same slope, but there are deviations in region I for water-quenched and air-cooled samples, respectively, with a more significant deviation for the water-quenched material. We attribute this reduction of the SANS intensity to a homogenisation process of the partially resolved large scattering features as scattering is coming from the Guinier regime. Since the aim of this work is to investigate the creation and evolution of the isothermal ω-phase precipitates we will assume that once the metastable phase has been dissolved into the matrix, this contribution will remain constant during the thermal treatment and that the variations on the SANS are originated by the isothermal ω-phase precipitates.

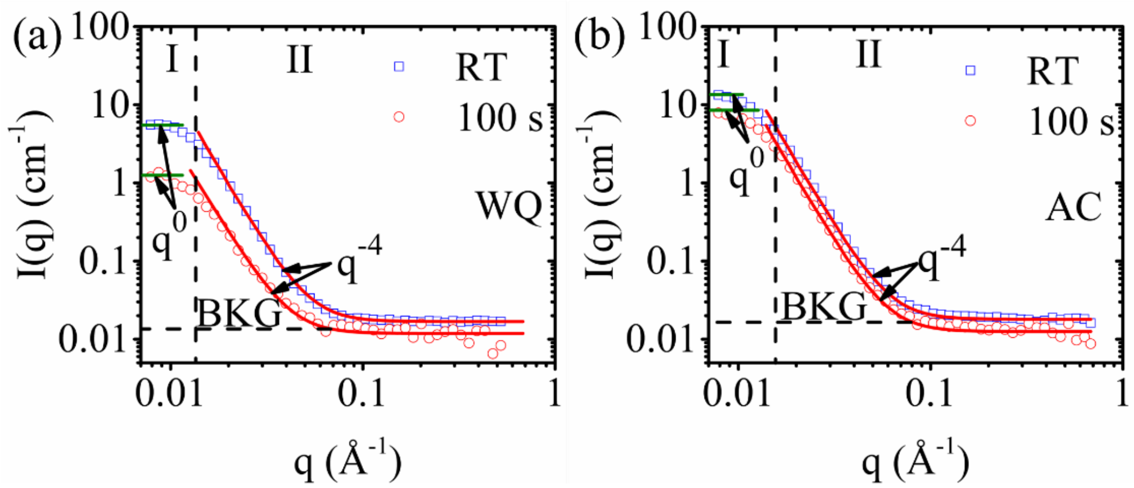

Fig. 5.7. One-dimensional plots of scattering intensity (I) vs scattering vector (q) for SANS measurements for Ti-5553 β-Ti alloy at room temperature (RT) and after the heating period (100 s of ageing data at 300 °C) after (a) water quenching (WQ) and (b) air cooling (AC) after solution treatment.

The SANS data collected for the aged samples can be divided into Guinier and Porod regions (Fig. 5.8); however, as the sample ages the *I* vs *q* decay at intermediate *q* values showed a deviation from the Guinier and Porod regime (Fig. 5.8 (a) and (b)) which indicated the scattering coming from the precipitates [40]. The segregation of different regions is shown in Fig. 5.8 (c) and (d) for water-quenched and air-cooled samples, respectively. The region I and III shows the scattering from the Guinier and Porod regime, respectively, whilst region II shows scattering from the precipitates.

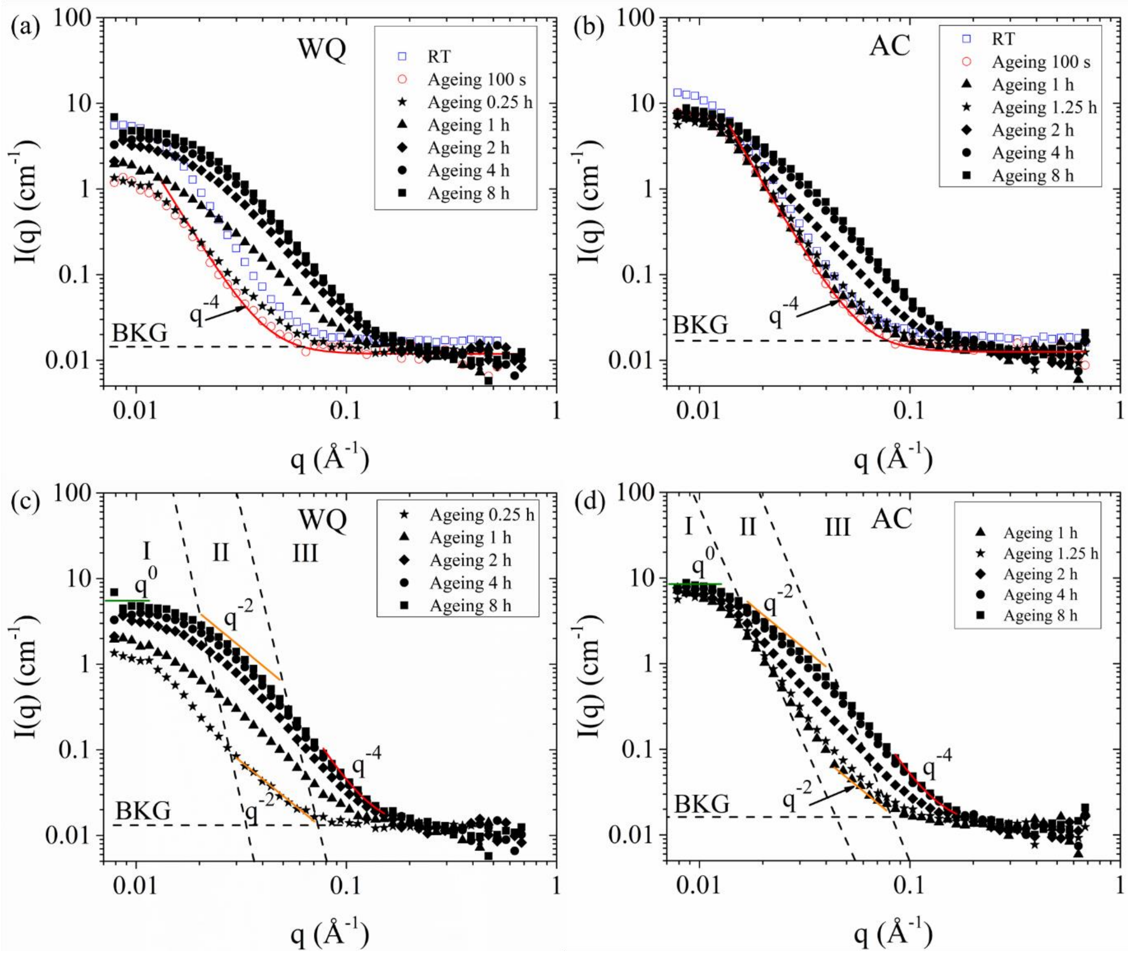

Fig. 5.8. One-dimensional plots for the whole measurement process for Ti-5553 β-Ti alloy samples after (a) water quenching (WQ) and (b) air cooling (AC) showing deviation in scattering from the Guinier-Porod regime during ageing, whilst (c) and (d) show the SANS signals produced during ageing at 300 °C up to 8 h after WQ and AC, respectively.

5.4.2 Model-independent Analysis

Firstly, the model-independent (shape-independent) analysis method was adopted to extract the useful information on the precipitate size and its volume fraction in the matrix. This method is based on following some standard plots that are useful in determining the precipitate characteristics without any particular assumption of its form (shape) [158]. For a polydispersed distribution of scattering features (region I and II), as understood from the *I vs q* plots in Fig. 5.8 (c) and (d), there is no simple relation for some of the standard plots (e.g. Guinier plot) to determine the particle characteristics

[159]. Hence, the simplest Kratky plots (Iq^2 vs q) were used to find out the characteristic precipitate size by calculating the pseudo-guiner radius (R_{max}) using the plots in Fig. 5.9. R_{max} can be obtained from the maximum q value (q_{max}) in the plot and using Equation (5.1). Numerical curve fitting was adopted to determine the q_{max} values in Fig. 5.9. A log-normal distribution of the precipitate size was assumed for curve fittings, as recommended in reference [159]. The obtained R_{max} values are presented in Table 3.1. Since the clear peak in the Kratky plots for ageing period data were observed from 2 h and 4 h of ageing the water-quenched (Fig. 5.9 (a)) and air-cooled (Fig. 5.9 (b)) samples respectively, hence, the R_{max} values for ageing period (Table 5.1) were determined from 2 h and 4 h of ageing.

$$R_{max} = \frac{\sqrt{3}}{q_{max}} \tag{5.1}$$

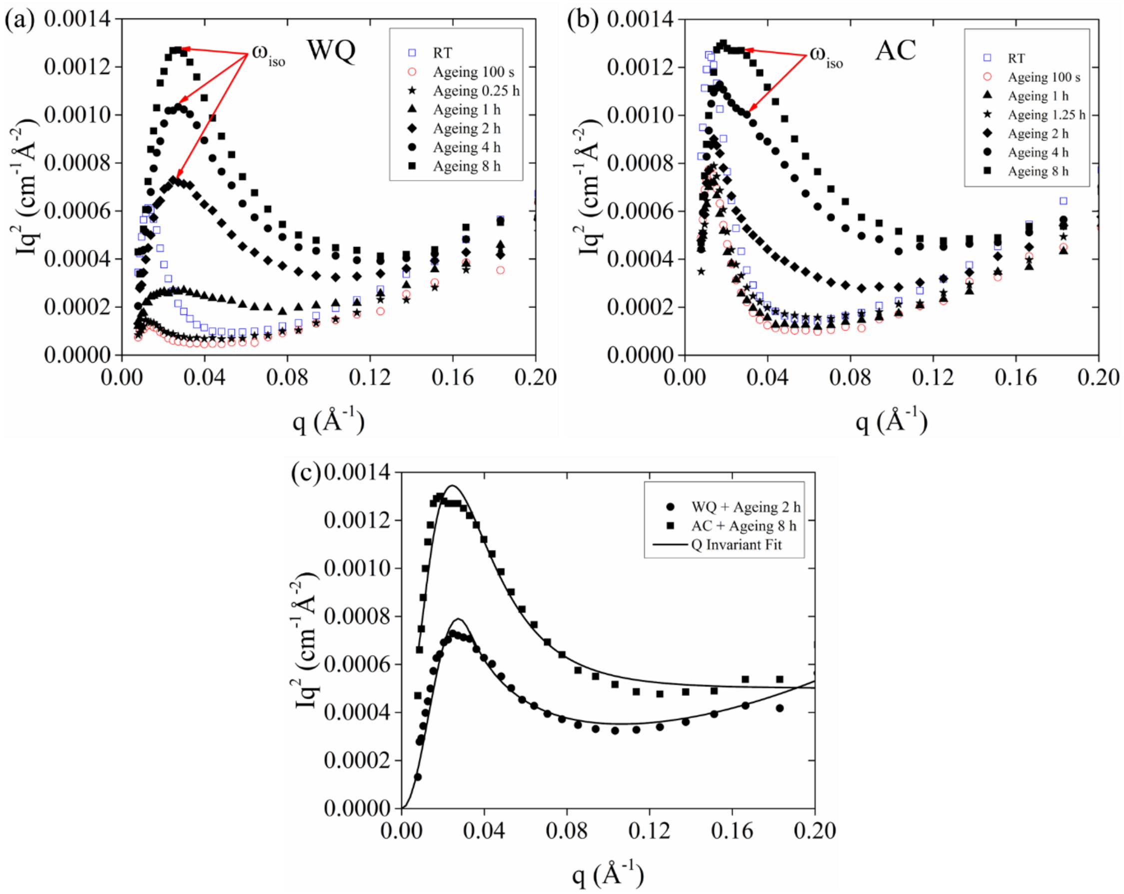

Fig. 5.9. The Kratky plots for the (a) water-quenched (WQ) and (b) air-cooled (AC) samples for the entire measurement process at 300 °C, and (c) shows the Q invariant fitting of the data to calculate the volume fraction.

Table 5.1. Characteristics of ω_{iso} precipitates formed during ageing at 300 °C up to 8 h, and determined from the analysis of SANS data using Kratky plots.

Transformation time	~Pseudo-Guinier radius, R_{max} (nm)		~Volume fraction, f_v(%)	
	WQ	AC	WQ	AC
Room temperature (RT)	13.5	13.5	–	–
After heating period (ageing 100s)	13.5	13.5	–	–
2 h	6.5	–	4.5	–
4 h	6.5	6.5	7.2	5.2
8 h	6.5	6.5	10.2	9.8

The area under the Kratky curves is proportional to the volume fraction (f_v) of the precipitates in a two-phase system [98]. The integrated small-angle scattering, Q, (Porod invariant) was used to calculate the volume fraction of isothermal ω-phase formed during the ageing time. The Q invariant is given by Equation (5.2), where ρ_ω and ρ_β represents the scattering length densities of isothermal ω-phase precipitate and the β-phase matrix, respectively. The f_v was calculated by fitting the Q invariant curves in the SASView software [160] within the error bars (± 0.0001 cm^{-1} Å^{-2}) of Kratky curves (Fig. 5.9). The error bars are not presented in Fig. 5.9 for better representation of data. The q-range for integration or Q invariant fit was extrapolated to 10^{-5} Å^{-1} for low q and 10 Å^{-1} for high q with the Guinier equation and the Porod law respectively, as recommended in reference [98]. The examples for Q invariant fit for water-quenched and air-cooled samples are shown in Fig. 5.9 (c). As two clear humps or clear peaks (indicating the presence of two different size precipitates) were observed for the air-cooled sample (Fig. 5.9 (b)), hence, only area under the high q region hump (indicating the presence of nanoscale isothermal ω-phase precipitates) was fitted (Fig. 5.9 (c)) for calculating the volume fraction of isothermal ω-phase precipitates formed during ageing (at 300 °C up to 8 h) of the air-cooled sample, as the scope of the work is to see the precipitation kinetics of isothermal ω-phase precipitates formed during ageing. The scattering length density (SLD) values for calculating the isothermal ω-phase precipitates volume fraction in the β-phase matrix was kept the same as obtained by Coakley *et al.* [57], where $\rho_\omega = -1.7 \times 10^{10}$ cm^{-2} and $\rho_\beta = -1.3 \times 10^{10}$ cm^{-2}.

$$Q = \int_0^\infty I(q) q^2 dq = 2\pi^2 \left(\rho_\omega - \rho_\beta\right)^2 f_v (1 - f_v) \tag{5.2}$$

The Kratky plot for the water-quenched sample (Fig. 5.9 (a)) indicates that there is a presence of scattering surfaces at the solution treated condition, however, the peak position of the curve is found to be at low q region indicating the precipitates of bigger size (Table 5.1), correlating with the observations from *I vs q* plots (Fig. 5.7). The area under the curve reduces upon completing the heating period (100 s of ageing data) indicating the homogenisation of large scattering features. The area under the Kratky curves, with peak position at high q, increases during ageing indicating an increase in the volume fraction of the isothermal ω-phase. The peak position after 2 h of ageing of the water-quenched samples almost become constant during the remaining ageing time indicating that the size of the precipitate remains constant during the ageing time, however, the volume fraction increases as the area under the curves increases. The air-cooled sample shows greater area under the room temperature curve indicating larger volume fraction of large scattering features. The area under the Kratky curve after 100 s of ageing of air-cooled sample does not decrease completely indicating the stability of the features. The curve starts increasing after 2 h of ageing and two humps observed in the curve can be associated with the presence of both bigger (large scattering features) and smaller sizes of isothermal ω-phase precipitates in the matrix. However, it is important to note that peak position for the air-cooled sample after precipitation of the smaller isothermal ω-phase precipitates becomes constant after 4 h of ageing and only the area under the curve increases indicating the increase in the volume fraction of the precipitates, but not the size.

In regards to the interpretation of the R_{max} values from the Kratky plots, the constant R_{max} values during ageing, as shown in Table 5.1, suggest a constant precipitate size during ageing that is in line with the observations of Coakley *et al.* [96] for their water-quenched Ti-5553 β-Ti alloy samples during ageing at 300 °C up to 8 h. Although, the f_v for ω_{iso} precipitates increased during ageing time for differently cooled samples.

5.4.3 Model Fitting of SANS Data

For model fitting of a monodisperse system having Guinier and Porod regions, the SANS intensity (I) is given by Equation 5.3,

$$I(q) = NV^2(\Delta\rho)^2P(q)S(q) + aq^{-4} + be^{[\frac{-q^2+R_g^2}{3}]} + BKG \tag{5.3}$$

where N refers to the number density of the precipitates per unit volume, V defines the volume of a single particle, $\Delta\rho$ defines the scattering length density (SLD) difference between the precipitate and the matrix, $P(q)$ is the particle shape function and BKG refers to an incoherent background scattering that is not desirable for data reduction [155]. $P(q)$ can be further defined in terms of form factors depending on the shape of the precipitates, as given in Equation 5.4. The form factor for ellipsoid shape precipitates (the model used in this work) has been described in Equation 5.5. $S(q)$ refers to the structure factor that incorporates the interparticle interference. A hard sphere model was considered in the current work, as recommended in [20], where $S(q)$ can be further defined as Equation 5.7. The scattering from the Guinier and Porod regions can be described by $be^{[\frac{-q^2+R_g^2}{3}]}$ and aq^{-4} respectively [18,142], where a and b are the scale factors for model fitting. R_g refers to the radius of gyration indicating the characteristic size factor for the Guinier region.

$$P(q) = \int_0^\infty F(q,r)^2 dr \tag{5.4}$$

$$F_{\text{ellipsoid}}(q,r) = 3\,\frac{(\sin(qr) - qr\cos(qr))}{(qr)^3} \tag{5.5}$$

where r can be obtained from Equation (5.6)

$$r = [R_e^2 \sin^2\alpha + R_p^2 \cos^2\alpha]^{0.5} \tag{5.6}$$

R_e and R_p refer to the equatorial and polar radii perpendicular and along the rotational axis of the ellipsoid respectively, whilst α represents the angle between the axis of the ellipsoid and q.

$$S(q) = \frac{1}{(1 - C(q))} \tag{5.7}$$

$C(q)$ can be defined in terms of volume fraction V_{HS} and diameter (D) of the hard spheres, as described in Equation (5.8)

$$C(q) = -\frac{24V_{HS}}{(qD)^6}[\beta(qD)^3(\sin qD - qD\cos qD) + \gamma(qD)^2\{2qD\sin qD - (q^2D^2 - 2)\cos qD - 2\} + \delta\{(4q^3D^3 - 24qD)\sin qD - (q^4D^4 - 12q^2D^2 + 24)\cos qD + 24\}] \tag{5.8}$$

where β, γ and δ can be defined by Equation (5.9), (5.10) and (5.11) respectively.

$$\beta = \frac{(1+2V_{HS})^2}{(1-V_{HS})^4} \tag{5.9}$$

$$\gamma = -6V_{HS}\frac{(1+\frac{V_{HS}}{2})^2}{(1-V_{HS})^4} \tag{5.10}$$

$$\delta = \frac{1}{2}V_{HS}\frac{(1+2V_{HS})^2}{(1-V_{HS})^4} \tag{5.11}$$

The model fitting of SANS data was undertaken in SASView software [160] to find out the real-space precipitate size. Based on the understanding from literature [17,145], both disc and ellipsoid shape model fittings were considered for the SANS measurements. However, the ellipsoid shape model fitting provided better fit, which was determined based on the residuals and Chi-squared values. Curve fitting applied to the experimental data was performed by maintaining contrast values for isothermal ω-phase precipitates (ρ_ω = –1.7 × 10^{10} cm^{-2}) and the β-phase matrix (ρ_β = –1.3 × 10^{10} cm^{-2}), as obtained by Coakley *et al.* [95]. The R_g values of LSS (seen in Guinier region) were calculated first using the Kratky plots (Fig. 5.9). These values were kept constant whilst doing the model fitting as shown in Equation 5.3. The evolution of isothermal ω-phase precipitates during ageing in terms of size and volume fraction is shown in Fig. 5.10 and Fig. 5.11, respectively.

It can be seen from Fig. 5.10 that the isothermal ω-phase precipitates attained an approximate maximum stable polar radius (R_p) after ~1 h and ~3 h of ageing at 300 °C in the water-quenched and air-cooled samples, respectively. However, the equatorial radius (R_e) became approximately constant after 2 h and 4 h of ageing the water-quenched and air-cooled samples, respectively. The formation of a stable size of ω_{iso} precipitates after 2 h of ageing was also observed by Coakley *et al.* [96] during ageing of water-quenched Ti-5553 β-Ti alloy. This can also be confirmed from the Kratky plots (Fig. 5.10). It could also be observed from Fig. 5.10 (b) that the polar dimension attained stable size earlier than the equatorial radius. This may be due to the higher strain field at the $\omega_{\text{iso}}/\beta$ interface, which leads to the preferential growth in <111> β directions, as observed by Sun *et al.* [101]. The SANS model-fitted dimensions of isothermal ω-phase precipitates along the equatorial dimensions (~ 21 nm) after 8 h ageing the water-quenched sample lies in the range of TEM observations (~10–50 nm) reported in the literature [17,57].

The characteristic evolution of the volume fraction of isothermal ω-phase precipitates obtained from the ellipsoid model fitting is shown in Fig. 5.11. The volume fraction increased with ageing time. Both the samples (water-quenched and air-cooled) showed approximately similar volume fraction (~11 %) after 8 h of ageing at 300 °C. This is in agreement with the observations of Coakley *et al.* [57] where they reported a volume fraction of ~10 % for the water-quenched Ti-5553 β-Ti alloy after the same ageing condition. The qualitative understanding of Chen *et al.* [97] (based on their TEM observation) showed that increment in the cooling rate increases the number density of isothermal ω-phase precipitates. However, from the current observations, it is stated that the delayed nucleation does happen with the slow cooling rate, but approximately the same volume fraction is observed once the saturation stage is reached.

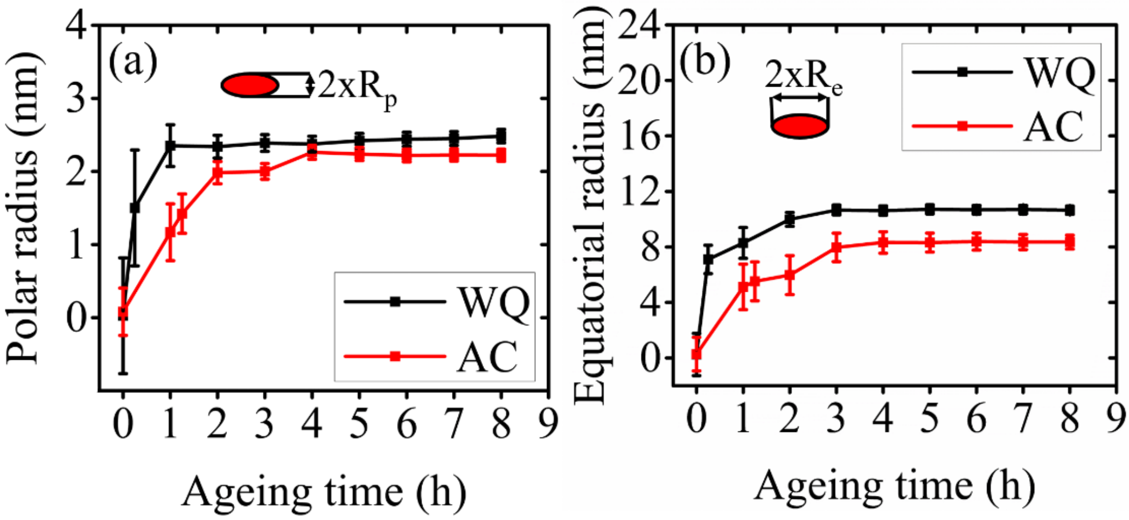

Fig. 5.10. The evolution of ω-phase precipitate during the ageing time at 300 °C up to 8 h after water quenching and air cooling. (a) shows the characteristic polar size of the precipitates, whilst (b) shows the evolution in the equatorial dimension of the precipitate.

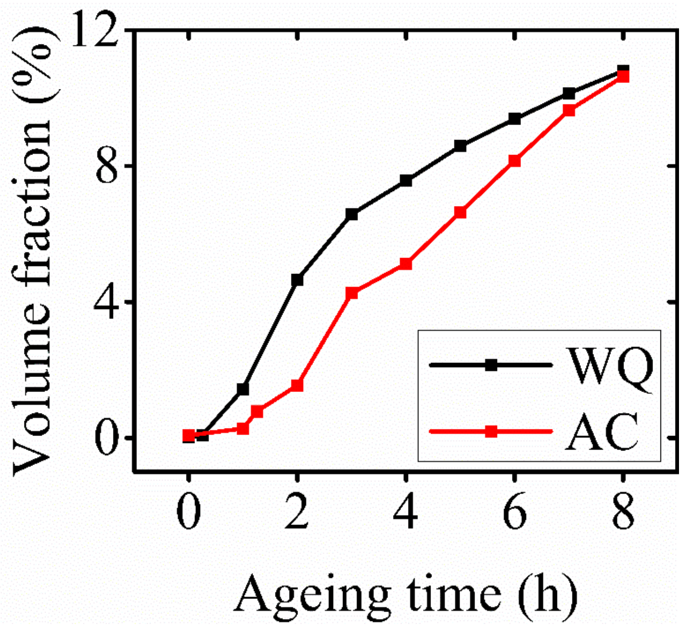

Fig. 5.11. The evolution of volume fraction of isothermal ω-phase precipitates obtained from the ellipsoid model fitting. It could be seen from the plot that the volume fraction increased as a function of ageing time.

5.4.4 Analysis of Initial Trends upon Heating

Upon heating, there is a drop in the electrical resistivity of both the air-cooled and water-quenched samples. This initial drop in the electrical resistivity can be associated with the partial disappearance of athermal ω-phase as seen previously [150–152]. This drop is of similar magnitude and rate (Fig. 5.5 (a)), therefore, it can be assumed that the volume fraction of athermal ω-phase is similar between the both the samples at room temperature and is unaffected by the cooling rate difference. This could also be confirmed from the similar microhardness values after solution treatment for both cooling variants. It is also important to note that the β grain size remained approximately the same.

Upon heating, the SANS data also show a drop in total scattered intensity. The observed decay of the SANS signal in the initial stages of the thermal treatment are different in both samples. The reduction in the air-cooled sample is smaller than the one observed in the water-quenched sample. Our interpretation of that effect is that the large scattering features formed during the initial cooling process is related to the cooling rate: A slower cooling rate will produce a much more stable volume fraction of these large scattering features (Fig. 5.9 (b)). This could be attributed to the fact that slower cooling has allowed diffusion to happen that has provided an ageing effect leading to the higher degree of solute partitioning for the air-cooled sample, as observed by Chen *et al*. [156].

5.4.5 Precipitation Kinetics

The transformed fraction (F) of isothermal ω-phase precipitates obtained from electrical resistivity measurements during ageing at 300 °C and 325 °C are presented below in Fig. 5.12. The transformed fraction represents the ratio between the volume fraction of isothermal ω-phase precipitates at time t during ageing and the volume fraction formed at the metastable equilibrium state [161,162] and is given by Equation 5.12.

$$F = \frac{\rho_t - \rho_0}{\rho_{\text{meta}} - \rho_0} \tag{5.12}$$

where ρ_t refers to the electrical resistivity of the alloy at time t during ageing period, ρ_0 refers to the electrical resistivity of the alloy at the beginning of ageing, and ρ_{meta} refers to the electrical resistivity of the alloy at the end of the ageing time.

It could be seen from the electrical resistivity results (Fig. 5.5) that the water-quenched and air-cooled samples showed similar trends, but the air-cooled samples showed a delay in the nucleation of the isothermal ω-phase precipitates (Fig. 5.12). Also, the nucleation behaviour showed transient nucleation kinetics for both the cases i.e. an incubation time (τ) is required to reach the critical nucleation size. This early nucleation in the water-quenched sample could be attributed to the higher dislocation density in the sample [49]. In addition, Chen *et al.* [156] reported that an air-cooled sample has shown a higher degree of solute partitioning due to the ageing effect during air cooling. This would make the β-phase matrix of the air-cooled sample more stable at room temperature, and a higher amount of energy would be required during ageing for separation of other phases from the stable matrix. This could be another reason for the delay in the nucleation of the ω_{iso} precipitates in the air-cooled sample, as observed in SANS (Fig. 5.11) and electrical resistivity data (Fig. 5.12). The obtained trend at the beginning of the transformed fraction correlates to the evolution trend of isothermal ω-phase volume fraction obtained from SANS data fit (Fig. 5.11). However, the electrical resistivity data (Fig. 5.12) shows a transformed fraction of ω_{iso} precipitates that almost saturates between 4–6 h of ageing, whilst the volume fraction obtained from SANS data (Fig. 5.11) showed an increasing trend even after reaching 6 h of ageing time. The intensity of the SANS signals is directly dependent on the volume fraction of the precipitates or the difference in the SLD values of the precipitate and the matrix phase (see Equation 5.3). As indicated by Equation 5.3, a slight variation in the SLD values or the volume fraction will cause the change in the scattering intensity of the SANS signals. In the present work, the SLD is held constant during refinement. However, it is possible that the SLD values of the precipitates and the matrix phase will evolve during the ageing as the formation of isothermal ω-phase happens by a diffusional process, leading to a slight change in the calculated volume fraction of ω_{iso} precipitates. It is important to note here that the initial trends for ω_{iso} evolution obtained from SANS (Fig. 5.11) and electrical resistivity data (Fig. 5.12) matches qualitatively.

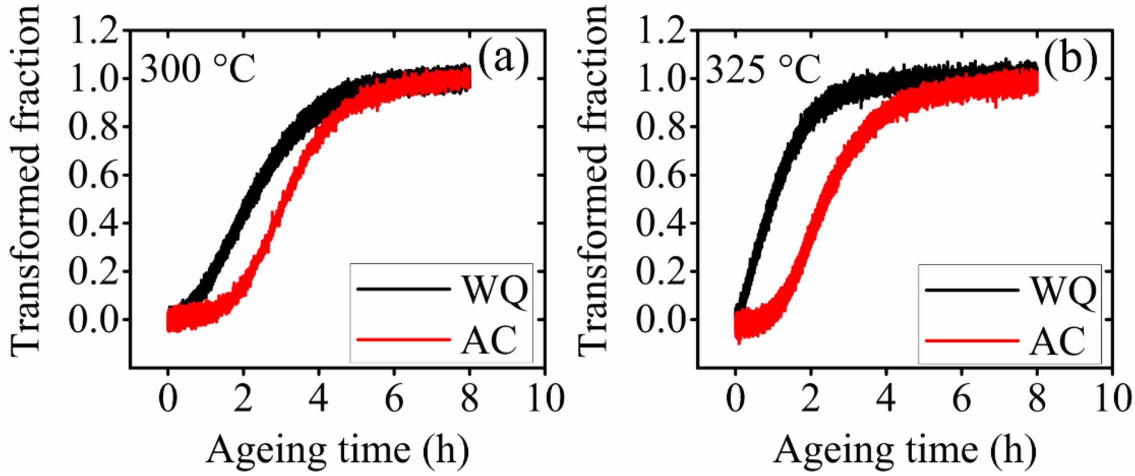

Fig. 5.12. Kinetic curves showing the isothermal ω-phase transformed fraction vs. ageing time: at (a) 300 °C and (b) 325 °C. The air-cooled (AC) sample showed a delayed nucleation of isothermal ω-phase precipitates when compared to water-quenched (WQ) sample.

5.4.6 Precipitation Mechanism

The universal Johnson-Mehl-Avrami-Kolmogorov (JMAK) model can be used to understand the isothermal transformation kinetics under specific assumptions [163]. However, the transient nucleation as observed from the transformed fraction (Fig. *5.12*) violates the universal JMAK model [163,164]. Hence, a modified JMAK model was used to understand the isothermal transformation kinetics of isothermal ω-phase precipitates. The modified JMAK model is given by Equation 5.13 [101,163].

$$F(t) = 1 - \exp\left(-K_T(t-\tau)^m\right) \tag{5.13}$$

$$K_T = k_0 e^{-E_a/RT} \tag{5.14}$$

Where m represents the Avrami exponent that is indicative of the precipitation mechanism, K_T is the thermally activated rate constant dependent on the nucleation and growth rate. This can be determined from the Arrhenius relation (Equation (5.14)), where E_a is the activation energy, R is the universal gas constant and T is the absolute temperature of isothermal ageing. τ refers to the incubation time required to achieve a steady-state precipitate size.

The Avrami exponent, m, was determined over the full range of ω_{iso} precipitation at 300 °C and 325 °C using Equation (5.15) and the gradients are shown in Fig. 5.13.

$$ln[-ln(1-F)] = lnK_T + mln(t-\tau) \tag{5.15}$$

The τ values obtained for water-quenched and air-cooled samples are ~0.25 h and ~1.25 h, respectively. An m value of approximately 1.35 (see Fig. 5.13) at the early stage of transformation is indicative of a pure growth mechanism from a pre-existing nucleation site [101,163]. This is in line with the growth of isothermal ω-phase precipitates from athermal ω-phase [16]. However, the m values reduce at later stages of transformation (Fig. 5.13 and Table 5.3). This reduction in the m values has been attributed to the dimension loss for isothermal ω-phase precipitates at later stages of precipitation due to high misfit strain at the ω_{iso}/β interface [101]. This can also be confirmed with the SANS measurement results during the early stage of transformation (Fig. 5.10). For water-quenched and air-cooled samples during ageing at 300 °C, the deviation in m values were observed after ~40% and ~60% of transformation (Fig. 5.13), respectively. This is in reasonable agreement with the SANS observations (Fig. 5.10), where an approximate stable size of isothermal ω-phase precipitates was achieved during ageing time between 1–2 h for water-quenched sample (~40% of transformation) and 2–4 h for air-cooled sample (~60% of transformation) after growth along the major axis. Table 5.2 shows the list of Avrami exponent (m) values along with corresponding precipitation mechanism predicted by them.

Table 5.2. List of Avrami exponent (m) values along with corresponding precipitation mechanism predicted by them [165].

Avrami exponent	Growth geometry	Rate determination
1<m<2	One-dimensional, rod like	Diffusion
2<m<3	Two-dimensional, disc like	Diffusion
3<m<4	Three-dimensional, spherulitic	Contact

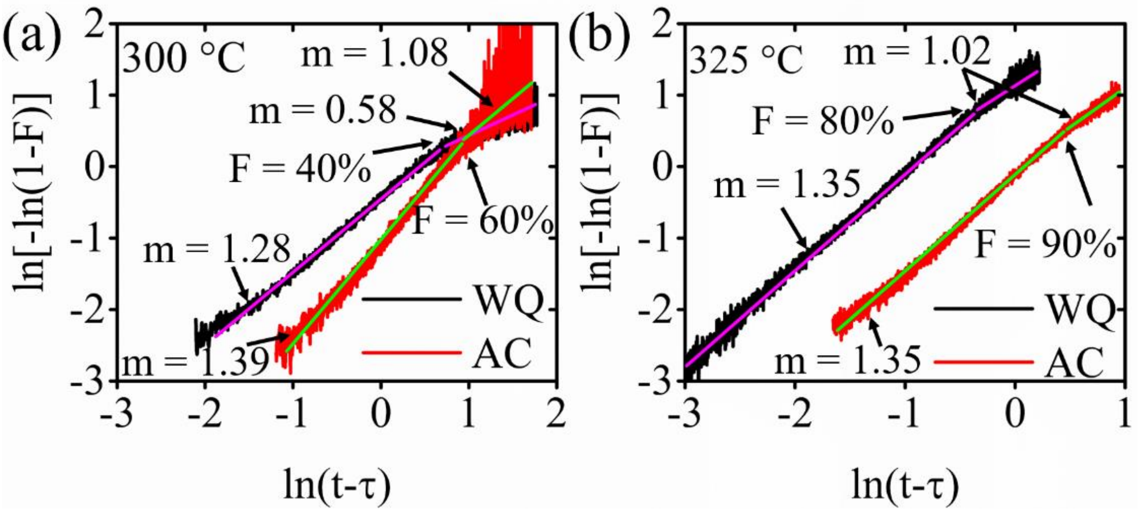

Fig. 5.13. The modified JMAK plots for Avrami exponents (m) during isothermal ω-phase transformation as a function of WQ and AC at (a) 300 and (b) 325 °C.

The analysis of the electrical resistivity measurements using the modified JMAK model indicate that the activation energy (E_a) for the formation of isothermal ω-phase in the air-cooled sample is high compared to water-quenched sample (Table 5.3). Hence, this can assist in rationalising the increased incubation time (τ) for isothermal ω-phase nucleation in the air-cooled sample as compared to the water-quenched sample (Fig. 5.12). The average value of the activation energy for the formation of isothermal ω-phase precipitates from the β-phase matrix was calculated as ~122 kJ mol^{-1}. This value is in agreement with the activation energy for the diffusion of Mo atoms in the Ti substrate (~135 kJ mol^{-1}) [47]. Being the slowest diffusing element [48] in the current alloy indicates that the formation of isothermal ω-phase precipitates is controlled by the diffusion rate of Mo, as reported earlier [49]. This is a good evidence to state that the electrical resistivity can pick up the β to isothermal ω-phase precipitates transformation. The observance of similar trends via electrical resistivity measurements and SANS measurements indicates the same transformation, *i.e.* β to isothermal ω-phase precipitates transformation.

Table 5.3. The Avrami exponent (m) and activation energy (E_a) values for entire nanoscale ω_{iso} precipitate transformation during ageing at 300 °C and 325 °C up to 8 h.

ST	Temperature (°C)	Early-stage transformation			Later stage transformation
		n (±0.05)	K_T ($\times 10^{-3}$)	E_a (±12 kJ mol^{-1})	n (±0.05)
WQ	300	1.28	16.84	114	0.58
	325	1.35	45.78		1.02
AC	300	1.39	3.18	131	1.08
	325	1.35	10.05		1.02

5.5 Conclusions

A combination of *in-situ* small-angle neutron scattering (SANS) and electrical resistivity measurement techniques was used to study the kinetics of isothermal ω-phase (ω_{iso}) precipitates during isothermal ageing at 300 °C and 325 °C up to 8 h as a function of different cooling rates from solution treatment temperature (water quenching (WQ) and air cooling (AC)). The following conclusions can be drawn:

1. Air-cooled samples showed a delayed nucleation of ω_{iso} precipitates when compared to water-quenched samples during ageing at 300 °C.
2. The volume fraction became approximately the same (~11 %) after ageing for 8 h although the air-cooled samples showed slower nucleation in comparison to water-quenched samples,

3. The ellipsoidal ω_{iso} precipitates achieved a maximum size (equatorial diameter = ~21 nm and ~17 nm) after 2 h and 4 h of ageing the water-quenched and air-cooled samples, respectively.
4. The Avrami exponent decreased at higher transformed fraction indicating the dimension loss during the growth of the ω_{iso} precipitates due to the high misfit strain at β/ω interface. This is in line with the SANS observations where only the equatorial dimension of ω_{iso} precipitates grew in the later stages of transformation before achieving the maximum size.
5. The Vickers microhardness results showed an increasing trend with ageing time up to 8 h when aged at 300 °C, where water-quenched samples showed higher hardness compared to air-cooled samples.

The results in this chapter have shown the precipitation behaviour of the wrought alloy. However, in the modern era, there is a need to produce these alloy parts to near-net shape with less wastage of material. This led to the work presented in the following chapter to study the precipitation behaviour of the additively manufactured β-Ti alloy.

CHAPTER 6

THE AGEING RESPONSE OF ADDITIVELY MANUFACTURED β-Ti ALLOY

6.1 Introduction

This chapter presents a study into the ageing response (at different ageing temperatures and times) of Ti-5553 β-Ti alloy deposited using laser engineered net shaping, a direct laser deposition technique, that has the capability to directly produce complex aerospace parts. The different post-processing pathways (single ageing and duplex ageing) for as-built samples were explored to critically understand the influence of heat treatment upon part microstructure (section 6.3.2) and the mechanical properties (section 6.3.3). The influence of different heating rate during single ageing was also introduced to see the likely effect on the evolved microstructure. A correlation between the evolved microstructure and the microhardness was established in section 6.4.7. An *in situ* electrical resistivity measurement technique was used to study the precipitation kinetics of isothermal ω-phase during low temperature (300 °C and 325 °C) ageing. The electrical resistivity measurement was done for both the as-built and the solution-treated samples so that influence of sub-structures on the kinetics can also be understood.

6.2 Experimental Details

The samples were deposited as double-walls (40 mm × 10 mm × ~1.5 mm) using laser engineered net shaping method. The deposition strategy has been explained in section 3.1.2. The solution and ageing heat treatments employed for the wrought alloy in section 4.2 above were used for heat treating AM samples. The schematics of heat treatment cycles are shown in Fig. 6.1. The samples were sectioned as 10 mm × 10 mm

× 1.5 mm for ageing treatments. Two different heating rates (~100 °C/min and ~5 °C/min) were introduced during single ageing to see the influence of heating rate on the microstructure evolution. For duplex ageing, the samples were pre-aged at 300 °C for 8 h before the final ageing at higher temperature. The heat treatment cycle is shown in Fig. 6.1 (c). Some as-built samples were solution-treated at 900 °C for 0.5 h to remove the sub-structures formed and see the subsequent effect on the microstructure after aging. The solution treatment cycle is shown in Fig. 6.1 (d). The heat treatment procedures are further explained in section 3.2. The metallography and characterisation details are explained in section 3.3.

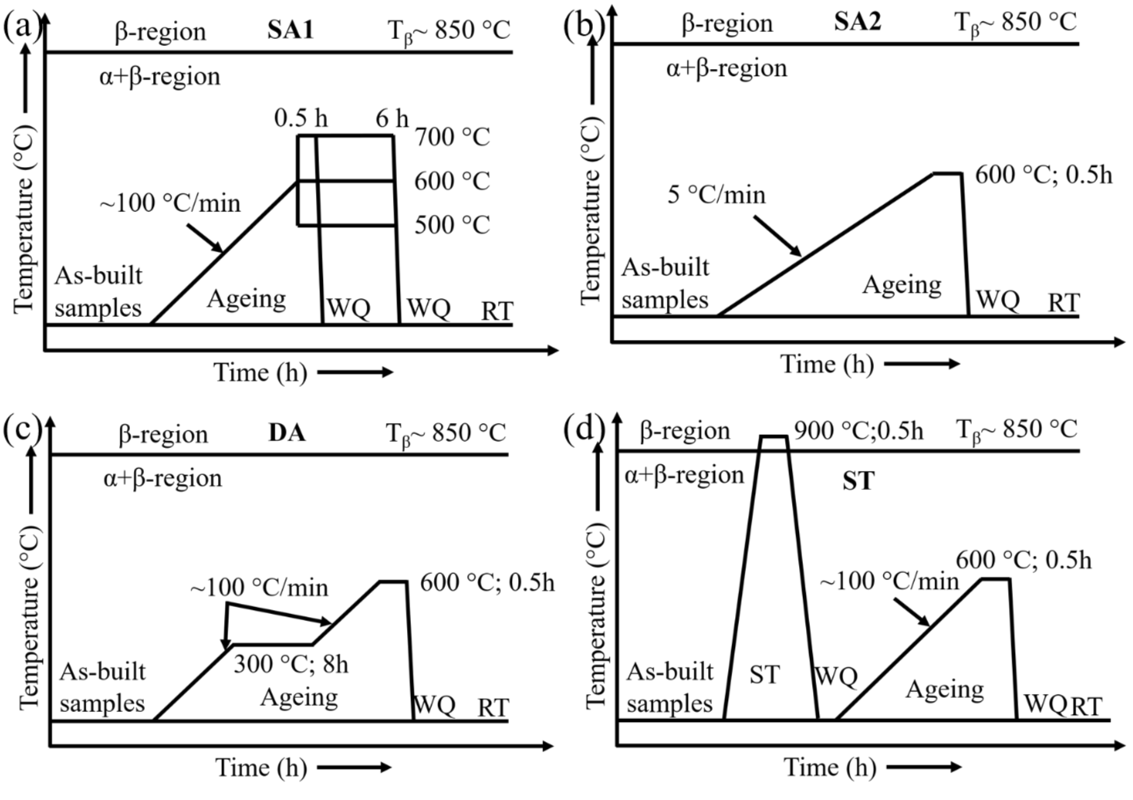

Fig. 6.1. The schematics of the heat treatment cycle used to understand the ageing response of additively manufactured (AM) Ti-5553 β-Ti alloy. The heat treatment was carried out using different parameters: (a) fast heating rate plus single ageing (SA1), (b) slow heating rate plus single ageing (SA2), (c) duplex ageing (DA), and (d) solution treatment plus single ageing (ST).

In-situ electrical resistivity measurements were recorded during ageing at 300 °C and 325 °C for 15 h on the as-built and solution-treated samples to understand the kinetics of isothermal ω-phase formation. The details of the experimental procedure can be seen in section 3.3.9, and the schematics of the heat treatment cycle are shown in Fig. 6.2.

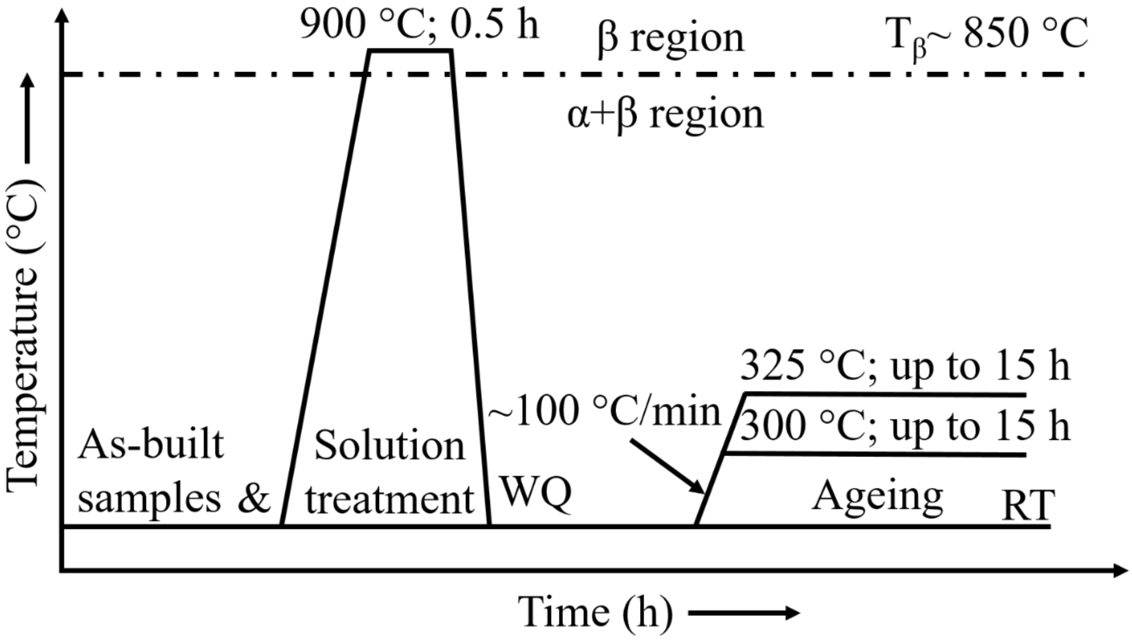

Fig. 6.2. The schematics of the heat treatment cycle used to perform the electrical resistivity measurements on the as-built and the solution-treated samples to understand the kinetics of isothermal ω-phase during low-temperature (300 °C and 325 °C) ageing.

6.3 Results

6.3.1 Microstructural Characterisation

The as-built samples showed the presence of spherical gas pores (19-62 µm) mostly distributed at the edges, as shown in Fig. 6.3. The average number density per unit area was calculated as ~0.22 mm^{-2}.

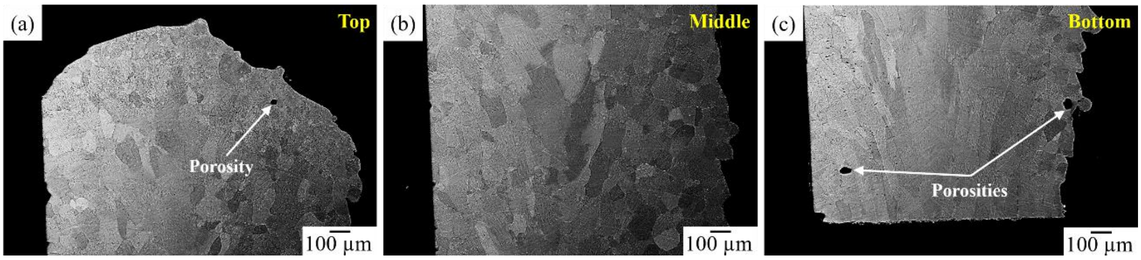

Fig. 6.3. SEM micrograph of as-built sample showing the presence of porosities at the (a) Top, (b) Middle, and (c) Bottom of the sample.

The EBSD map of the cross-section of the as-built sample is shown in Fig. 6.4 (a). The as-built samples exhibited the presence of solely β-phase matrix in the microstructure (Fig. 6.4 (b)), however, the presence of an athermal ω-phase is expected as the formation of athermal ω-phase is inevitable during cooling from the β-phase region irrespective of the cooling rate [16]. Elongated β grains were present in the sample, where the sample showed more elongation towards the bottom of the as-built sample. However, more equiaxed grains were present on one side of the sample compared to the other side. The width of the β-phase remained approximately the same from top to bottom as 184 ± 66 µm. The as-built samples showed texture in <100> direction, and the texture intensity was measured as 4 times the random, as shown in Fig. 6.4 (c). The scan (melt pool) tracks are also visible in the micrograph (Fig. 6.4 (b)) throughout the sample.

The microstructure (Fig. 6.4 (b)) also revealed the presence of sub-structures within the β grains. These sub-structures showed either cell or cellular-dendritic morphology with dendritic long axes perpendicular to the scan track boundaries, in agreement with the maximum heat flow direction. The sub-structures are present below the scan track boundaries; however, the sub-structures were not present in certain regions above the scan tracks. The sub-structures showed cellular morphology just below the scan tracks and then became cellular-dendritic as we reach towards the area free from the sub-structure at the top of the next scan track. However, the sub-structures primarily followed cellular-dendritic morphology towards the bottom of the sample, followed by sub-structure free region. The sub-structure width varied in the range of 14 ± 4 µm.

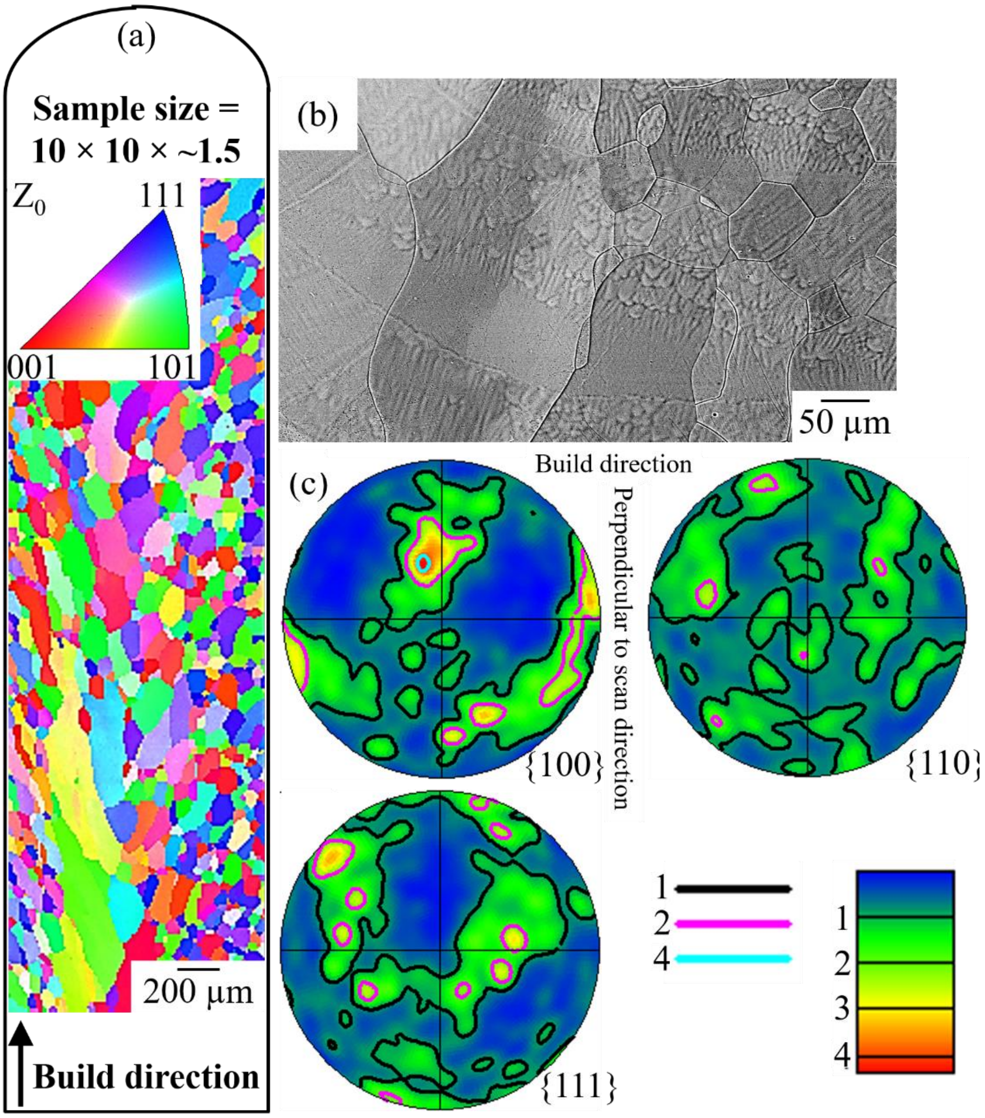

Fig. 6.4. (a) The EBSD map of the cross-section of the as-built sample showing the characteristics of β-phase along the build direction. (b) shows the SEM micrograph of the as-built sample showing the presence of solely β-phase and the cellular sub-structures after deposition. (c) shows the pole figures for the as-built sample showing the texture along the <100> direction with texture intensity as 4 times random.

The EDS analysis (Fig. 6.5) of the as-built samples revealed that these sub-structures (point 1) were slightly rich in Mo (6.3 wt%), while depleted in Cr (1.9 wt%). The sub-structure boundaries (point 2) were slightly depleted in Mo (5.5 wt%) and rich in Cr (2.3 wt%). This remains true for both cellular and cellular-dendritic sub-structures. However, the remaining elements (Ti, V, and Al) did not show any observable segregation.

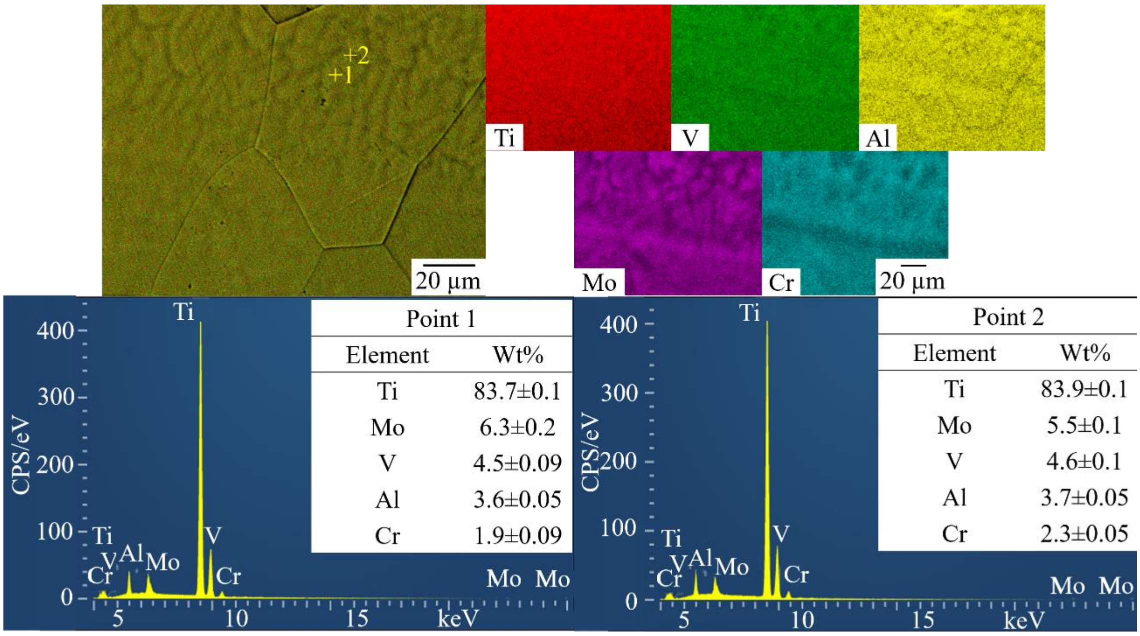

Point 1	
Element	Wt%
Ti	83.7±0.1
Mo	6.3±0.2
V	4.5±0.09
Al	3.6±0.05
Cr	1.9±0.09

Point 2	
Element	Wt%
Ti	83.9±0.1
Mo	5.5±0.1
V	4.6±0.1
Al	3.7±0.05
Cr	2.3±0.05

Fig. 6.5. The energy dispersive spectroscopy maps and point analysis done on the sub-structures (point 1) and sub-structures boundaries (point 2) to find out their elemental composition.

The solution-treated sample did not show the presence of sub-structures, and only β-phase was present, as shown in Fig. 6.6. The EBSD analysis of the solution-treated sample also showed a similar microstructure as the as-built sample. The width of β-phase was measured as 187 ± 65 µm, which is approximately the same as the as-built sample.

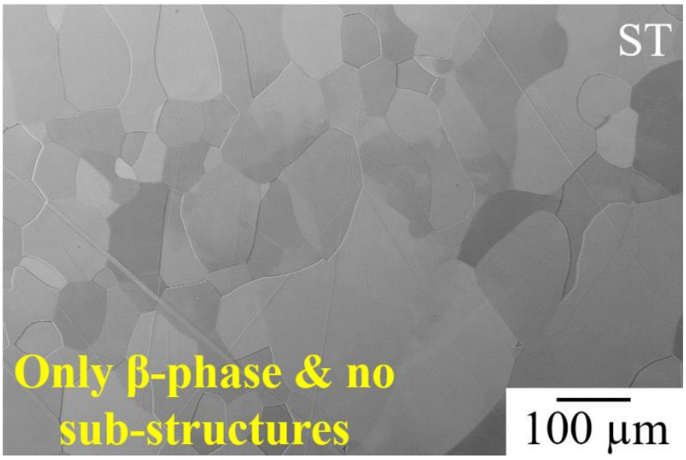

Fig. 6.6. The BSE SEM microstructure of the solution-treated (ST) sample showing the presence of solely β-phase without any sub-structures.

6.3.2 Aged Microstructure

The as-built and solution-treated samples showed differences in their subsequent ageing response. Fig. 6.7 (a) and (b) show the microstructures of the two samples following an ageing heat treatment of 600 °C for 0.5 h. A generally more refined intragranular α-phase was observed for the as-built sample compared to solution-treated sample after ageing. Both samples showed a similar self-accommodating acicular morphology of intragranular α-phase. However, the solution-treated sample exhibited a lamellar α-phase morphology near to the grain boundaries. The solution-treated sample also showed Widmanstätten α-phase in the aged condition, that grows from the grain boundary α-phase to the interior of the β grains.

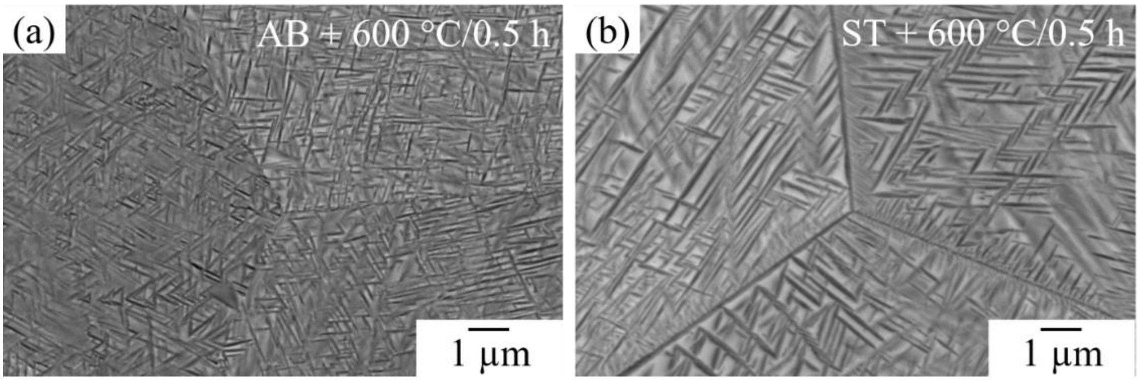

Fig. 6.7. The BSE-SEM microstructure of aged (600 °C/0.5 h) Ti-5553 β-Ti alloy (a) directly after deposition (AB) and (b) after solution treatment (ST), illustrating the grain boundary and intragranular α-phase characteristics.

The volume fraction of intragranular α-phase was similar (~52%) for both the aged samples. The width of intragranular α-phase was larger for the solution-treated sample (139 ± 22 nm) compared to as-built sample (103 ± 20 nm), based on a measurement of 150 α-phase particles. The interparticle (α-phase) spacing for as-built plus aged and solution-treated plus aged samples was found to be about 137 ± 17 nm and 187 ± 16 nm respectively.

The width and morphology of the α-phase precipitates remained uniform within sub-structure and sub-structure free regions *i.e.* there was no local effect of the sub-structure formation for as-built plus aged sample, as shown in Fig. 6.8. In addition, thinner and discontinuous grain boundary α-phase was observed for the as-built plus aged sample, whilst a thicker and continuous α-phase was observed for the solution-treated sample after ageing. The as-built and solution-treated samples did not show any observable difference in the width and morphology of the α-phase along the build height.

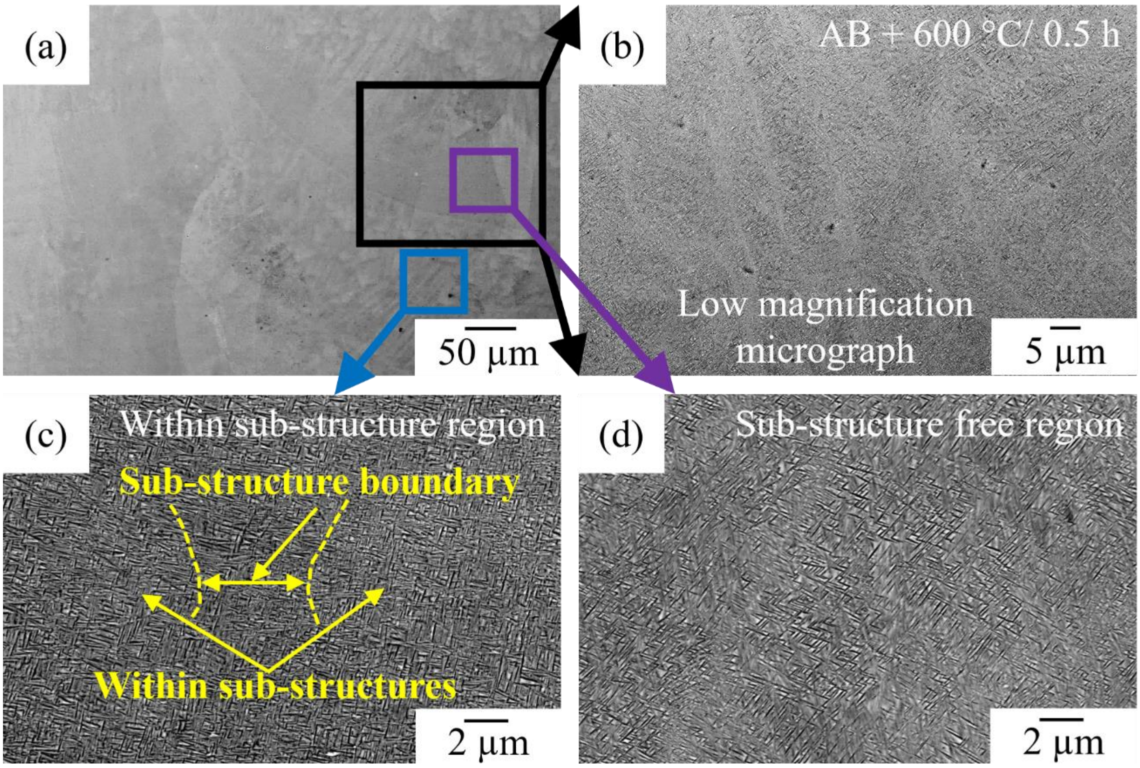

Fig. 6.8. BSE-SEM microstructure of aged (600 °C/0.5 h) Ti-5553 β-Ti alloy showing (a) the presence of sub-structures after ageing. (b) shows low magnification SEM micrograph showing uniform distribution of intragranular α-phase across the sub-structures and sub-structure free regions. AB refers to the as-built sample. (c) and (d) shows the high magnification SEM micrographs from sub-structures and sub-structure free regions, respectively. No observable difference in the α-phase characteristics were observed across the different regions.

The microstructure of the single aged (500 °C and 700 °C for 0.5 h) as-built samples are shown in Fig. 6.9 (a) and (b), respectively. The micrographs show the presence of self-accommodating acicular α-phase morphology similar to the wrought alloy. No Widmanstätten α-phase was observed for aged as-built samples as observed in wrought and solution-treated (after deposition) samples. Precipitate free zones (PFZ) were observed near grain boundaries for as-built plus agedsample aged at 700 °C. PFZ were not seen in the single-aged wrought alloy. The slow-heated (Fig. 6.9 (c)) and duplex aged (Fig. 6.9 (d)) samples showed a very refined microstructure, similar to the wrought alloy. In addition, duplex aged and slow-heated samples also showed the presence of a very narrow PFZ.

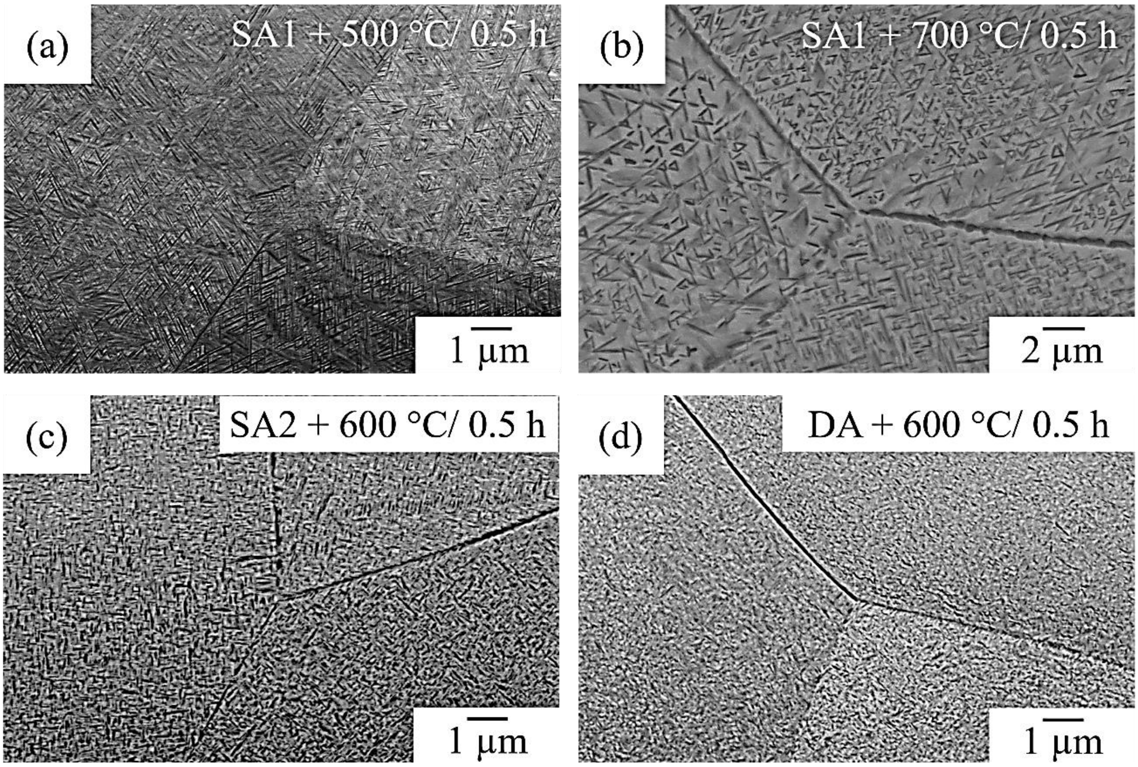

Fig. 6.9. The BSE SEM microstructure of the as-built Ti-5553 β-Ti alloy samples aged (a) using the fast heating rate at 500 °C and (b) 700 °C for 0.5 h. (c) and (d) shows the aged microstructure after slow heating and duplex ageing at 600 °C for 0.5 h, respectively. SA1 refers to the single ageing with fast heating rate, SA2 refers to the single ageing with slow heating rate, and DA refers to the duplex ageing.

The volume fraction, width and interparticle spacing of the α-phase precipitates are shown in Fig. 6.10 (a), (b) and (c) respectively. Irrespective of the ageing process, the volume fraction of intragranular α-phase was found to be a maximum (~52%) after heat treatment at 600 °C. The volume fraction remained approximately the same for single-aged as-built samples after ageing for 0.5 h and 6 h at 600 °C. This is similar to the observation from the wrought alloy aged at 600 °C. After ageing at 500 °C, the volume fraction increased as the ageing time increased. However, the volume fraction remained lower than the 600 °C aged samples. After ageing at 700 °C, the volume fraction was the lowest. It can be seen that the width of α-phase and the interparticle spacing between the α-phase increased as a function of ageing temperature and ageing time during single ageing of as-built samples. The slow-heated and the duplex aged samples showed the minimum values of α-phase characteristics when compared to the different ageing approaches.

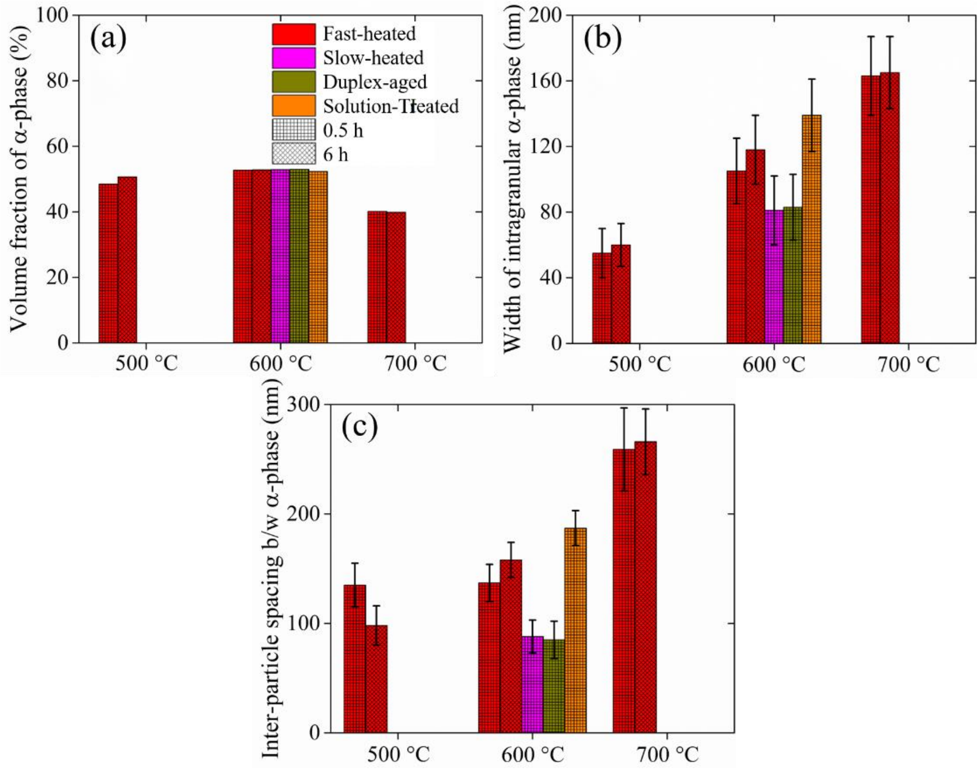

Fig. 6.10. The characteristic variation in (a) volume fraction, (b) width of intragranular α-phase, and (c) interparticle spacing between the α-phase as a function of different ageing approaches.

The variation of grain boundary α-phase thickness and its linear density, *i.e.* total coverage of grain boundary (in %) for single-aged as-built sample as a function of ageing temperature is shown in Fig. 6.11. The characteristics of grain boundary α-phase after ageing the solution-treated sample are also shown in Fig. 6.11. The grain boundary α-phase was analysed over a range of grain boundaries across the sample. For as-built plus aged samples, the grain boundary α-phase thickness and its linear density increased with ageing temperature. The as-built samples aged at 500 °C and 600 °C showed thinner and discontinuous grain boundary α-phase. However, thicker, and continuous grain boundary α-phase was observed after ageing at 700 °C although the boundary coverage is still comparable to that observed in the solution-treated sample after ageing at 600°C. It is important to note here that the solution-treated sample showed the presence of thicker grain boundary α. The grain boundary coverage was also very high when compared with the as-built sample aged at the same temperature (600 °C). The slow-heated and duplex aged sample showed the presence of continuous, but narrow grain boundary α-phase, as can be seen in Fig. 6.9 (c) and (d), respectively.

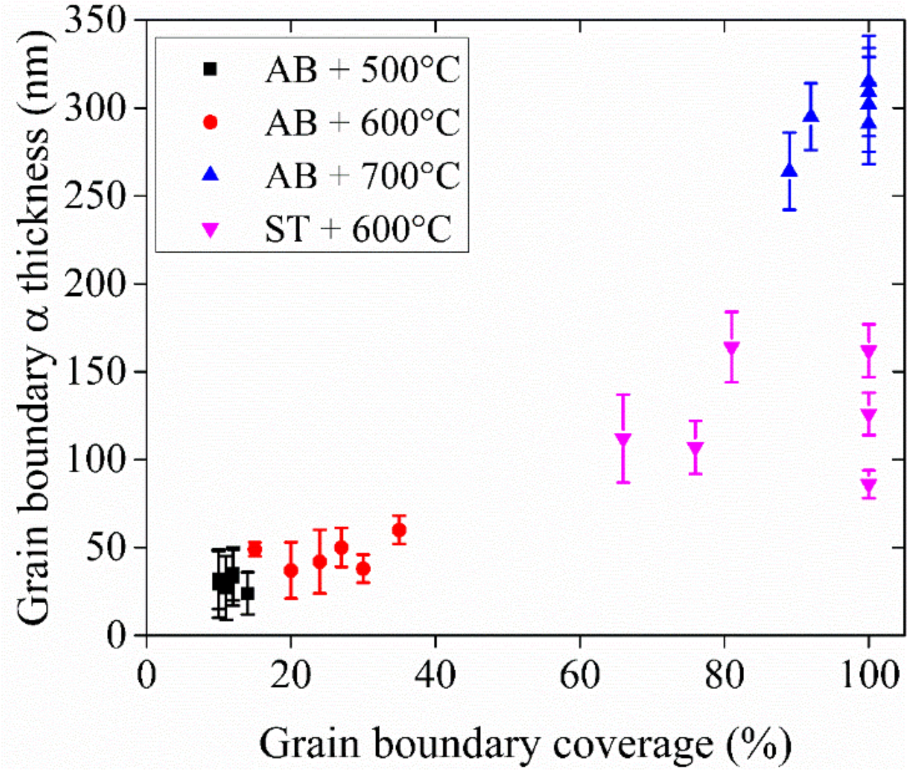

Fig. 6.11. The characteristics of grain boundary α-phase precipitate for as-built (AB) samples as a function of ageing temperature, and for solution-treated (ST) sample after ageing.

6.3.3 Microhardness

The hardness values of as-built and solution-treated samples remained within the error bars and were found to be 311 ± 8 Hv and 305 ± 5 Hv respectively. The removal of sub-structures after solution treatment does not affect the hardness values significantly. Hence, it could be stated that the sub-structures do not act as barriers to the dislocations or do not act as the nucleation points that can possibly affect the subsequent precipitation of α-phase during ageing. However, the hardness value remained low for the aged (600 °C/0.5 h) solution-treated sample (400 ± 5 Hv), when compared to the aged as-built sample (424 ± 4 Hv). The observance of low hardness for the solution-treated sample compared to the as-built sample after ageing can be attributed to the increment in the interparticle spacing [168].

The samples after single ageing with fast heating rate and duplex ageing showed higher hardness when compared with the single-aged samples after fast heating and solution treatment. The trend in the hardness characteristics as a function of different ageing approaches can be seen in Fig. 6.12. The hardness of the single-aged samples with fast heating rate decreased as a function of ageing temperature and ageing time (at 600 °C and 700 °C). However, after ageing at 500 °C, the hardness increased with ageing time. The improvement in the microhardness values of the slow-heated and the duplex-aged samples is because of the reduction in the interparticle spacing due to refined microstructure. However, after single ageing with fast heating rate, the interparticle spacing increased as a function of ageing temperature and ageing time. Hence, the hardness values decreased. The microhardness value of single-aged Ti-5553 alloy after deposition using selective laser melting, as obtained by Carlton *et al.* [132], are approximately similar to the current work values.

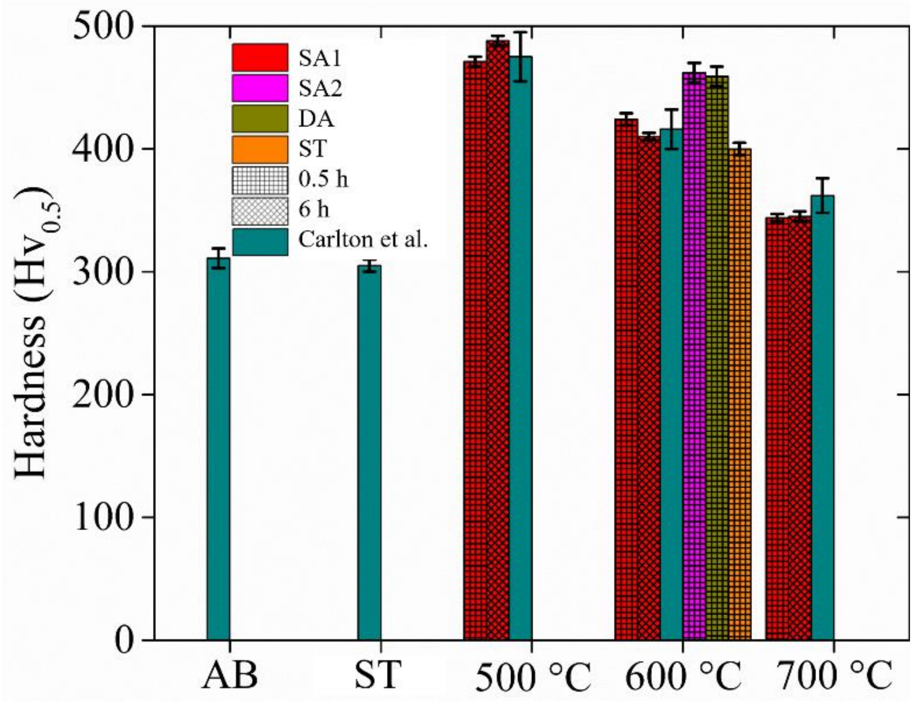

Fig. 6.12. The hardness characteristics AM Ti-5553 β-Ti alloy as a function of different ageing approaches. The hardness values of as-built (AB) and solution-treated (ST) samples are also shown in the Fig. SA1 refers to the single ageing with fast heating rate, SA2 refers to the single ageing with slow heating rate, and DA refers to the duplex ageing.

6.3.4 XRD Analysis

The XRD data for single-aged as-built samples, as a function of single ageing with fast heating rate, can be seen in Fig. 6.13. The as-built sample showed only peaks corresponding to the β-phase, which is in agreement with the SEM micrograph (Fig. *6.3* (b)). After ageing the sample at 300 °C for 8 h, a small volume fraction of isothermal ω-phase can also be seen in the XRD patterns. No presence of α-phase was observed in this condition. After high-temperature ageing, α-phase precipitates were observed along with the β-phase matrix. This could also be seen from the SEM images (Fig. 6.7, Fig. 6.8 and Fig. 6.9).

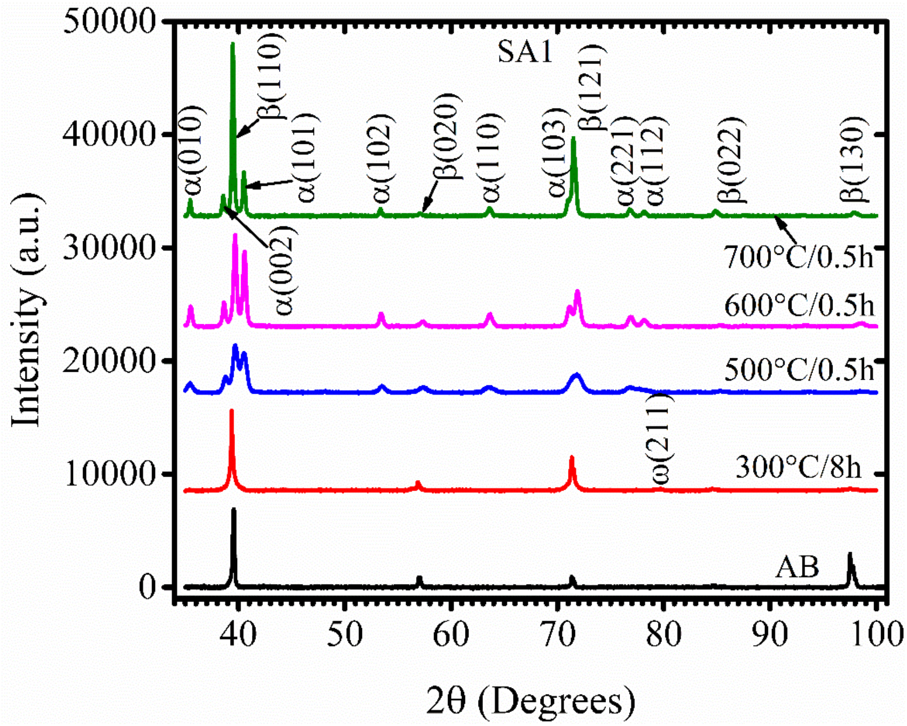

Fig. 6.13. The evolution of XRD diffraction pattern for as-built, pre-aged (300 °C + 8 h) and single-aged after single ageing with fast heating rate. AB refers to the as-built sample.

6.3.5 Electrical Resistivity Measurement

To investigate the influence of sub-structures in the as-built condition on the isothermal ω-phase, the electrical resistivity measurements were done on the as-built plus aged and the solution-treated plus aged samples. *In situ* resistivity measurements were recorded during the low-temperature ageing starting from the room temperature, heating period and during both 300 °C and 325 °C for up to 15 h. The relative electrical resistivity results are shown in Fig. 6.14. The resistivity data is normalized with respect to the resistivity at room temperature.

The electrical resistivity dropped for both samples (as-built and solution-treated) as the temperature was raised to the ageing temperatures (300 °C and 325 °C), as shown in Fig. 6.14 (a) and (b). This decrease in the electrical resistivity can be associated with the partial dissolution of athermal ω-phase [80,141,150–153]. This decrease in electrical resistivity due to the dissolution of athermal ω-phase also confirms the fact that athermal ω-phase is present in the as-built samples.

The first increase in the electrical resistivity can be associated with the time to nucleate isothermal ω-phase precipitates [101]. This occurs for the solution-treated sample (Fig. 6.14) (a)) after ~0.5 h of ageing. Whilst, for the as-built sample the initial increase in electrical resistivity was delayed relative to the solution-treated sample to ~2 h.

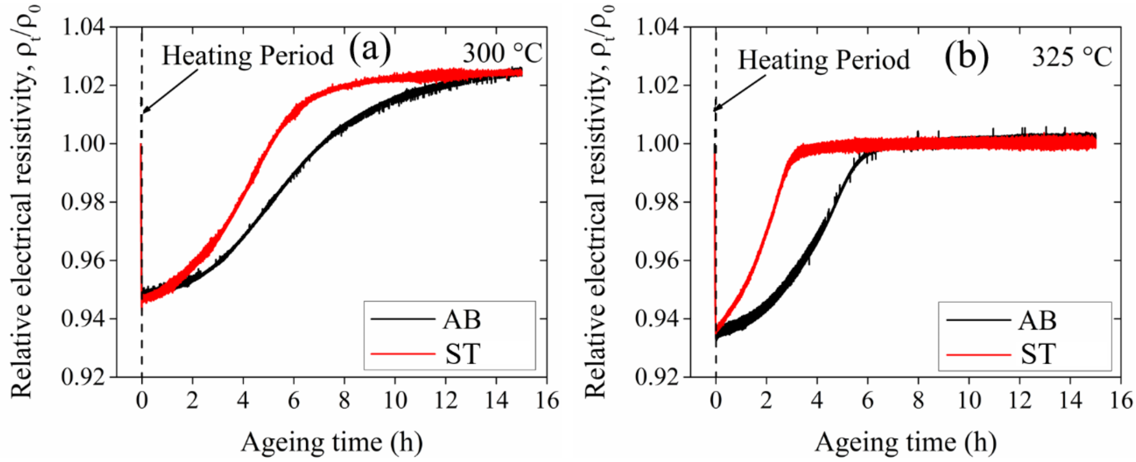

Fig. 6.14. The electrical resistivity measurements for as-built (AB) and solution-treated (ST) samples during ageing at (a) 300 °C and (b) 325 °C for 15 h.

After this initial increase in electrical resistivity during ageing at 300 °C, the electrical resistivity increased further (Fig. 6.14 (a)) and attained an approximate saturation condition after ~9 h and ~14 h of ageing the solution-treated and as-built samples, respectively. For the samples aged at 325 °C, a reduction in the precipitate nucleation time was observed. The first increase in electrical resistivity for the solution-treated sample was observed almost immediately upon reaching the ageing temperature; however, the nucleation time was considerably delayed (~1 h) for the as-built sample.

As for the samples measured at 300 °C the electrical resistivity increased further (Fig. 6.14 (b)) and attained an approximate saturation condition after ~3 h and ~6 h of ageing the solution-treated and as-built samples, respectively.

6.4 Discussion

6.4.1 Formation of Microstructure for As-built Samples

The formation of solely β-phase in the microstructure of the as-built sample can be attributed to the rapid cooling rates (~88 °C/ min) during the deposition of the samples. The high-temperature gradient in the melt pool produced elongated β grains along the build height (Fig. 6.4 (a)). The most easy-growth directions for BCC crystals are <100> and hence the long axis of the dendritic grains are oriented along this orientation [169] producing <100> texture as shown in Fig. *6.4* (c). However, due to repeated heating of subsequent layers, a transition from columnar (dendritic) grains to equiaxed grains can be seen in the microstructure.

The formation of the sub-structures can be understood from the constitutional undercooling [170,171]. The reduction in the temperature gradient ahead of the planar interface increases the undercooling leading to the increased outgrowth away from the interface. Hence, the cell structure is formed, that causes the rejection of solute causing the reduction in equilibrium solidification temperature [170]. The segregation of the solute elements is dependent on their solubility limits in the liquid and the solid state. Depending on the solubility limits of the elements, the solid may either take excess solute from the liquid or reject solute into the liquid. The redistribution of the solute elements can be understood with the help of equilibrium segregation coefficient (k)

(Equation 6.1) that is defined as the ratio of solute concentration in the solid (C_s) and the liquid (C_L) at the solid interface at any given temperature T.

$$k = C_s / C_L \qquad 6.1$$

The solubility of a solute is dependent on the temperature, so for a particular temperature, when $k < 1$, the solute solubility is more in liquid than in the solid. For $k > 1$, the solute solubility is more in solid than in the liquid. This basically means that when the solute solubility decreases for a particular phase then it cannot hold the solute further and rejects it to another phase during solidification. From Ti-Mo and Ti-Cr binary phase diagrams, the k values were found to be greater and less than 1, respectively. This implies that the Mo will be rejected to the solid phase, *i.e.* the core of the sub-structures, however, Cr will be rejected to the sub-structure boundaries. For the remaining solute elements, the k values were found to be approximately equal to 1 that indicates that they will be uniformly distributed across the sub-structures. This is in line with the observations from EDS results (Fig. 6.5). The cellular-dendritic morphology was observed near to the bottom of the scan track and build due to higher temperature gradient. But the sub-structure-free region has the highest temperature gradient during solidification that reduced the outgrowth leading to no sub-structures in this region.

6.4.2 Evolution of Intragranular α-phase Precipitates

Fig. 6.15 (a) and (b) show the inverse pole figure maps for as-built and solution-treated samples, respectively. These maps are superimposed with the grain boundary orientation map, where high-angle boundaries (HAGB > 15°) are represented with black colour lines and the low-angle boundaries (LAGB 2°–15°) are represented with white colour lines. The as-built sample shows a large number density of LAGB within the β grains (Fig. 6.15 (a) when compared to solution-treated sample (Fig. 6.15 (b). The presence of a large number density of LAGBs in the as-built sample indicate that the sample has a large amount of dislocations when compared to solution-treated sample. The presence of higher dislocation density can also be confirmed from the fact that as-built samples have previously [172] shown residual stresses in the deposited condition. This could also be related to the rapid solidification of the sample during deposition. However, the heat treatment of the sample will cause the annihilation of the dislocations [173]. Hence, it could be attributed to the fact that a lower number density of LAGBs were observed in the solution-treated sample.

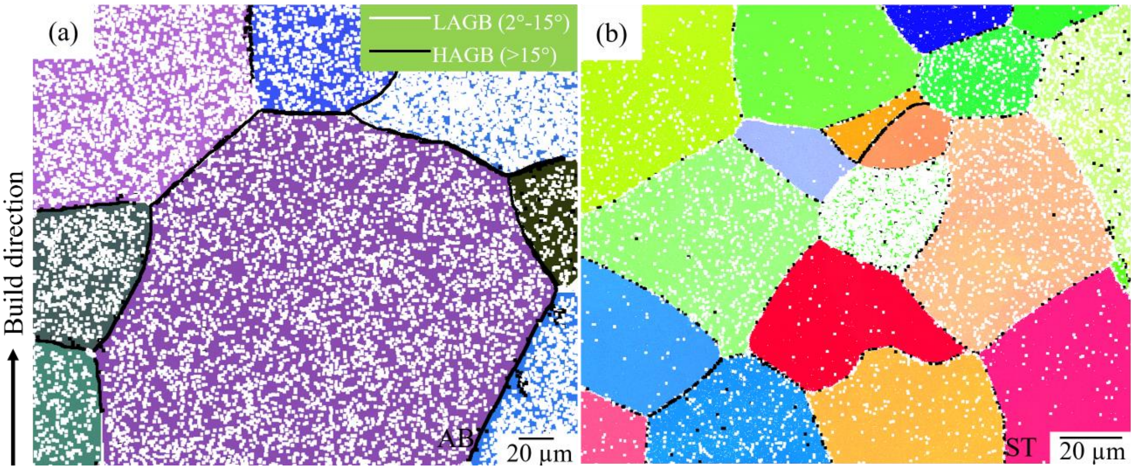

Fig. 6.15. The grain boundary misorientation mapping for (a) as-built and (b) solution-treated (ST) AM Ti-5553 β-Ti alloy.

These dislocations in the sample will act as the nucleation point for the α-phase precipitation. Hence, the refinement of intragranular α-phase for the as-built sample in comparison to solution-treated sample can be attributed to the higher number density of dislocations in the as-built condition. Due to the refinement of intragranular α-phase, there is less enrichment of β-stabilisers in the surrounding area that leads to lower interparticle spacings. Based on EDS analysis (Fig. 6.5), the value of Mo equivalent for the sub-structure free region, the core of the sub-structure and sub-structure boundary are calculated as ~8.3. The Mo equivalent is almost the same for all the regions. Mo equivalent controls the precipitation temperature for the phases. Hence, this can be the reason for getting the uniform microstructure throughout although we have seen Mo and Cr segregation across the sub-structures, but both are β-phase stabilisers.

For single-aged material, the width of α-phase and the interparticle spacing between the α-phase precipitates increased as a function of ageing temperature and ageing time due to availability of larger driving force. The slow-heated and duplex aged samples showed refined α-phase due to isothermal ω-phase assisted nucleation.

6.4.3 Effect of Intragranular α-phase on Microhardness

The effect of interparticle spacing upon the eventual mechanical properties in Ti–6Mo–5V–3Al–2Fe β-Ti alloy has been considered previously [146]. This suggests that the reduction in interparticle spacing observed here would lead to an increase in hardness of around 6% between the as-built and solution-treated samples after ageing. This reduction in the interparticle spacing can also be correlated with the refinement of the α-phase as stated above. The refined microstructure makes the dislocations pile up into more interfaces and this movement is restricted, whilst a coarser microstructure allows greater movement of dislocations leading to more assimilation of plastic deformation. In addition, refinement of α-phase width can directly be linked to the increase in yield strength and hardness [10,136]. Therefore, it could be concluded that the increase in hardness of ~24 Hv after ageing is solely due to the refinement of the α-phase caused due to higher dislocation density in the as-built condition. A similar proportional increase would be expected in the yield and fatigue strength of the material [147,148].

The observance of the highest microhardness values for the slowly heated and the duplex aged samples is because of the extremely refined α-phase precipitates leading to the reduction in the interparticle spacing. However, for the sample aged using single ageing with fast heating rate, the interparticle spacing increased as a function of ageing temperature. Hence, the hardness values decreased with temperature. The samples aged at 500 °C showed the highest hardness amongst the single aged sample using single ageing with fast heating rate. This is attributed to the refined microstructure. The further increment in hardness with ageing time at this temperature was because of the increased number density of α-phase (as stated above) leading to reduced interparticle spacing (Fig. 6.10 (c)). At 700 °C, the hardness was the lowest due to coarser α-phase and highest interparticle spacing. The ageing time at 700 °C did not cause any change in the hardness because the volume fraction, width and interparticle spacing of α-phase remained constant with ageing time. The drop in the hardness with ageing time at 600 °C is because of the coarsening of the α-phase leading to increased interparticle spacing.

6.4.4 Evolution of Grain Boundary α-phase

As understood from Fig. 6.11, the nucleation and growth mechanism of the grain boundary α-phase can be represented as shown in Fig. 6.15. Grain boundary α primarily starts forming with the heterogenous nucleation at the grain boundaries and then grows due to diffusion of Al and O (α stabilizing elements) from the surroundings to the grain boundary α [9]. The diffusion of Al and O from the grain boundary surroundings makes the region rich in β-stabilisers, hence, leading to the formation of PFZ. The growth of the α-phase at grain boundary allows the different nucleants at grain boundary to connect with each other and form a thicker and continuous grain boundary α. The nucleation and growth of the α-phase is a temperature dependent process, however, since as-built and solution-treated samples were aged at the same temperature (600 °C). Hence, it is important to understand the reason for obtaining the difference in the formation of grain boundary α-phase for both the samples.

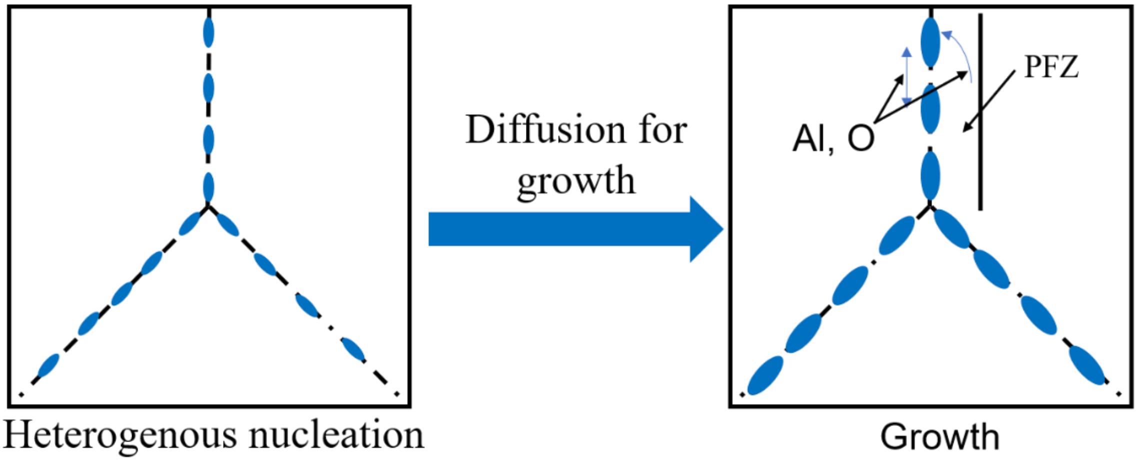

Fig. 6.16. The nucleation and growth mechanism for grain boundary α-phase. Heterogenous nucleation happens at grain boundaries and diffusion of Al and O leads the growth of the grain boundary α-phase and precipitate free zones near grain boundaries.

The refinement of microstructure for the as-built plus aged sample in comparison to the solution-treated plus aged sample may also be linked to a loss of ductility [174]. However, based on previous assessments [9], the ductility is majorly controlled by the grain boundary α-phase. The authors [9] reported an empirical relation between ductility and grain boundary α-phase based on their experimental validation. They reported that the discontinuity in the grain boundary α-phase is directly proportional to ductility and larger discontinuity provides higher ductility. For the current work, discontinuous grain boundary α-phase was observed after ageing the as-built samples at 500 °C and 600 °C. The discontinuous grain boundary and refined intragranular α-phase for as-built samples are highly significant for getting higher ductility and higher strength at the same time.

The observance of discontinuous grain boundary α-phase in as-built samples can be attributed to the presence of high angle β grain boundaries in the as-built condition (Fig. 6.15), whilst the solution-treated sample shows low angle β grain boundaries. The differences and the similarities in the precipitation behaviour of wrought and additively manufactured samples in terms of its microstructural features are presented in Table 6.1.

Table 6.1. The differences and the similarities in the precipitation behaviour of wrought and additively manufactured Ti-5553 β-Ti alloy.

Microstructural feature	Difference/similarities
1. Intragranular α-phase size distribution	• The slow heating and duplex ageing led to a uniform distribution of extremely refined α-phase in both kinds of samples, *i.e.* the wrought and the AM samples. • The fast-heated samples showed a nonuniform α-phase distribution, where larger size α-phase was distributed near to the grain boundaries, whilst relatively finer size α-phase found within the β grains. However, the fast-heated AM samples did not show the presence of Widmanstätten α-phase near to the grain boundaries as observed in wrought alloy after single ageing with a faster heating rate. • When the comparison of the Intragranular α-phase size was done for the wrought and the AM samples, it was observed that the intragranular α-phase precipitates are relatively refined in the AM samples. This could be attributed to the fact that the intragranular α-phase precipitates become more refined when the β grain size reduces [175]. The β grain size for the wrought and the AM samples was found as 245 ± 75 µm and 184 ± 66 µm, respectively.
2. Grain boundary α-phase distribution	• Wrought alloy samples showed the presence of thick and continuous grain boundary α-phase, whilst the AM samples showed the presence of thin and discontinuous grain boundary α-phase. • It was also observed that the reduction in the β grain size will lead to thicker and continuous grain boundary α-phase, however, this was not the case for AM samples (relatively smaller β grains).
3. Morphology of intragranular α-phase	• Both the types of samples, *i.e.*, the wrought and AM samples showed similar morphologies of the intragranular α-phase.

6.4.5 Precipitation Kinetics

Fig. 6.17 shows the evolution of the transformed fraction (F) of isothermal ω-phase precipitates obtained from the electrical resistivity measurements during ageing at 300 °C and 325 °C. Transformed fraction is the ratio between the volume fraction of isothermal ω-phase precipitates at time t during ageing and the volume fraction formed at the metastable equilibrium state [161,162] and is given by Equation 6.2.

$$F = \frac{\rho_t - \rho_0}{\rho_{\mathrm{meta}} - \rho_0} \quad (6.2)$$

where ρ_t refers to the electrical resistivity of the alloy at time t during ageing, ρ_0 refers to the electrical resistivity of the alloy at the beginning of ageing, and ρ_{meta} refers to the electrical resistivity of the alloy at the end of the ageing time.

Similar trends were observed in the electrical resistivity measurments (Fig. 6.14) of the solution-treated and the as-built samples, but a delay in the nucleation of the isothermal ω-phase precipitates (Fig. 6.17) was observed for the as-built samples. Also, a transient nucleation kinetics was observed in both cases *i.e.* an incubation time (τ) is required to reach the critical nucleation size.

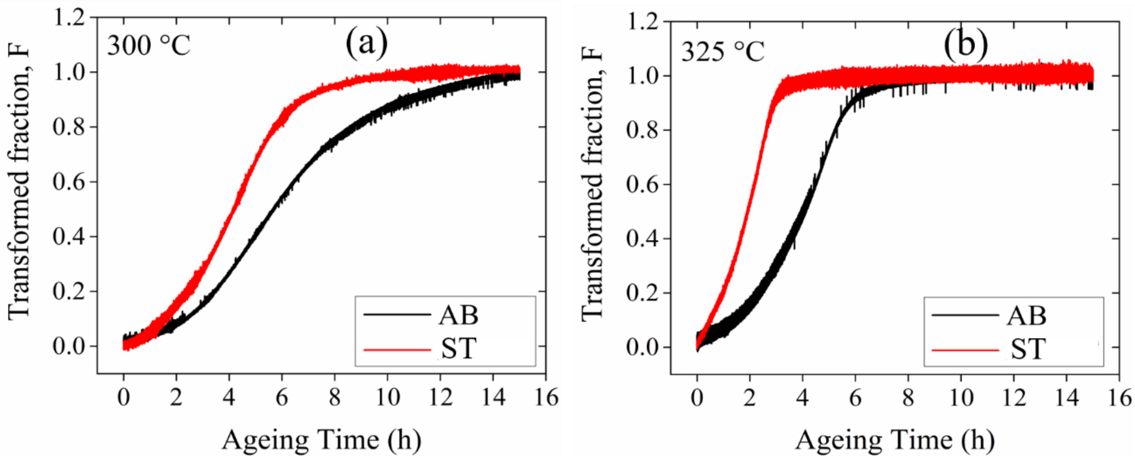

Fig. 6.17. Kinetic curves showing the ω_{iso} transformed fraction vs. ageing time: at (a) 300 °C and (b) 325 °C. A delay in the nucleation of ω_{iso} precipitates was observed for as-built samples when compared to the solution-treated samples. AB refers to the as-built sample and ST refers to the solution-treated sample.

6.4.6 Precipitation Mechanism

Isothermal transformation kinetics of a material can be understood by the universal Johnson-Mehl-Avrami-Kolmogorov (JMAK) model under specific assumptions [163]. The current work shows a transient nucleation behaviour, as observed from the transformed fraction (Fig. 6.17). This violates the universal JMAK model [163,164]. Therefore, a modified version of the JMAK model was utilised to understand the isothermal transformation kinetics of isothermal ω-phase precipitates. The modified JMAK model is given by Equation 6.3.

$$F(t) = 1 - \exp\left(-K_T(t-\tau)^m\right) \tag{6.3}$$

$$K_T = k_0 e^{-Ea/RT} \tag{6.4}$$

where, m represents the Avrami exponent that is an indicative of the precipitation mechanism, K_T is the thermally activated rate constant dependent on the nucleation and growth rate. This can be determined from the Arrhenius relation (Equation (6.4)), where

E_a is the activation energy, R is the universal gas constant and T is the absolute temperature of isothermal ageing. τ refers to the incubation time required to achieve a steady-state precipitate size.

The Avrami exponent, m, was determined for isothermal ω-phase precipitation at 300 °C and 325 °C using Equation (6.5) and the gradients are shown in Fig. 6.18.

$$ln[-ln(1-F)] = lnK_T + mln(t-\tau) \tag{6.5}$$

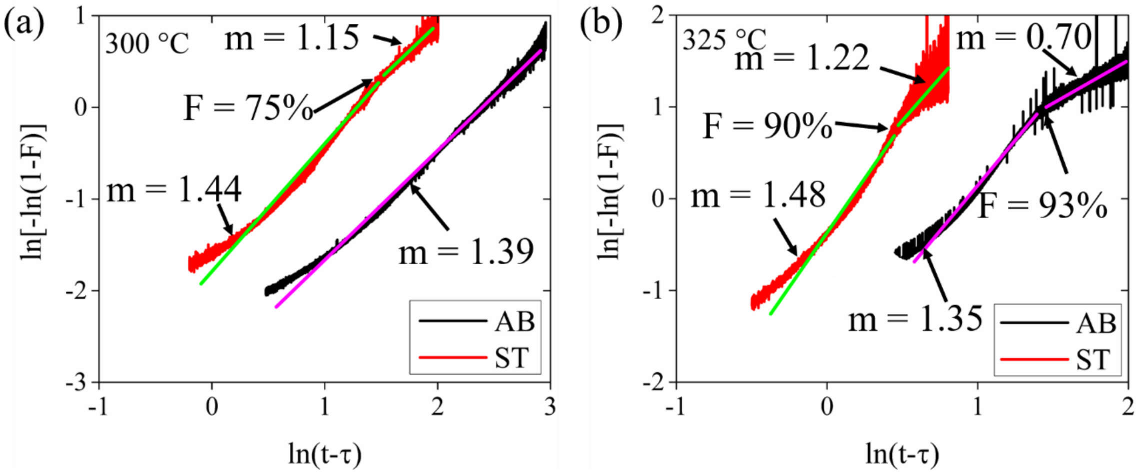

Fig. 6.18. The modified JMAK plots for Avrami exponents (m) during isothermal ω-phase transformation for as-built and solution-treated samples at (a) 300 and (b) 325 °C. AB refers to the as-built sample and ST refers to the solution-treated sample.

The τ values obtained for solution-treated and as-built samples are ~0.5 h and ~2 h, respectively. An m value of approximately 1.4 (see Fig. 6.18) at the early stage of transformation is indicative of a pure growth mechanism from a pre-existing nucleation site [101,163]. This is in line with the growth of isothermal ω-phase precipitates from athermal ω-phase [16]. This is also similar to the precipitation mechanism for wrought alloy (Fig. 5.13). However, the m values reduce at later stage of transformation (Fig. 6.18 and Table 6.2). This reduction in the m values has been attributed to the dimension loss for isothermal ω-phase precipitates at later stages of precipitation due to high misfit strain at the ω_{iso}/β interface [101]. The as-built sample aged at 300 °C does not show any reduction in the m values. This indicates that isothermal ω-phase precipitated in as-built sample after ageing at 300 °C did not lose its dimensions. For the solution-treated sample during ageing at 300 °C, the deviation in m values was observed after ~75 % of transformation (Fig. 6.18), respectively.

The activation energy (E_a) for the formation of isothermal ω-phase, as calculated using the modified JMAK model, showed a higher value for the as-built samples in comparision to the solution-treated samples (Table 6.2). This coul be attributed to the increased incubation time (τ) for isothermal ω-phase nucleation in the as-built sample as compared to the solution-treated sample (Fig. 6.18). The average value of activation energy for isothermal ω-phase precipitation in the additively manufactured alloy was determined as ~130 kJ mol^{-1}. This is approximately similar to the values obtained for wrought alloy and activation energy of Mo atom diffusion in Ti substrate. Hence, it is stated that the precipitation of isothermal ω-phase in AM samples is also controlled by Mo diffusion, as observed for wrought alloy.

Table 6.2. The Avrami exponent (m) and activation energy (E_a) values for entire nanoscale ω_{iso} precipitate transformation during ageing at 300 °C and 325 °C up to 8 h.

Temperature (°C)		Early stage transformation			Later stage transformation
		n (±0.05)	K_T (×10^{-3})	E_a (±12 kJ mol^{-1})	n (±0.05)
ST	300	1.44	17.85	119	1.15
	325	1.48	50.77		-
AB	300	1.39	3.88	140	1.22
	325	1.35	10.85		0.70

6.4.7 Correlation between Microstructure and Microhardness

A good correlation between the microhardness values and the width of α-phase (d) was observed for all the aged samples. A high value of correlation coefficient, $R^2 = 0.91$

was observed for the fitted regression lines. The mean width of α-phase was considered as the best microstructural feature to control the microhardness values. The dependence of microhardness and the the width of α-phase is represented in Fig. 6.19 and the relation is given in Equation 6.6.

$$H_v = 348 + 168/\sqrt{d} \tag{6.6}$$

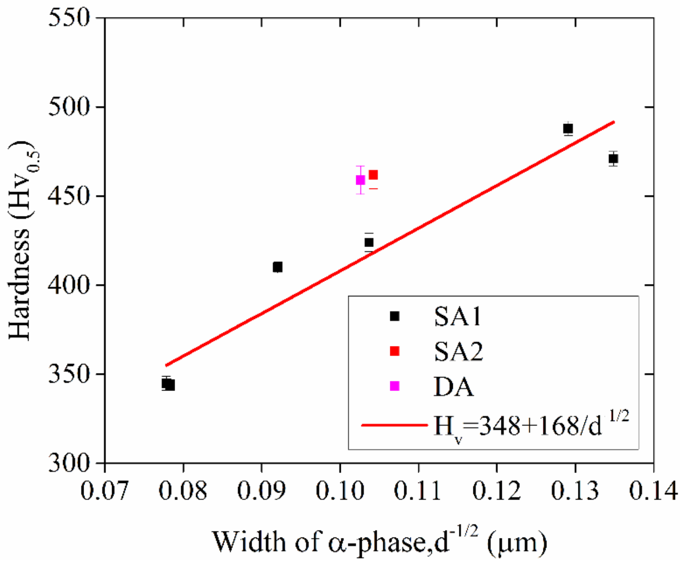

Fig. 6.19. Variation of mean hardness with the inverse of square root of mean width of α-phase after ageing the AM Ti-5553 β-Ti alloy samples. SA1 refers to the single ageing with fast heating rate, SA2 refers to the single ageing with slow heating rate, and DA refers to the duplex ageing.

6.5 Conclusions

The following conclusions can be drawn from this chapter:

1. The direct laser deposition methods can be directly used to deposit the Ti-5553 β-Ti alloy samples with solely β-phase matrix, without having to go for solution treatment. This saves the production time.

2. The aged microstructure of as-built samples showed similar morphology of the α strengthening phase when compared to wrought alloy. This indicates that the as-built samples can be directly used in the application after ageing.
3. The as-built samples exhibited refined intragranular α-phase after single ageing when compared to solution-treated samples, hence producing higher hardness values.
4. The duplex-aged and slow-heated samples showed the maximum hardness due to further refinement of the intragranular α-phase.
5. The single-aged as-built sample with fast heating rate showed discontinuous grain boundary α-phase indicating the possibility of achieving higher ductility for as-built samples in comparison to solution-treated material.
6. The average value of activation energy for isothermal ω-phase precipitation in the additively manufactured alloy was determined as ~130 kJ mol^{-1}. This is approximately similar to the values obtained for the wrought alloy.
7. A good correlation ($H_v = 348 + 168/\sqrt{d}$) between the microhardness values and the width of α-phase (d) was established for all the aged samples.

CHAPTER 7

SUMMARY AND FUTURE WORK

The primary aim of this work was directed at understanding the precipitation behaviour of wrought and additively manufactured Ti-5553 β-Ti alloy. The first investigations were carried out on the wrought Ti-5553 β-Ti alloy to understand the influence of different ageing approaches on its microstructure-property relationship and the precipitation mechanisms. These investigations were coupled with scanning electron microscopy, X-ray diffraction, *in situ* electrical resistivity measurements and Vickers' microhardness studies. The slowly heated and duplex aged samples showed approximately similar microhardness and microstructure results at all ageing conditions. This was attributed to the same precipitation mechanism in both cases as observed via *in situ* electrical resistivity measurements. However, the fast-heated samples showed coarser microstructure and lower hardness in comparison to slowly heated and duplex aged samples. This study also supported that the isothermal ω-phase precipitates have a direct role to play in the nucleation of α-phase precipitates. The slowly heated and duplex aged samples generally showed higher microhardness values in comparison to fast heated samples, however, the difference in the microhardness tended to decrease with ageing time at higher temperatures (600 °C and 700 °C). A good correlation ($H_v = 348 + 247/\sqrt{d}$) between the microhardness values and the width of α-phase (d) was observed for all the aged samples of wrought alloy.

Subsequently, the influence of different cooling rate (air cooling and water quenching) on the precipitation kinetics of isothermal ω-phase was studied by coupling *in situ* small-angle neutron scattering (SANS) and electrical resistivity measurements.

These studies were complemented by scanning electron microscopy, X-ray diffraction and Vickers microhardness studies. The air-cooled sample showed delayed nucleation of isothermal ω-phase precipitates in comparison to water-quenched sample during ageing at 300 °C. This delayed nucleation was attributed to the higher activation energy for isothermal ω-phase precipitation in the air-cooled sample (~131 kJ mol^{-1}) compared to the water-quenched sample (~114 kJ mol^{-1}). The average value of activation energy (~122 kJ mol^{-}) for isothermal ω-phase precipitation in the β-phase matrix was found to be comparable to the activation energy for the diffusion of Mo atoms (~135 kJ mol^{-1}) in the Ti substrate. Because Mo is the slowest diffusing element in the current alloy system, therefore, it was concluded that the isothermal ω-phase precipitation is controlled by the diffusion of Mo. The volume fraction of isothermal ω-phase precipitates became approximately the same (~11 %) after ageing water-quenched and air-cooled samples for 8 h, although air-cooled samples showed slower nucleation. The SANS modelling was consistent with the ellipsoid shaped particles for isothermal ω-phase precipitates, where they achieved a maximum size (equatorial diameter = ~21 nm and ~17 nm) after 2 h and 4 h of ageing the water-quenched and air-cooled samples, respectively. A decrease in the Avrami exponent was observed at later stages of transformation that indicated that isothermal ω-phase precipitates suffer a dimension loss during their growth due to the high misfit strain at the β/ω interface. This was found to be in line with the SANS observations where only equatorial dimension of isothermal ω-phase precipitates grew at later stages of transformation. The Vickers microhardness results showed an increasing trend with ageing time, where water-quenched samples showed higher hardness compared to air-cooled samples.

Lastly, the ageing response of additively manufactured (direct laser deposited) Ti-5553 β-Ti alloy was investigated by coupling with scanning electron microscopy, X-ray diffraction, energy dispersive spectroscopy, electron backscatter diffraction, Vickers' microhardness and *in situ* electrical resistivity measurements studies. It was concluded that the direct laser deposition methods can be directly used to deposit the Ti-5553 β-Ti alloy samples with solely β-phase matrix, without having to go for solution treatment. This will save production time. The similarity in the microstructure features of additively manufactured and wrought alloy samples after ageing boosts the confidence in directly using the as-built samples in the applications after ageing. The as-built samples exhibited refined intragranular α-phase after single ageing when compared to solution-treated samples, hence, producing higher hardness values. Similar to wrought alloy, the duplex-aged and slow-heated additively manufactured samples showed maximum hardness due to further refinement of the intragranular α-phase. Discontinuous grain boundary α-phase was obtained for single-aged as-built sample in comparison to the solution-treated sample. This is an indication of higher ductility for as-built samples in comparison to solution-treated samples after ageing because grain boundary α-phase plays a major role in controlling the ductility of the material. The *in situ* electrical resistivity studies at low temperature ageing (300 °C and 325 °C) indicated that solution treatment of the additively manufactured samples reduces the activation energy for precipitation of isothermal ω-phase. The average value of activation energy for isothermal ω-phase precipitation in the additively manufactured alloy was determined as ~130 kJ mol^{-1} that is approximately similar to the values obtained for wrought alloy. This is an indication of approximately similar precipitation behaviour for both types of alloys. As observed wrought alloy, a good correlation ($H_v =$

$348 + 168/\sqrt{d}$) between the microhardness values and the width of α-phase (d) was observed for all the aged samples.

There is further scope for study in this field. Some of the important future directions are as follows:

- The electrical resistivity results for wrought alloy indicated that different phase transformations happen during the isothermal ω-phase-assisted α-phase nucleation. SANS studies for these pathways can provide better insights as SANS is more sensitive to provide precise structural information at the nano level.
- The SANS signals indicated the dissolution of an unknown metastable phase (bigger size) in wrought alloy as the temperature was raised from room temperature to ageing temperature (300 °C). Further studies on this can provide better insights to this observation.
- The as-built samples showed finer intragranular α-phase precipitates and discontinuous grain boundary α-phase. This is a good indication for producing higher strength (controlled by intragranular α-phase) and higher ductility (controlled by grain boundary α-phase) at the same time. A comparative understanding of mechanical properties for single aged, duplex-aged, solution treated plus aged and slowly heated samples can help in understanding the direct use of additively manufactured samples in the applications.
- The additively manufactured samples showed the presence of sub-structures in the deposited condition. These sub-structures were present just below the melt pool tracks. Although these sub-structures did not show any influence on the

mechanical properties of this material, but the sub-structures in the other materials such as steel have resulted in the better mechanical properties for them. However, the size of the sub-structures in steel was quite small in comparison to the sub-structure size in current material. Hence, the influence of additive manufacturing parameters can be studied to control the sub-structure size that could provide better mechanical properties for titanium alloys.

References

[1] P.J. Bania, Beta titanium alloys and their role in the titanium industry, JOM. 46 (1994) 16–19. doi:10.1007/BF03220742.

[2] R.R. Boyer, An overview on the use of titanium in the aerospace industry, Mater. Sci. Eng. A. 213 (1996) 103–114. doi:10.1016/0921-5093(96)10233-1.

[3] B. He, X. Cheng, J. Li, G.C. Li, H.M. Wang, ω-assisted α phase and hardness of Ti-5Al-5Mo-5V-1Cr-1Fe during low temperature isothermal heat treatment after laser surface remelting, J. Alloys Compd. 708 (2017) 1054–1062. doi:10.1016/j.jallcom.2017.03.089.

[4] H. Yu, M. Yan, J. Li, A. Godbole, C. Lu, K. Tieu, H. Li, C. Kong, Mechanical properties and microstructure of a Ti-6Al-4V alloy subjected to cold rolling, asymmetric rolling and asymmetric cryorolling, Mater. Sci. Eng. A. 710 (2017) 10–16. doi:10.1016/j.msea.2017.10.075.

[5] O.M. Ivasishin, P.E. Markovsky, S.L. Semiatin, C.H. Ward, Aging response of coarse- and fine-grained β titanium alloys, Mater. Sci. Eng. A. 405 (2005) 296–305. doi:10.1016/j.msea.2005.06.027.

[6] Z. Du, S. Xiao, L. Xu, J. Tian, F. Kong, Y. Chen, Effect of heat treatment on microstructure and mechanical properties of a new β high strength titanium alloy, Mater. Des. 55 (2014) 183–190. doi:10.1016/j.matdes.2013.09.070.

[7] J. Fan, J. Li, H. Kou, K. Hua, B. Tang, Y. Zhang, Microstructure and mechanical property correlation and property optimization of a near β titanium alloy Ti-7333, J. Alloys Compd. 682 (2016) 517–524. doi:10.1016/j.jallcom.2016.04.303.

[8] L. Ren, W. Xiao, W. Han, C. Ma, L. Zhou, Influence of duplex ageing on secondary α precipitates and mechanical properties of the near β-Ti alloy Ti-55531, Mater. Charact. 144 (2018) 1–8. doi:10.1016/j.matchar.2018.06.025.

[9] C.M. Liu, H.M. Wang, X.J. Tian, D. Liu, Development of a pre-heat treatment for obtaining discontinuous grain boundary α in laser melting deposited, Mater. Sci. Eng. A. 604 (2014) 176–182. doi:10.1016/j.msea.2014.03.028.

[10] M. Qian, W. Xu, M. Brandt, H.P. Tang, Additive manufacturing and postprocessing of Ti-6Al-4V for superior mechanical properties, MRS Bull. 41 (2016) 775–783. doi:10.1557/mrs.2016.215.

[11] H. Schwab, F. Palm, U. Kühn, J. Eckert, Microstructure and mechanical properties of the near-beta titanium alloy Ti-5553 processed by selective laser melting, Mater. Des. 105 (2016) 75–80. doi:10.1016/j.matdes.2016.04.103.

[12] S. Nag, R. Banerjee, R. Srinivasan, J.Y. Hwang, M. Harper, H.L. Fraser, ω-Assisted nucleation and growth of α precipitates in the Ti-5Al-5Mo-5V-3Cr-0.5Fe β titanium alloy, Acta Mater. 57 (2009) 2136–2147. doi:10.1016/j.actamat.2009.01.007.

[13] G. Lütjering, J.C. Williams, Titanium, Second ed., Springer, New York, 2007.

[14] J.D. Cotton, R.D. Briggs, R.R. Boyer, S. Tamirisakandala, P. Russo, N. Shchetnikov, J.C. Fanning, State of the art in beta titanium alloys for airframe applications, JOM. 67 (2015) 1281–1303. doi:10.1007/s11837-015-1442-4.

[15] M.J. Donachie, Titanium a technical guide, Second ed. Materials Park, OH: ASM International, 2000.

[16] S. Nag, A. Devaraj, R. Srinivasan, R.E.A. Williams, N. Gupta, G.B. Viswanathan, J.S. Tiley, S. Banerjee, S.G. Srinivasan, H.L. Fraser, R. Banerjee, Novel mixed-mode phase transition involving a composition-dependent displacive component, Phys. Rev. Lett. 106 (2011) 7–10. doi:10.1103/PhysRevLett.106.245701.

[17] P. Zháňal, P. Harcuba, M. Hájek, B. Smola, J. Stráský, J. Šmilauerová, J. Veselý, M. Janeček, Evolution of ω phase during heating of metastable β titanium alloy Ti–15Mo, J. Mater. Sci. 53 (2018) 837–845. doi:10.1007/s10853-017-1519-2.

[18] J. Coakley, V.A. Vorontsov, K.C. Littrell, R.K. Heenan, M. Ohnuma, N.G. Jones, D. Dye, Nanoprecipitation in a beta-titanium alloy, J. Alloys Compd. 623 (2015) 146–156. doi:10.1016/j.jallcom.2014.10.038.

[19] H. Liu, M. Niinomi, M. Nakai, K. Cho, Athermal and deformation-induced ω-phase transformations in biomedical beta-type alloy Ti-9Cr-0.2O, Acta Mater. 106 (2016) 162–170. doi:10.1016/j.actamat.2016.01.008.

[20] B.E. Tegner, Phase stability of titanium alloys: a first principles study, PhD Thesis, The University of Edinburgh, UK, 2014.

[21] I. Polmear, D. StJohn, J.F. Nie, M. Qian, Light alloys, Fifth ed., Chennai, India, 2017.

[22] F.W. Chen, G. Xu, X.Y. Zhang, K.C. Zhou, Y. Cui, Effect of α morphology on the diffusional β ↔ α transformation in Ti–55531 during continuous heating: Dissection by dilatometer test, microstructure observation and calculation, J. Alloys Compd. 702 (2017) 352–365. doi:10.1016/j.jallcom.2017.01.209.

[23] S. Sadeghpour, S.M. Abbasi, M. Morakabati, S. Bruschi, Correlation between alpha phase morphology and tensile properties of a new beta titanium alloy, Mater. Des. 121 (2017) 24–35. doi:10.1016/j.matdes.2017.02.043.

[24] T.W. Duerig, G.T. Terlinde, J.C. Williams, The ω-phase reaction in titanium alloy, Titan. ‘80 Sci. Technol. - Proc. 4th Int’l Conf. Titan. (1980) 1299–1308.

[25] A. Devaraj, Phase separation and second phase precipitation in beta titanium alloys, PhD Thesis, University of North Texas, US, 2011.

[26] S. Nag, Y. Zheng, R.E.A. Williams, A. Devaraj, A. Boyne, Y. Wang, P.C. Collins, G.B. Viswanathan, J.S. Tiley, B.C. Muddle, R. Banerjee, H.L. Fraser, Non-classical homogeneous precipitation mediated by compositional fluctuations in titanium alloys, Acta Mater. 60 (2012) 6247–6256. doi:10.1016/j.actamat.2012.07.033.

[27] S. Shekhar, R. Sarkar, S.K. Kar, A. Bhattacharjee, Effect of solution treatment and aging on microstructure and tensile properties of high strength β titanium alloy, Ti–5Al–5V–5Mo–3Cr, Mater. Des. 66 (2015) 596–610.

doi:10.1016/j.matdes.2014.04.015.

[28] Z. Wei, G. Peng, Z. Yongqing, X. Shewei, L. Qian, C. Jun, Z. Siyuan, H. Chaowen, Evolution of primary α phase morphology and mechanical properties of a novel high-strength titanium alloy during heat treatment, Rare Met. Mater. Eng. 46 (2017) 2852–2856. doi:10.1016/S1875-5372(18)30019-5.

[29] A. Dehghan-Manshadi, R.J. Dippenaar, Development of α-phase morphologies during low temperature isothermal heat treatment of a Ti-5Al-5Mo-5V-3Cr alloy, Mater. Sci. Eng. A. 528 (2011) 1833–1839. doi:10.1016/j.msea.2010.09.061.

[30] D. Kent, G. Wang, W. Wang, M.S. Dargusch, Influence of ageing temperature and heating rate on the properties and microstructure of β Ti alloy, Ti-6Cr-5Mo-5V-4Al, Mater. Sci. Eng. A. 531 (2012) 98–106. doi:10.1016/j.msea.2011.10.040.

[31] A. Ghosh, S. Sivaprasad, A. Bhattacharjee, S.K. Kar, Microstructure-fracture toughness correlation in an aircraft structural component alloy Ti-5Al-5V-5Mo-3Cr, Mater. Sci. Eng. A. 568 (2013) 61–67. doi:10.1016/j.msea.2013.01.017.

[32] J. Fan, J. Li, H. Kou, K. Hua, B. Tang, Y. Zhang, Influence of solution treatment on microstructure and mechanical properties of a near β titanium alloy Ti-7333, Mater. Des. 83 (2015) 499–507. doi:10.1016/j.matdes.2015.06.015.

[33] S.K. Kar, S. Suman, S. Shivaprasad, A. Chaudhuri, A. Bhattacharjee, Processing-microstructure-yield strength correlation in a near β Ti alloy, Ti-5Al-5Mo-5V-3Cr, Mater. Sci. Eng. A. 610 (2014) 171–180. doi:10.1016/j.msea.2014.04.113.

[34] J. Lu, Y. Zhao, P. Ge, Y. Zhang, H. Niu, W. Zhang, P. Zhang, Precipitation behavior and tensile properties of new high strength beta titanium alloy Ti-1300, J. Alloys Compd. 637 (2015) 1–4. doi:10.1016/j.jallcom.2015.02.222.

[35] L. Huang, Y. Chen, A study on the microstructures and mechanical properties of forged trace-boron-modified Ti-B20 alloy, Mater. Des. 66 (2015) 110–117. doi:10.1016/j.matdes.2014.10.042.

[36] Y. Zheng, D. Banerjee, H.L. Fraser, A nano-scale instability in the β phase of dilute Ti-Mo alloys, Scr. Mater. 116 (2016) 131–134. doi:10.1016/j.scriptamat.2016.01.044.

[37] Y. Zheng, R.E.A. Williams, H.L. Fraser, Characterization of a previously unidentified ordered orthorhombic metastable phase in Ti-5Al-5Mo-5V-3Cr, Scr. Mater. 113 (2016) 202–205. doi:10.1016/j.scriptamat.2015.10.037.

[38] Z. Du, S. Xiao, L. Xu, J. Tian, F. Kong, Y. Chen, Effect of heat treatment on microstructure and mechanical properties of a new β high strength titanium alloy, Mater. Des. 55 (2014) 183–190. doi:10.1016/j.matdes.2013.09.070.

[39] Y. Zheng, R.E.A. Williams, S. Nag, R. Banerjee, H.L. Fraser, D. Banerjee, The effect of alloy composition on instabilities in the β phase of titanium alloys, Scr. Mater. 116 (2016) 49–52. doi:10.1016/j.scriptamat.2016.01.024.

[40] Y. Zheng, R.E.A. Williams, D. Wang, R. Shi, S. Nag, P. Kami, J.M. Sosa, R. Banerjee, Y. Wang, H.L. Fraser, Role of ω phase in the formation of extremely refined

intragranular α precipitates in metastable β-titanium alloys, Acta Mater. 103 (2016) 850–858. doi:10.1016/j.actamat.2015.11.020.

[41] J.W. Foltz, B. Welk, P.C. Collins, H.L. Fraser, J.C. Williams, Formation of grain boundary α in β Ti alloys : Its role in deformation and fracture behavior of these alloys, Metall. Mater. Trans. A. 42 (2011) 645–650. doi:10.1007/s11661-010-0322-3.

[42] F.J. Gil, M.P. Ginebra, J.M. Manero, J.A. Planell, Formation of α-Widmanstätten structure: Effects of grain size and cooling rate on the Widmanstätten morphologies and on the mechanical properties in Ti6Al4V alloy, J. Alloys Compd. 329 (2001) 142–152. doi:10.1016/S0925-8388(01)01571-7.

[43] S. Sadeghpour, S.M. Abbasi, M. Morakabati, S. Bruschi, Correlation between alpha phase morphology and tensile properties of a new beta titanium alloy, Mater. Des. 121 (2017) 24–35. doi:10.1016/j.matdes.2017.02.043.

[44] V.N. Moiseev, Heat treatment and mechanical properties of titanium alloys with 5–13% aluminium, Met. Sci. Heat Treat 2 (1960) 337–342. doi.org/10.1007/BF00715785.

[45] X. Shi, W. Zeng, Y. Long, Y. Zhu, Microstructure evolution and mechanical properties of near-α Ti-8Al-1Mo-1V alloy at different solution temperatures and cooling rates, J. Alloys Compd. 727 (2017) 555–564. doi:10.1016/j.jallcom.2017.08.165.

[46] D. Qin, Y. Lu, D. Guo, L. Zheng, Q. Liu, L. Zhou, On preparation of bimodal Ti-5Al-5V-5Mo-3Cr-0.4Si (Ti-5553s) alloy: α+β forging and heat treatment, Mater. Sci. Eng. A. 609 (2014) 42–52. doi:10.1016/j.msea.2014.04.056.

[47] M. Ahmed, T. Li, G. Casillas, J.M. Cairney, D. Wexler, E. V. Pereloma, The evolution of microstructure and mechanical properties of Ti-5Al-5Mo-5V-2Cr-1Fe during ageing, J. Alloys Compd. 629 (2015) 260–273. doi:10.1016/j.jallcom.2015.01.005.

[48] N.G. Jones, R.J. Dashwood, M. Jackson, D. Dye, Development of chevron-shaped α precipitates in Ti-5Al-5Mo-5V-3Cr, Scr. Mater. 60 (2009) 571–573. doi:10.1016/j.scriptamat.2008.12.010.

[49] S.C. Wang, M. Aindow, M.J. Starink, Effect of self-accommodation on α/α boundary populations in pure titanium, Acta Mater. 51 (2003) 2485–2503. doi:10.1016/S1359-6454(03)00035-1.

[50] S.V. Kamat, J.P. Hirth, Critical stress for the escape of a group of dislocatins from a partially pinned tilt boundary, Scr. Metall. Mater. 33 (1995) 1795–1800. doi:10.1016/0956-716x(95)98937-z.

[51] D. Srivastava, K. Madangopal, S. Banerjee, S. Ranganathan, Self accomodation morphology of martensite variants in Zr2.5wt%Nb alloy, Acta Metall. Mater. 41 (1993) 3445–3454. doi:10.1016/0956-7151(93)90224-G.

[52] B. Tang, H. Kou, X. Zhang, P. Gao, J. Li, Study on the formation mechanism of α lamellae in a near β titanium alloy, Prog. Nat. Sci. Mater. Int. 26 (2016) 385–390. doi:10.1016/j.pnsc.2016.06.009.

[53] J. Fan, J. Li, Y. Zhang, H. Kou, L. Germain, C. Esling, Formation and crystallography of nano/ultrafine-trimorphic structure in metastable β titanium alloy Ti-5Al-5Mo-5V-3Cr-0.5Fe processed by dynamic deformation at low temperature, Mater. Charact. 130 (2017) 149–155. doi:10.1016/j.matchar.2017.06.005.

[54] A. Settefrati, E. Aeby-Gautier, M. Dehmas, G. Geandier, B. Appolaire, S. Audion, J. Delfosse, Precipitation in a near beta titanium alloy on ageing: Influence of heating rate and chemical composition of the beta-metastable phase, Solid State Phenom. 172–174 (2011) 760–765. doi:10.4028/www.scientific.net/SSP.172-174.760.

[55] S. Bahl, A.S. Krishnamurthy, S. Suwas, K. Chatterjee, Controlled nanoscale precipitation to enhance the mechanical and biological performances of a metastable β Ti-Nb-Sn alloy for orthopedic applications, Mater. Des. 130 (2017) 349. doi:10.1016/j.matdes.2017.05.072.

[56] S. Ankem, C.. Greene, Recent developments in microstructure/property relationships of beta titanium alloys, Mater. Sci. Eng. A. 263 (1999) 127–131. doi:10.1016/S0921-5093(98)01170-8.

[57] J. Coakley, V.A. Vorontsov, N.G. Jones, A. Radecka, P. Aj, K.C. Littrell, Precipitation Processes in the beta-titanium alloy Ti-5Al-5Mo-5V-3Cr, J. Alloys Compd. 646 (2015) 946–953. doi: 10.1016/j.jallcom.2015.05.251.

[58] T.W. Xu, J.S. Li, S.S. Zhang, F.S. Zhang, X.H. Liu, Cold deformation behavior of the Ti-15Mo-3Al-2.7Nb-0.2Si alloy and its effect on α precipitation and tensile properties in aging treatment, J. Alloys Compd. 682 (2016) 404–411. doi:10.1016/j.jallcom.2016.04.293.

[59] N. Clément, A. Lenain, P.J. Jacques, Mechanical property optimization via microstructural control of new metastable beta titanium alloys, JOM. 59 (2007) 50–53. doi:10.1007/s11837-007-0010-y.

[60] C.C. Chung, S.W. Wang, Y.C. Chen, C.P. Ju, J.H. Chern Lin, Effect of cold rolling on structure and tensile properties of cast Ti-7.5Mo alloy, Mater. Sci. Eng. A. 631 (2015) 52–66. doi:10.1016/j.msea.2015.02.045.

[61] G. Choi, K. Lee, Effect of cold rolling on the microstructural evolution of new β-typed Ti–6Mo–6V–5Cr–3Sn–2.5Zr alloys, Mater. Charact. 123 (2017) 67–74. doi:10.1016/j.matchar.2016.11.007.

[62] Z.X. Du, S.L. Xiao, Y.P. Shen, J.S. Liu, J. Liu, L.J. Xu, F.T. Kong, Y.Y. Chen, Effect of hot rolling and heat treatment on microstructure and tensile properties of high strength beta titanium alloy sheets, Mater. Sci. Eng. A. 631 (2015) 67–74. doi:10.1016/j.msea.2015.02.030.

[63] F. Sun, J.Y. Zhang, M. Marteleur, C. Brozek, E.F. Rauch, M. Veron, P. Vermaut, P.J. Jacques, F. Prima, A new titanium alloy with a combination of high strength, high strain hardening and improved ductility, Scr. Mater. 94 (2015) 17–20. doi:10.1016/j.scriptamat.2014.09.005.

[64] A. Lenain, N. Clement, M. Veron, P.J. Jacques, Characterization of the alpha phase nucleation in a two-phase metastable beta titanium alloy, J. Mater. Eng. Perform. 14

(2005) 722–727. doi:10.1361/105994905x75510.

[65] J. Nieh, C. Wu, Y. Chen, C. Wei, S. Lee, Effect of cooling rate during solution heat treatment on the microstructure and mechanical properties of SP-700 titanium alloys, J. Mar. Sci. Technol. 24 (2016) 99–106. doi:10.6119/JMST-015-0409-1.

[66] M. Ikeda, S. Komatsu, M. Ueda, A. Suzuki, The effect of cooling rate from solution treatment temperature on phase constitution and tensile properties of Ti-4.3Fe-7.1Cr-3.0Al Alloy, Mater. Trans. 45 (2004) 1566–1570. doi:10.2320/matertrans.45.1566.

[67] O.N. Senkov, J.J. Valencia, S. V. Senkova, M. Cavusoglu, F.H. Froes, Effect of cooling rate on microstructure of Ti-6Al-4V forging, Mater. Sci. Technol. 18 (2002) 1471–1478. doi:10.1179/026708302225007808.

[68] X.J. Jiang, H.T. Zhao, G. Yu, H.Y. Wu, C.L. Tan, X.Y. Zhang, M.Z. Ma, R.P. Liu, Structural evolution and mechanical properties of Ti-41Zr-7.3Al alloy during continuous cooling process, J. Alloys Compd. 725 (2017) 750–756. doi:10.1016/j.jallcom.2017.07.204.

[69] S.K. Kar, A. Ghosh, N. Fulzele, A. Bhattacharjee, Quantitative microstructural characterization of a near beta Ti alloy, Ti-5553 under different processing conditions, Mater. Charact. 81 (2013) 37–48. doi:10.1016/j.matchar.2013.03.016.

[70] Z. Zhou, Y. Fei, M. Lai, H. Kou, H. Chang, G. Shang, Z. Zhu, J. Li, L. Zhou, Microstructure and mechanical properties of new metastable β type titanium alloy, Trans. Nonferrous Met. Soc. China. 20 (2010) 2253–2258. doi:10.1016/S1003-6326(10)60637-1.

[71] Y. Chen, Z. Du, S. Xiao, L. Xu, J. Tian, Effect of aging heat treatment on microstructure and tensile properties of a new β high strength titanium alloy, J. Alloys Compd. 586 (2014) 588–592. doi:10.1016/j.jallcom.2013.10.096.

[72] J.K. Fan, J.S. Li, H.C. Kou, K. Hua, B. Tang, The interrelationship of fracture toughness and microstructure in a new near β titanium alloy Ti-7Mo-3Nb-3Cr-3Al, Mater. Charact. 96 (2014) 93–99. doi:10.1016/j.matchar.2014.07.018.

[73] X. Zhang, H. Kou, J. Li, F. Zhang, L. Zhou, Evolution of the secondary α phase morphologies during isothermal heat treatment in Ti-7333 alloy, J. Alloys Compd. 577 (2013) 516–522. doi:10.1016/j.jallcom.2013.06.180.

[74] C.L. Li, X.J. Mi, W.J. Ye, S.X. Hui, D.G. Lee, Y.T. Lee, Microstructural evolution and age hardening behavior of a new metastable beta Ti-2Al-9.2Mo-2Fe alloy, Mater. Sci. Eng. A. 645 (2015) 225–231. doi:10.1016/j.msea.2015.08.028.

[75] S. Guo, Q. Meng, G. Liao, L. Hu, X. Zhao, Microstructural evolution and mechanical behavior of metastable β-type Ti – 25Nb – 2Mo – 4Sn alloy with high strength and low modulus, Prog. Nat. Sci. Mater. Int. 23 (2013) 1–9. doi:10.1016/j.pnsc.2013.03.008.

[76] F.H. da Costa, C.A.F. Salvador, M.G. de Mello, R. Caram, Alpha phase precipitation in Ti-30Nb-1Fe alloys – phase transformations in continuous heating and aging heat treatments, Mater. Sci. Eng. A. 677 (2016) 222–229. doi:10.1016/j.msea.2016.09.023.

[77] F.J. Gil, J.M. Manero, M.P. Ginebra, J.A. Planell, The effect of cooling rate on the cyclic deformation of β-annealed Ti-6Al-4V, Mater. Sci. Eng. A. 349 (2003) 150–155. doi:10.1016/S0921-5093(02)00784-0.

[78] P.E. Markovsky, S.L. Semiatin, Tailoring of microstructure and mechanical properties of Ti-6Al-4V with local rapid (induction) heat treatment, Mater. Sci. Eng. A. 528 (2011) 3079–3089. doi:10.1016/j.msea.2010.12.002.

[79] R. Dong, J. Li, J. Fan, H. Kou, B. Tang, Precipitation of α phase and its morphological evolution during continuous heating in a near β titanium alloy Ti-7333, Mater. Charact. 132 (2017) 199–204. doi:10.1016/j.matchar.2017.07.032.

[80] J.C. Williams, B.S. Hickman, H.L. Marcus, The effect of omega phase on the mechanical properties of titanium alloys, Metall. Trans. 2 (1971) 1913–1919. doi:10.1007/BF02913423.

[81] M.J. Lai, C.C. Tasan, J. Zhang, B. Grabowski, L.F. Huang, D. Raabe, Origin of shear induced β to ω transition in Ti-Nb-based alloys, Acta Mater. 92 (2015) 55–63. doi:10.1016/j.actamat.2015.03.040.

[82] Y. Zheng, T. Alam, R.E.A.A. Williams, S. Nag, R. Banerjee, H.L. Fraser, Structural and compositional characteristics of isothermal omega phase in beta titanium alloys, Proc. 13th World Conf. Titan. (2016) 559–562. doi:10.1002/9781119296126.ch90.

[83] F. Langmayr, P. Fratzl, G. Vogl, W. Miekeley, Crossover from ω-phase to α-phase precipitation in bcc Ti-Mo, Phys. Rev. B. 49 (1994) 11759–11766. doi:10.1103/PhysRevB.49.11759.

[84] C. Lin, G. Yin, A. Zhang, Y. Zhao, Q. Li, Simple models to account for the formation and decomposition of athermal ω phase in titanium alloys, Scr. Mater. 117 (2016) 28–31. doi:10.1016/j.scriptamat.2016.01.042.

[85] O.M. Ivasishin, P.E. Markovsky, Y. V. Matviychuk, S.L. Semiatin, Precipitation and recrystallization behavior of beta titanium alloys during continuous heat treatment, Metall. Mater. Trans. A Phys. Metall. Mater. Sci. 34 (2003) 147–158. doi:10.1007/s11661-003-0216-8.

[86] I.B. Ramsteiner, O. Shchyglo, M. Mezger, A. Udyansky, V. Bugaev, S. Schöder, H. Reichert, H. Dosch, Omega-like diffuse X-ray scattering in Ti-V caused by static lattice distortions, Acta Mater. 56 (2008) 1298–1305. doi:10.1016/j.actamat.2007.11.015.

[87] J. Coakley, B.S. Seong, D. Dye, M. Ohnuma, Isothermal omega kinetics in beta-titanium alloys, Philos. Mag. Lett. 97 (2017) 83–91. doi:10.1080/09500839.2017.1282633.

[88] F. Langmayr, P. Fratzl, G. Vogl, W. Miekeley, Crossover from ω-phase to α-phase precipitation in bcc Ti-Mo, Phys. Rev. B. 49 (1994) 11759–11766. doi:10.1103/PhysRevB.49.11759.

[89] S. Dubinskiy, A. Korotitskiy, S. Prokoshkin, V. Brailovski, In situ X-ray diffraction study of athermal and isothermal omega-phase crystal lattice in Ti-Nb-based shape

memory alloys, Mater. Lett. 168 (2016) 155–157. doi:10.1016/j.matlet.2016.01.012.

[90] F. Prima, P. Vermaut, D. Ansel, J. Debuigne, ω precipitation in a beta metastable titanium alloy, resistometric Study, Mater. Trans. JIM. 41 (2000) 1092–1097. doi:10.2320/matertrans1989.41.1092.

[91] N.G. Jones, R.J. Dashwood, M. Jackson, D. Dye, β Phase decomposition in Ti-5Al-5Mo-5V-3Cr, Acta Mater. 57 (2009) 3830–3839. doi:10.1016/j.actamat.2009.04.031.

[92] J.K. Fan, H.C. Kou, M.J. Lai, B. Tang, H. Chang, J.S. Li, Characterization of hot deformation behavior of a new near beta titanium alloy: Ti-7333, Mater. Des. 49 (2013) 945–952. doi:10.1016/j.matdes.2013.02.044.

[93] P. Fratzl, F. Langmayr, G. Vogl, W. Miekeley, The growth of ω-phase inclusions in Ti-20at .% Mo and the competition between lastic and surface energies, Acta Merall. Mater. 39 (1991) 753–761.

[94] T. Gloriant, G. Texier, F. Sun, I. Thibon, F. Prima, J.L. Soubeyroux, Characterization of nanophase precipitation in a metastable β titanium-based alloy by electrical resistivity, dilatometry and neutron diffraction, Scr. Mater. 58 (2008) 271–274. doi:10.1016/j.scriptamat.2007.10.007.

[95] J. Coakley, V.A. Vorontsov, N.G. Jones, A. Radecka, P.A.J. Bagot, K.C. Littrell, R.K. Heenan, F. Hu, A.P. Magyar, D.C. Bell, D. Dye, Precipitation processes in the Beta-Titanium alloy Ti-5Al-5Mo-5V-3Cr, J. Alloys Compd. 646 (2015) 946–953. doi:10.1016/j.jallcom.2015.05.251.

[96] J. Coakley, V.A. Vorontsov, N.G. Jones, A. Radecka, P.A.J. Bagot, K.C. Littrell, R.K. Heenan, F. Hu, A.P. Magyar, D.C. Bell, D. Dye, Precipitation processes in the Beta-Titanium alloy Ti-5Al-5Mo-5V-3Cr, J. Alloys Compd. 646 (2015) 946–953. doi:10.1016/j.jallcom.2015.05.251.

[97] J. Chen, W. Xiao, M.S. Dargusch, C. Ma, The Dependence of isothermal ω precipitation on the quenching rate in a metastable β-Ti alloy, Sci. Rep. 5 (2015) 1–6. doi:10.1038/srep14632.

[98] F. De Geuser, A. Deschamps, Precipitate characterisation in metallic systems by small-angle X-ray or neutron scattering, Comptes Rendus Phys. 13 (2012) 246–256. doi:10.1016/j.crhy.2011.12.008.

[99] A. Deschamps, F. De Geuser, Quantitative characterization of precipitate microstructures in metallic alloys using small-angle scattering, Metall. Mater, Trans. A. 44A (2013) 77-86. doi:10.1007/s11661-012-1435-7.

[100] J. Coakley, V.A. Vorontsov, K.C. Littrell, R.K. Heenan, M. Ohnuma, N.G. Jones, D. Dye, Nanoprecipitation in a beta-titanium alloy, J. Alloys Compd. 623 (2015) 146–156. doi:10.1016/j.jallcom.2014.10.038.

[101] F. Sun, D. Laillé, T. Gloriant, Thermal analysis of the ω nanophase transformation from the metastable β Ti-12Mo alloy, J. Therm. Anal. Calorim. 101 (2010) 81–88. doi:10.1007/s10973-010-0713-0.

[102] C. Lan, Y. Wu, L. Guo, F. Chen, Effects of cold rolling on microstructure, texture evolution and mechanical properties of Ti-32.5Nb-6.8Zr-2.7Sn-0.3O alloy for biomedical applications, Mater. Sci. Eng. A. 690 (2017) 170–176. doi:10.1016/j.msea.2017.02.045.

[103] T. Figueiredo Azevedo, T. Nunes Lima, J. Garcia de Blas, L. Carlos Pereira, S. Griza, The mechanical behavior of TiNbSn alloys according to alloying contents, cold rolling and aging, J. Mech. Behav. Biomed. Mater. 75 (2017) 33–40. doi:10.1016/j.jmbbm.2017.07.002.

[104] R. Santhosh, M. Geetha, V.K. Saxena, M. Nageswara Rao, Effect of duplex aging on microstructure and mechanical behavior of beta titanium alloy Ti-15V-3Cr-3Al-3Sn under unidirectional and cyclic loading conditions, Int. J. Fatigue. 73 (2015) 88–97. doi:10.1016/j.ijfatigue.2014.12.005.

[105] A. Devaraj, V. V. Joshi, A. Srivastava, S. Manandhar, V. Moxson, V.A. Duz, C. Lavender, A low-cost hierarchical nanostructured beta-titanium alloy with high strength, Nat. Commun. 7 (2016) 11176. doi:10.1038/ncomms11176.

[106] Y. Ohmori, T. Ogo, K. Nakai, S. Kobayashi, Effects of ω-phase precipitation on β → α, α″ transformations in a metastable β titanium alloy, Mater. Sci. Eng. A. 312 (2001) 182–188. doi:10.1016/S0921-5093(00)01891-8.

[107] Y. Zheng, D. Choudhuri, T. Alam, R.E.A. Williams, R. Banerjee, H.L. Fraser, The role of cuboidal ω precipitates on α precipitation in a Ti-20V alloy, Scr. Mater. 123 (2016) 81–85. doi:10.1016/j.scriptamat.2016.06.004.

[108] F. Prima, P. Vermaut, G. Texier, D. Ansel, T. Gloriant, Evidence of α-nanophase heterogeneous nucleation from ω particles in a β-metastable Ti-based alloy by high-resolution electron microscopy, Scr. Mater. 54 (2006) 645–648. doi:10.1016/j.scriptamat.2005.10.024.

[109] T. Li, D. Kent, G. Sha, M.S. Dargusch, J.M. Cairney, The mechanism of ω-assisted α phase formation in near β-Ti alloys, Scr. Mater. 104 (2015) 75–78. doi:10.1016/j.scriptamat.2015.04.007.

[110] Y. Zheng, R.E.A. Williams, J.M. Sosa, Y. Wang, R. Banerjee, H.L. Fraser, The role of the ω phase on the non-classical precipitation of the α phase in metastable β-titanium alloys, Scr. Mater. 111 (2016) 81–84. doi:10.1016/j.scriptamat.2015.08.019.

[111] Y. Zheng, R.E.A. Williams, J.M. Sosa, T. Alam, Y. Wang, R. Banerjee, H.L. Fraser, The indirect influence of the ω phase on the degree of refinement of distributions of the α phase phase in metastable β-Titanium alloys, Acta Mater. 103 (2016) 165–173. doi:10.1016/j.actamat.2015.09.053.

[112] T. Li, D. Kent, G. Sha, J.M. Cairney, M.S. Dargusch, The role of ω in the precipitation of α in near-β Ti alloys, Scr. Mater. 117 (2016) 92–95. doi:10.1016/j.scriptamat.2016.02.026.

[113] T. Li, D. Kent, G. Sha, H. Liu, S.G. Fries, A. V. Ceguerra, M.S. Dargusch, J.M. Cairney, Nucleation driving force for ω-assisted formation of α and associated ω morphology in β-Ti alloys, Scr. Mater. 155 (2018) 149–154.

doi:10.1016/J.SCRIPTAMAT.2018.06.039.

[114] D.W. Hayward, L. Chiappisi, S. Prévost, R. Schweins, M. Gradzielski, A small-angle neutron scattering environment for in-situ observation of chemical processes, Sci. Rep. 8 (2018) 1–11. doi:10.1038/s41598-018-24718-z.

[115] S. Nag, R. Banerjee, J.Y. Hwang, M. Harper, H.L. Fraser, Elemental partitioning between and phases in the Ti-5Al-5Mo-5V-3Cr-0.5Fe (Ti-5553) alloy, Philos. Mag. 89 (2009) 535–552. doi:10.1080/14786430802613158.

[116] R. Santhosh, M. Geetha, V.K. Saxena, M. Nageswararao, Studies on single and duplex aging of metastable beta titanium alloy Ti-15V-3Cr-3Al-3Sn, J. Alloys Compd. 605 (2014) 222–229. doi:10.1016/j.jallcom.2014.03.183.

[117] R. Reda, A. Nofal, A.-H. Hussein, Effect of single and duplex stage heat treatment on the microstructure and mechanical properties of cast Ti–6Al–4V alloy, Metallogr. Microstruct. Anal. 2 (2013) 388–393. doi:10.1007/s13632-013-0103-7.

[118] T. Furuhara, T. Maki, T. Makino, Microstructure control by thermomechanical processing in β-Ti-15-3 alloy, J. Mater. Process. Technol. 117 (2001) 318–323. doi:10.1016/S0924-0136(01)00790-7.

[119] S. Nag, R. Banerjee, H.L. Fraser, Microstructural evolution and strengthening mechanisms in Ti-Nb-Zr-Ta, Ti-Mo-Zr-Fe and Ti-15Mo biocompatible alloys, Mater. Sci. Eng. C. 25 (2005) 357–362. doi:10.1016/j.msec.2004.12.013.

[120] E. Aeby-Gautier, A. Settefrati, F. Bruneseaux, B. Appolaire, B. Denand, M. Dehmas, G. Geandier, P. Boulet, Isothermal α″ formation in β metastable titanium alloys, J. Alloys Compd. 577 (2013) S439–S443. doi:10.1016/j.jallcom.2012.02.046.

[121] A. Settefrati, E. Aeby-Gautier, B. Appolaire, M. Dehmas, G. Geandier, G. Khelifati, Low Temperature Transformations in β-Metastable Ti 5553 Titanium Alloy, Mater. Sci. Forum. 738–739 (2013) 97–102. doi:10.4028/www.scientific.net/MSF.738-739.97.

[122] A. Settefrati, M. Dehmas, G. Geandier, B. Denand, E. Aeby-Gautier, B. Appolaire, G. Khelifati, J. Delfosse, Precipitation sequences in beta metastable phase of Ti-5553 alloy during ageing, Proc. 12th World Conf. Titan. (2011) 468–472.

[123] N. Wain, X.J. Hao, G.A. Ravi, X. Wu, The influence of carbon on precipitation of α in Ti-5Al-5Mo-5V-3Cr, Mater. Sci. Eng. A. 527 (2010) 7673–7683. doi:10.1016/j.msea.2010.08.032.

[124] F.H. Froes, H.B. Bomberger, The beta titanium alloys, JOM 37 (1985) 28–37. doi:10.1007/BF03259693.

[125] R.R. Boyer, R.D. Briggs, The use of β titanium alloys in the aerospace industry, J. Mater. Eng. Perf. 14 (2005) 681–685. doi:10.1361/105994905X75448.

[126] B. Roebuck, D. Cox, R. Reed, The temeperature dependence of γ’ volume fraction in a Ni-based single crystal superalloy from resistivity measurements,Scr. Mater. 44 (2001)

917–921. doi: 10.1016/S1359-6462%2800%2900662-X.

[127] J.E. Barnes, W. Peter, C.A. Blue, Evaluation of low cost titanium alloy products, Mater. Sci. Forum. 618 619 (2009) 165–168. doi:10.4028/www.scientific.net/MSF.618-619.165.

[128] N. Shamsaei, A. Yadollahi, L. Bian, S.M. Thompson, An overview of direct laser deposition for additive manufacturing; Part II: Mechanical behavior, process parameter optimization and control, Addit. Manuf. 8 (2015) 12–35. doi:10.1016/j.addma.2015.07.002.

[129] M. Izadi, A. Farzaneh, M. Mohammed, I. Gibson, B. Rolfe, A review of laser engineered net shaping (LENS) build and process parameters of metallic parts, Rapid Prototyp. J. 6 (2020) 1059–1078. doi:10.1108/RPJ-04-2018-0088.

[130] L. Costa, R. Vilar, Laser powder deposition, Rapid Prototyp. J. 15 (2009) 264–279. doi:10.1108/13552540910979785.

[131] H. Schwab, M. Bönisch, L. Giebeler, T. Gustmann, J. Eckert, U. Kühn, Processing of Ti-5553 with improved mechanical properties via an in-situ heat treatment combining selective laser melting and substrate plate heating, Mater. Des. 130 (2017) 83–89. doi:10.1016/j.matdes.2017.05.010.

[132] H.D. Carlton, K.D. Klein, J.W. Elmer, Evolution of microstructure and mechanical properties of selective laser melted Ti-5Al-5V-5Mo-3Cr after heat treatments, Sci. Tech. Weld. Join. 24 (2019) 465-473. doi:10.1080/13621718.2019.1594589.

[133] X. Wu, R. Sharman, J. Mei, W. Voice, Microstructure and properties of a laser fabricated burn-resistant Ti alloy, Mater. Des. 25 (2004) 103–109. doi:10.1016/j.matdes.2003.10.004.

[134] C. Qiu, G.A. Ravi, M.M. Attallah, Microstructural control during direct laser deposition of a β-titanium alloy, Mater. Des. 81 (2015) 21–30. doi:10.1016/j.matdes.2015.05.031.

[135] C. Liu, Y. Lu, X. Tian, D. Liu, Influence of continuous grain boundary α on ductility of laser melting deposited titanium alloys, Mater. Sci. Eng. A. 661 (2016) 145–151. doi:10.1016/j.msea.2016.03.034.

[136] H. Sharma, D. Parfitt, A.K. Syed, D. Wimpenny, E. Muzangaza, G. Baxter, B. Chen, A critical evaluation of the microstructural gradient along the build direction in electron beam melted Ti-6Al-4V alloy, Mater. Sci. Eng. A. 744 (2019) 182–194. doi:10.1016/j.msea.2018.12.016.

[137] C.A. Schneider, W.S. Rasband, K.W. Eliceiri, Historical commentary NIH Image to ImageJ : 25 years of image analysis, Nat. Methods. 9 (2012) 671–675. doi:10.1038/nmeth.2089.

[138] C. Fabrice, Small angle neutron scattering, EPJ web of conferences 104, 01004 (2015). doi: 10.1051/epjconf/201510401004.

[139] O. Arnold, J.C. Bilheux, J.M. Borreguero, A. Buts, S.I. Campbell, L. Chapon, M.

Doucet, N. Draper, R.F. Leal, M.A. Gigg, V.E. Lynch, A. Markvardsen, D.J. Mikkelson, R.L. Mikkelson, R. Miller, K. Palmen, P. Parker, G. Passos, T.G. Perring, P.F. Peterson, S. Ren, M.A. Reuter, A.T. Savici, J.W. Taylor, R.J. Taylor, R. Tolchenov, W. Zhou, J. Zikovsky, Nuclear Instruments and Methods in Physics Research A Mantid — Data analysis and visualization package for neutron scattering and μ SR experiments, Nucl. Inst. Methods Phys. Res. A. 764 (2014) 156–166. doi:10.1016/j.nima.2014.07.029.

[140] ISIS Neutron and Muon Source UK, ENGIN-X Furnace. https://www.isis.stfc.ac.uk/Pages/ENGINX-Furnace.aspx, 2010 (accessed 01 July 2020).

[141] M.A.. Hill, D.H. Polonis Influence of beta phase decomposition on the temperature coefficient of resistivity of titanium alloys, J. Mat. Sci. 22 (1987) 2181–2184.

[142] B. Roebuck, M.G. Gee, M. Brooks, D.Cox, R.Reed, Miniature multiproperty tests at elevated temperatures, Int. Conf. Component Optimistion from Materials Properties and Simulation Software, IRC Swansea, Wales, April (1999).

[143] P. Manda, V. Singh, U. Chakkingal, A.K. Singh, Development of α precipitates in metastable Ti-5Al-5Mo-5V-3Cr and similar alloys, Mater. Charact. 120 (2016) 220–228. doi:10.1016/j.matchar.2016.09.005.

[144] S.E. Haghighi, H.B. Lu, G.Y. Jian, G.H. Cao, D. Habibi, L.C. Zhang, Effect of α″ martensite on the microstructure and mechanical properties of beta-type Ti-Fe-Ta alloys, Mater. Des. 76 (2015) 47–54. doi:10.1016/j.matdes.2015.03.028.

[145] J. Coakley, V.A. Vorontsov, K.C. Littrell, R.K. Heenan, M. Ohnuma, N.G. Jones, D. Dye, Nanoprecipitation in a beta-titanium alloy, J. Alloys Compd. 623 (2015) 146–156. doi:10.1016/j.jallcom.2014.10.038.

[146] H. Zhang, C. Wang, S. Zhang, G. Zhou, L. Chen, Evolution of secondary α phase during aging treatment in novel near β Ti-6Mo-5V-3Al-2Fe Alloy, Mater. 11 (2018) 2283. doi:10.3390/ma11112283.

[147] A. Casagrande, G.P. Cammarota, L. Micele, Relationship between fatigue limit and Vickers hardness in steels, Mater. Sci. Eng. A. 528 (2011) 3468–3473. doi:10.1016/j.msea.2011.01.040.

[148] I. Brooks, P. Lin, G. Palumbo, G.D. Hibbard, U. Erb, Analysis of hardness – tensile strength relationships for electroformed nanocrystalline materials, Mater. Sci. Eng. A. 491 (2008) 412–419. doi:10.1016/j.msea.2008.02.015.

[149] N.G. Jones, R.J. Dashwood, D. Dye, M. Jackson, Thermomechanical processing of Ti-5Al-5Mo-5V-3Cr, Mater. Sci. Eng. A. 490 (2008) 369–377. doi:10.1016/j.msea.2008.01.055.

[150] P. Zháňal, P. Harcuba, J. Šmilauerová, J. Stráský, M. Janeček, B. Smola, M. Hájek, Phase transformations in Ti-15Mo investigated by in situ electrical resistance, Acta Phys. Pol. A. 128 (2015) 779–782. doi:10.12693/APhysPolA.128.779.

[151] D. De Fontaine, N.E. Paton, J.C. Williams, The omega phase transformation in

titanium alloys as an example of displacement controlled reactions, Acta Metall. 19 (1971) 1153–1162. doi:10.1016/0001-6160(71)90047-2.

[152] J. Nejezchlebová, M. Janovská, H. Seiner, P. Sedlák, M. Landa, J. Šmilauerová, J. Stráský, P. Harcuba, M. Janeček, The effect of athermal and isothermal ω phase particles on elasticity of β-Ti single crystals, Acta Mater. 110 (2016) 185–191. doi:10.1016/j.actamat.2016.03.033.

[153] J. Debuigne, F. Prima, Growth kinetic model for isothermal omega phase particles in low-cost beta titanium Ti–6.8Mo–4.5Fe–1.5Al alloy, Mater. Trans. 46 (2005) 1433–1435. doi:10.2320/matertrans.46.1433.

[154] H. Seiner, P. Sedl, M. Landa, J. Smilauerov, B. Denand, M. Dehmas, B. Appolaire, On the complementarity between resistivity measurement and ultrasonic measurement for in-situ characterization of phase transitions in Ti-alloys, J. Alloys Compd. 762 (2018) 868–872. doi:10.1016/j.jallcom.2018.05.173.

[155] Y.Q. Wang, S. Clark, V. Janik, R.K. Heenan, D. Alba Venero, K. Yan, D.G. McCartney, S. Sridhar, P.D. Lee, Investigating nano-precipitation in a V-containing HSLA steel using small angle neutron scattering, Acta Mater. 145 (2018) 84–96. doi:10.1016/j.actamat.2017.11.032.

[156] J. Chen, W. Xiao, M.S. Dargusch, C. Ma, The dependence of isothermal ω precipitation on the quenching rate in a metastable β-Ti alloy, Sci. Rep. 5 (2015) 14632. doi:10.1038/srep14632.

[157] N.G. Jones, R.J. Dashwood, D. Dye, M. Jackson, Thermomechanical processing of Ti-5Al-5Mo-5V-3Cr, Mater. Sci. Eng. A. 490 (2008) 369–377. doi:10.1016/j.msea.2008.01.055.

[158] B. Hammouda, Probing nanoscale structures – the SANS toolbox. https://www.ncnr.nist.gov/staff/hammouda/the_SANS_toolbox.pdf, 2016 (accessed 11 October 2020.

[159] D. Geuser, On the validity of simple precipitate size measurements by small-angle scattering in metallic systems research papers, J. App. Cryst. (2011) 343–352. doi:10.1107/S0021889811003049.

[160] SasView, SasView user documentation. http://www.sasview.org/docs/user/user.html, 2018 (accessed 01 July 2020)

[161] Q. Hui, X. Xue, H. Kou, M. Lai, B. Tang, J. Li, Kinetics of the ω phase transformation of Ti-7333 titanium alloy during continuous heating, J. Mater. Sci. 48 (2013) 1966–1972. doi:10.1007/s10853-012-6962-5.

[162] F. Lourdjane, A.A. Raho, Precipitation kinetics of the GP zones in Al4,65at .% Ag(15%Wt.), Am. J. Mater. Sci. Eng. 3 (2015) 11–14. doi:10.12691/ajmse-3-1-3.

[163] I. Sinha, R.K. Mandal, Avrami exponent under transient and heterogeneous nucleation transformation conditions, J. Non. Cryst. Solids. 357 (2011) 919–925. doi:10.1016/j.jnoncrysol.2010.11.005.

[164] I. Sinha, R.K. Mandal, Isothermal nanocrystallization kinetics during polymorphic transformation, J. Non. Cryst. Solids. 355 (2009) 361–367. doi:10.1016/j.jnoncrysol.2008.12.006.

[165] K.D. Li, K. Chen, Kinetics modeling of precipitation with characteristic shape during post-implantation annealing, AIP Adv. 5 (2015) 117211. doi:10.1063/1.4935568.

[166] A.D. Abramenkov, Y.M. Fogel, V. V Slyozov, L. V Tanatarov, O.P. Ledenyov, Research on diffusion of Mo substrate atoms into Ti and Cr thin films by secondary ion-ion emission method, Phys. Met. Metallogr. 29 (1970) 4–6.

[167] C.F. Yolton, F.H. Froes, R.F. Malone, Alloying element effects in metastable beta titanium alloys, Met. Trans. A. 10A (1979) 132–134..

[168] G.H. Zhao, X.Z. Liang, B. Kim, P.E.J. Rivera-Díaz-del-Castillo, Modelling strengthening mechanisms in beta-type Ti alloys, Mater. Sci. Eng. A. 756 (2019) 156–160. doi:10.1016/j.msea.2019.04.027.

[169] B. Vrancken, L. Thijs, J. Kruth, J. Van Humbeeck, Microstructure and mechanical properties of a novel b titanium metallic composite by selective laser melting, Acta Mater. 68 (2014) 150–158. doi:10.1016/j.actamat.2014.01.018.

[170] D.A. Porter, K.E. Easterling, Phase Transformations in Metals and Alloys, Second ed., Springer-Science + Business Media, Hong Kong, 1992.

[171] K. Saeidi, X. Gao, Y. Zhong, Z.J. Shen, A Hardened austenite steel with columnar sub-grain structure formed by laser melting, Mater. Sci. Eng. A. 625 (2015) 221–229. doi:10.1016/j.msea.2014.12.018.

[172] R. Acevedo, P. Sedlak, R. Kolman, M. Fredel, Residual stress analysis of additive manufacturing of metallic parts using ultrasonic waves: State of the art review, J. Mater. Res. Technol. (2020) 1–21. doi:10.1016/j.jmrt.2020.05.092.

[173] M. Hu, W.D. Fei, C.K. Yao, Effect of heat treatment on dislocation states and work hardening behaviors of SiCw/6061Al composite, Mater. Lett. 56 (2002) 637–641. doi:10.1016/S0167-577X(02)00568-2.

[174] Z.D. Lü, C.J. Zhang, Z.X. Du, J.C. Han, S.Z. Zhang, F. Yang, Y.Y. Chen, Relationship between microstructure and tensile properties on a near-β titanium alloy after multidirectional forging and heat treatment, Rare Met. 38 (2019) 336–342. doi:10.1007/s12598-018-1159-y.

[175] B. Zhang, Y. Chong, R. Zheng, Y. Bai, R. Gholizadeh, M. Huang, D. Wang, Q. Sun, Y. Wang, N. Tsuji, Enhanced mechanical properties in β-Ti alloy aged from recrystallized ultrafine β grains, Mater. Des. 195 (2020) 109017. doi:10.1016/j.matdes.2020.109017.